

OPEN JOURNAL OF

NAN



ISSN:2147-0081

Volume:7, Issue: 2, Year: 2022

A JOURNAL ABOUT  
NANOSCIENCE

## Open Journal of Nano

### Editor in Chief

Dr. Mustafa CAN, Sakarya University of Applied Sciences, Turkey  
mustafacan@subu.edu.tr

### Editorial Board

Dr. Emrah ÖZAKAR, Ataturk University,  
Erzurum, Turkey.  
emrahozakar@atauni.edu.tr

Dr. Hamza ŞİMŞİR, Karabuk University,  
Turkey.  
hamzasimsir@karabuk.edu.tr

Dr. Harun GÜL, Sakarya University of  
Applied Sciences, Turkey.  
harungul@subu.edu.tr

Dr. Mustafa Zahid YILDIZ, Sakarya  
University of Applied Sciences, Turkey.  
mustafayildiz@sakarya.edu.tr

Dr. Numan GÖZÜBENLİ, Harran  
University, Turkey.  
gnuman@harran.edu.tr

Dr. Oğuz SARIBIYIK, Gümüşhane  
University, Gumushane, Turkey.  
oysaribiyik@gumushane.edu.tr

Dr. Tuğrul ÇETİNKAYA, Sakarya  
University, Turkey.  
tcetinkaya@sakarya.edu.tr

Dr. Yasin AKGÜL, Karabuk University,  
Turkey.  
yasinakgul@karabuk.edu.tr

### Field Editors

Dr. Hasan HACİFAZLIOĞLU, İstanbul  
University-Cerrahpaşa, İstanbul, Turkey.  
hasanh@istanbul.edu.tr

Dr. Mithat ÇELEBİ, Yalova University,  
Turkey.  
mithat.celebi@yalova.edu.tr

Dr. Zafer Ömer ÖZDEMİR, University of  
Health Sciences, Turkey.  
zaferomer.ozdemir@sbu.edu.tr

Dr. Erol ALVER, Hitit University, Turkey.  
erolalver@hitit.edu.tr

Dr. Kamal YUSOH, University Malaysia  
Pahang, Malaysia.  
kamal@ump.edu.my

Dr. Tetiana TEPLA, Lviv Polytechnic  
National University, Ukraine.  
tetiana.l.tepla@lpnu.ua

Dr. Birgül BENLİ, İstanbul Technical  
University, Turkey.  
benli@itu.edu.tr

Dr. Deniz ŞAHİN, Gazi University, Turkey.  
dennokalk@hotmail.com

### Statistics Editor

Dr. Özer UYGUN, Sakarya University,  
Sakarya, Turkey.  
ouygun@sakarya.edu.tr

## Open Journal of Nano

### Editorial Assistants

Mücahid SARI, Sakarya University of Applied Sciences, Sakarya, Turkey.  
<https://dergipark.org.tr/en/pub/@mucahidsari>

Dr. Hamza ŞİMŞİR, Karabuk University, Turkey.  
[hamzasimsir@karabuk.edu.tr](mailto:hamzasimsir@karabuk.edu.tr)

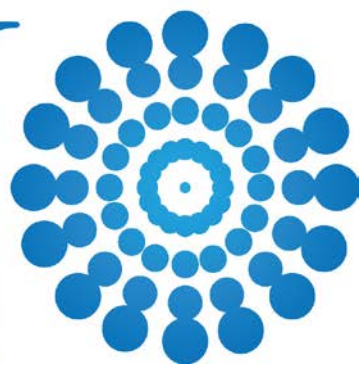
Engin Deniz PARLAR, Sakarya University of Applied Sciences, Sakarya, Turkey. [denizparlar97@hotmail.com](mailto:denizparlar97@hotmail.com)

Nadir ATMACA, The Istanbul Metropolitan Municipality, Istanbul, Turkey.  
[nadiratmaca@gmail.com](mailto:nadiratmaca@gmail.com)

Halid ÖZGÜR, FreshForty Media, Turkey  
[halid@freshforty.media](mailto:halid@freshforty.media)

Enis AKSOY, Areya illüstrasyon, Sakarya, Turkey  
[enisaksoy@gmail.com](mailto:enisaksoy@gmail.com)






---

**Contents**

**Volume: 7, Issue: 2, Year: 2022**

<b>Use of F-type Fly Ash in Cement Mortar with Alternative Mixing Methods</b> (Research Article)	<b>Arife Akin, Marwan Alithawi</b>	41-52
<b>Modification of PVDF Membranes Using Dopamine/Zinc Oxide for Lead Removal from Aqueous Media</b> (Research Article)	<b>İrem Sevim Üçel, Elif Demirel</b>	53-73
<b>Synthesis and Photophysical Properties of Pyrene-BODIPY Functionalized Subphthalocyanine Dyad</b> (Research Article)	<b>Seda Çetindere</b>	74-80
<b>Fractal adsorption characteristics and statistical analysis approach of complex dye molecule on metal oxide particles—A case study of Reactive Black 5 (RB 5) adsorption onto NiO nanoparticles</b> (Research Article)	<b>Ferda Gönen, Gizem Biçer</b>	81-93
<b>Investigation of the Effects of Unidirectional Compression on the Hardness of High-Density Polyethylene Materials</b> (Research Article)	<b>Erkin AKDOĞAN</b>	94-102

# Use of F-type Fly Ash in Cement Mortar with Alternative Mixing Methods

\*<sup>1</sup> Arife Akın , <sup>1</sup> Marwan Alithawi

Konya Technical University, Civil Engineering Depart., Konya/Turkey

\* Corresponding author, e-mail: aakin@ktun.edu.tr

Submission Date: 03.01.2022

Acceptation Date: 14.02.2022

**Abstract** - In this study, it is focused on the use of fly ash, which is one of the industrial wastes, as a partial replacement of cement and fine aggregate in cement mortar. The feasibility of using fly ash as an alternative to cement and fine aggregates in concrete was determined by examining its effect on strength and durability properties in composites. Fly ash was used in the mixtures with three different mixing methods. This is the simple substitution method, addition method and partial substitution method. In each method, 10%, 20% and 30% of the material was removed by weight, and a total of ten different mixtures were prepared by adding fly ash instead. As a result of the experiments to determine the properties of the mixtures in the fresh and hardened state, the addition of fly ash to the mixtures improved the workability and freeze-thaw resistance. When we look at the results in terms of the methods used in the study, it was seen that the addition method gave better results in pressure, water absorption and capillary water absorption experiments than other methods, and according to the bending and cylinder splitting test results, higher values were obtained in the mixtures prepared with the partial substitution method compared to the other mixing methods.

**Keywords:** Fly ash, simple substitution method, partial substitution method, addition method, mechanical properties, freeze-thaw, permeability properties

## Alternatif Karışım Yöntemleri ile F tipi Uçucu Külün Çimento Harcı İçerisinde Kullanımı

**Öz** - Bu çalışmada, endüstriyel atıklardan birisi olan uçucu külün çimento harcı içerisindeki çimento ve ince agreganın kısmi ikamesi olarak kullanılmasına odaklanılmıştır. Betonda çimento ve ince agregalara alternatif olarak uçucu kül kullanımının uygulanabilirliği, kompozitlerde dayanım ve dayanıklılık özelliklerine etkisinin incelenmesi ile belirlenmiştir. Uçucu kül, karışımlar içerisinde üç farklı karışım yöntemi ile kullanılmıştır. Bunlar; basit ikame yöntemi, ilave yöntemi ve kısmi ikame yöntemidir. Her bir yöntemde %10, %20 ve %30 oranında ağırlıkça malzeme çıkarılmış, yerine uçucu kül eklenerek toplam on farklı karışım hazırlanmıştır. Karışımların taze ve sertleşmiş haldeki özelliklerinin belirlenmesine yönelik yapılan deneyler neticesinde, uçucu külün karışımlara eklenmesi işlenebilirliği ve donma-çözülme direncini iyileştirmiştir, su emme ve kılcal su emme oranı değerleri ise uçucu kül içeriğinin artmasıyla ilk günlerde artış göstermiş fakat ilerleyen yaşlarda azalmıştır. Çalışmada kullanılan yöntemler açısından sonuçlara bakıldığında basınç, su emme ve kılcal su emme deneylerinde ilave yönteminin, diğer yöntemlere göre daha iyi sonuçlar verdiği görülmüş, eğilme ve silindir yarma deney sonuçlarına göre ise, kısmi ikame yöntemi ile hazırlanan karışımlarda diğer karıştırma yöntemlerine kıyasla daha yüksek değerler elde edilmiştir.

**Anahtar kelimeler:** Uçucu kül, basit ikame yöntemi, kısmi ikame yöntemi, ilave yöntemi, mekanik özellikler, donma-çözülme, geçirimsizlik özellikleri

### 1. Introduction

Concrete is the most used building material worldwide. The use of cement and aggregate in concrete composition causes rapid depletion of natural resources and environmental pollution. Replacing any of these materials with industrial waste materials has a positive impact on the environment as it reduces the problem of waste disposal, intensive use of energy and natural resources. The durability of concrete is an important consideration to ensure a long service life in aggressive environments. Although Portland cement is one of the main components used in concrete production, it is a relatively high cost material that has no alternative in the construction industry. A

<sup>1</sup> Corresponding author: Tel: 0 533 774 07 12  
E-mail: aakin@ktun.edu.tr

large amount of cement production causes environmental problems and also consumes a lot of energy. It causes about 7% of the total greenhouse gas emissions in the world [1]. In this situation, engineers and scientists are faced with the crucial decision to either destroy the ecosystem by continuing concrete production or to seek an alternative methodology to conserve natural resources by reducing CO<sub>2</sub> emissions [2]. They can be used as alternative sources in concrete as they can help solve some environmental concerns such as the use of industrial waste materials as recycled materials, the problem of waste disposal, and the intensive use of energy and natural resources. There are many industrial waste products that have the potential to replace aggregate and cement in concrete, such as plastic, fly ash, rubber, steel, and leather waste. Fly ash (FA), which is one of these industrial wastes, can be partially used instead of cement thanks to its pozzolanic structure, thus reducing the carbon emissions and industrial waste amount resulting from cement production. Class F FA contains a small amount of lime. Thus, the increase in the amount of FA in the concrete causes a decrease in the compressive strength. However, the pozzolanic activity of FA increases the compressive strength in advancing curing times [3]. As a result of the pozzolanic reaction, the increase in strength lasts longer than conventional concrete [4].

The voids in the concrete affect the transport of environmental fluids. In their study, Supit and Shaikh observed that with the addition of FA to concrete, the void volume decreased by 6-11% compared to conventional concrete [5]. On the other hand, in the study reported by Mardani-Aghabaglou et al.[6], it was reported that the durability performance was adversely affected as the FA ratio increased with the replacement of FA with cement.

FA can be used in concrete with three different mixing methods [7]. These; simple substitution method, addition method and partial substitution method. In the simple substitution method, a certain amount of cement is removed from the mixture and replaced with the same amount of FA. Concretes produced by this method have low strength at early ages. The main purpose of using the simple substitution method is to reduce the heat of hydration and increase the workability in mass concrete production. In addition, this method can be evaluated environmentally and economically. In the addition method, fine aggregate is removed from the mixture without changing the amount of cement in the mixture and FA is added instead. Thus, the amount of binder in the mixture increases. The main purpose of using this method is to increase the strength of concrete in later ages and to obtain a more impermeable concrete with a denser microstructure. In the partial replacement method, FA is substituted for the cement and fine aggregate removed from the mixture. In this method, it is aimed to provide optimum benefit from the positive features provided by the two methods mentioned above. In this study, three different ratios of FA were added to the mixtures with three different mixing methods and their effects on the fresh and hardened mortar properties were investigated. In the literature, FA is widely used in mortar by replacing cement [8]. In this study, the effects of FA on mixture properties were investigated by substituting both cement and aggregate in equal proportions. Various tests were carried out to determine the consistency and unit weight values of fresh mixtures and the strength, permeability and durability properties of hardened samples. Compressive, flexural and cylinder splitting strength tests in the determination of mechanical properties; water absorption and capillary water absorption in determining permeability properties, in the determination of durability properties, freeze-thaw tests were carried out.

## 2. Materials and Methods

### 2.1. Materials

In the study, CEM I 42.5 R type cement, F class FA according to ASTM C618 [9] standard and sand obtained from local sources with 0-4 mm grain size were used. Chemical and physical properties of cement and FA are given in Table 1.

**Table 1.** Chemical and physical properties of cement and fly ash.

Chemical Composition (%)	Cement (C)	Fly Ash(FA)
SiO <sub>2</sub>	20.8	50.98
Al <sub>2</sub> O <sub>3</sub>	5.42	13.11
Fe <sub>2</sub> O <sub>3</sub>	2.98	9.74
S+A+F	29.2	73.83
CaO	61.53	11.82
MgO	2.39	3.91
SO <sub>3</sub>	2.4	3.94
K <sub>2</sub> O	0.75	1.91
Na <sub>2</sub> O	0.21	2.71
<b>Physical Properties</b>		
Specific weight (g/cm <sup>3</sup> )	3.06	2.36
Fineness (cm <sup>2</sup> /g)	3250	2900

## 2.2. Preparation of Mixtures and Experiments

When designing the mixtures, three different methods were used for incorporating FA into the mixture. In this way, a total of 10 different mixture sets were created, FA was not used for the control mixture(FA(0)). 9 different mixtures were obtained by using 3 different ratios of FA in 3 different methods. Mixing codes and material ratios are given in Table 2.

In the preparation of the mixtures, 25 L capacity planetary mixer is used. First of all, dry materials (aggregates, cement and FA) are processed at 100 rpm. was mixed at speed for 1 minute. Then water was added and 150 rpm. speed for 1 minute, finally 300 rpm. The mixing process was completed by mixing at high speed for 3 minutes (Figure 1). Prepared mixtures were placed in pre-lubricated molds and a vibrator was used for compaction. After 24 hours, the samples were taken out of their molds and placed in a pool filled with lime-saturated water.

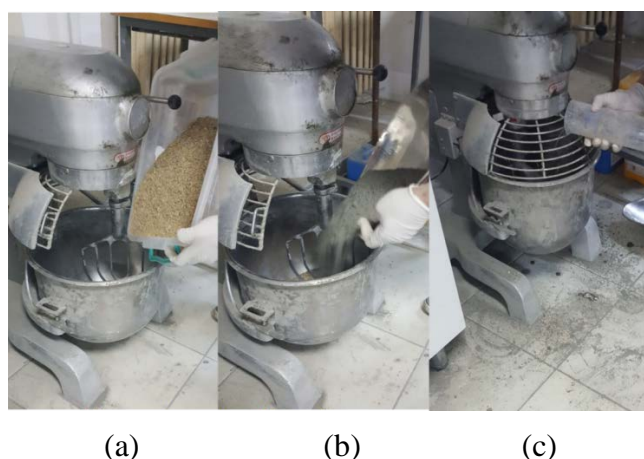


**Figure 1.** Preparation of mixtures a) Sand addition, b) Cement and fly ash addition, c) Water addition.

One of the tests applied to determine the fresh state properties of the mixtures, the unit weight test was carried out according to the ASTM C138 [9] standard. With this method, it was determined how much the weight of FA, which has a lower unit volume weight than cement, can be reduced compared to the control mixture by using different proportions and different methods in the mixtures. In order to determine the fresh state properties of the mixtures, the spreading table test was carried out in accordance with the ASTM C230[10] standard. The mortar taken from the mixing bowl to the tray was placed in the mold on the spreading plate so that it was half filled, and after it was hit 25 times with the mallet, the other part of the mold was filled and another 25 strokes were applied. After the upper surface of the mold was cleaned and smoothed with a trowel, the handle of the test tool, which was taken by pulling the mold, was rotated 5 times in 15 seconds, the diameter of the spread

mixture was measured with the help of a meter in 2 different axes and the average of the readings was recorded (Figure 2).



**Figure 2.** Spreading table test.

Mechanical and permeability tests were carried out on the hardened samples at the end of the 7, 28 and 90 days following production, and the freeze-thaw test was performed at the end of the 28 day. Compressive strength test was carried out on 50x50x50 mm cube samples in accordance with ASTM C39[11] standard. The flexural strength test was carried out on beam specimens of 40x40x160 mm in 3-point bending model in accordance with ASTM C293[12] Cylinder specimens of Ø100/200 mm size were used in the cylinder splitting tests and the tests were carried out in accordance with ASTM C496. Freeze-thaw test was carried out in accordance with TSE CEN/TR 15177 [13] standard. 40x40x160 mm beam specimens were produced for the experiments, and flexural and compressive strengths were determined by taking the average of the three specimens on the 28 day. In the freeze-thaw test according to the TSE CEN/TR 15177 standard, the samples are frozen at -20 °C for 18 hours and then left in the air for 30 minutes. Then it is expected to dissolve in water at 20 °C for 2 hours. In this way, a freeze-thaw cycle is performed. Within the scope of the experimental studies, a total of 30 cycles were applied and the compressive and flexural strengths of the samples were determined after the cycles and the changes that occurred before and after freezing-thawing were examined. Permeability tests are important tests applied to have an idea about the void character and amount of voids of the samples. Significant durability problems arise in materials with permeable voids. In the study, two different test methods were used to determine the permeability properties of the samples. For these experiments, Ø100/200 mm sized cylindrical samples were produced, and the samples extracted from the curing water on the day of the experiment were cut using a diamond saw to obtain Ø100x50 mm sized samples. Water absorption tests were carried out according to ASTM C642[14], capillary water absorption tests were carried out according to ASTM C1585 [15] standards.

**Table 2.** The amount of material in the mixtures in grams (in grams for 1 dm<sup>3</sup>).

Mix. ID	Cement (C)	F-FA	Sand(S)	Water
FA(0)	450	-	1350	225
FA(C10)	405	45	1350	225
FA(C20)	360	90	1350	225
FA(C30)	315	135	1350	225
FA(C5+A5)	427.5	90	1282.5	225
FA(C10+A10)	405	180	1215	225
FA(C15+A15)	382.5	270	1147.5	225
FA(A10)	450	135	1215	225
FA(A20)	450	270	1080	225
FA(A30)	450	405	945	225

### 3. Results and Discussions



### 3.1. Unit Volume Weight Test

The average unit volume weight values of the fresh mixtures are shown in Figure 3. In the simple substitution method in which FA is replaced by cement, unit weight values were lower than the control mixture. In other methods, it was observed that the unit volume weight was higher, especially at low FA ratios, and the values decreased depending on the increase in FA ratio.

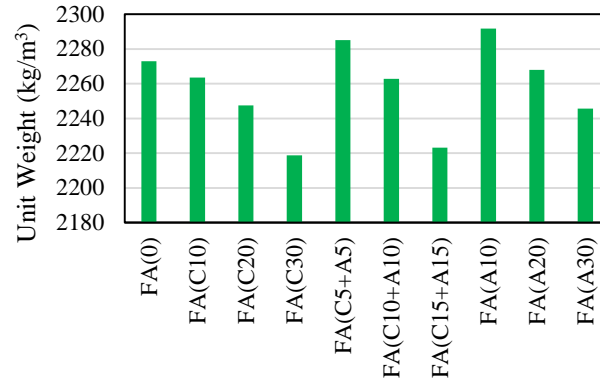


Figure 3. Average unit volume weight values of mixtures.

### 3.2. Spreading Table Test

The average spreading values of the fresh mixtures are shown in Figure 4. To understand the effect of fly ash on the workability of concrete, the water content was adjusted to be constant for all mixtures. When the spreading test results were examined, the mixture dispersion increased as the fly ash ratio increased. In addition, it is noticed that the mixtures formed by the simple substitution method (using an equal amount of FA instead of cement) are more workable than the mixtures prepared by other methods.

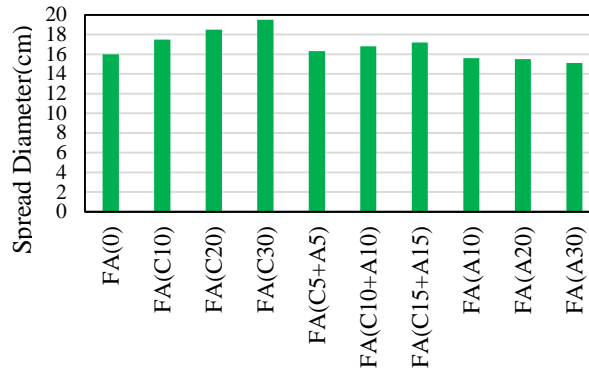


Figure 4. Average spreading diameter values of mixtures.

### 3.3. Compressive Strength Test

The compressive strength test on the hardened samples was carried out on the 7, 28 and 90 days following and the results are given in Table 3.

**Table 3.** 7, 28 and 90-day compressive strengths of the samples.

Mix. ID	Compressive Strength (MPa)		
	7 day	28 day	90 day
FA(0)	29.88	47.54	55.75
FA(C10)	22.61	44.52	52.01
FA (C20)	16.71	41.39	50.33
FA (C30)	15.61	27.54	49.21
FA (C5+A5)	27.00	50.90	70.18
FA (C10+A10)	23.58	46.48	64.61
FA (C15+A15)	19.61	45.15	60.79
FA (A10)	25.65	54.64	74.37
FA (A20)	21.88	51.47	72.04
FA (A30)	18.82	45.77	69.97

In the simple substitution method, the maximum decrease in compressive strength was 12% in the FA(C30) samples, and the minimum decrease was 7% in the FA(C10) samples compared to the reference samples FA(0).

In the partial substitution method, the maximum increase in compressive strength was 26% in the FA(C5+A5) samples, and the minimum increase was 9% in the FA(C15+A15) samples, compared to the reference samples FA(0).

Similarly, in the addition method, the maximum increase rate was 33% in the FA(A10) samples and the minimum increase rate was 25% in the FA(A30) samples compared to the reference samples FA(0). The graphic representation of the compressive strength comparison of the samples is given in the Figure 5.

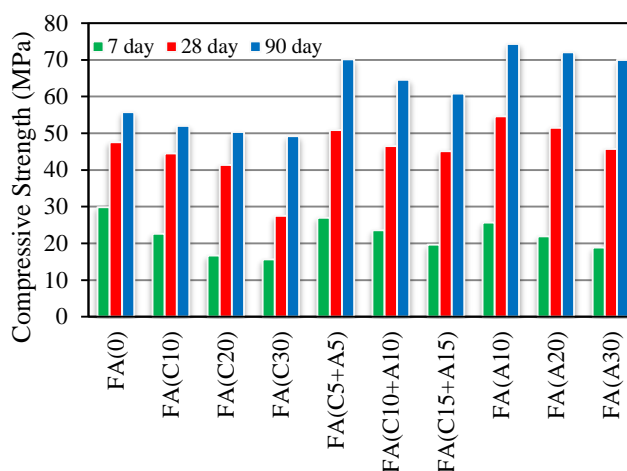


**Figure 5.** Comparison of compressive strength of samples.

- It was observed that mixtures containing 10% FA at different ages had the highest compressive strength among all FA mixtures. When the existing literature studies are examined, it is seen that the use of FA in concrete reduces the mechanical properties of concrete.
- Increases in compressive strength were observed in all mixtures with advancing age. However, the increase in the 90-day compressive strength of the samples prepared in partial replacement and addition methods is quite evident. The amount of cement removed from the mixtures in these two methods is less than in simple replacement methods. The hydration property of cement is higher than FA. However, the use of FA instead of aggregate caused an increase in the amount of binder in the mixture. Thanks to the pozzolanic character of the FA, the long-term continuation of the

hydration event has led to an increase in strength in advancing ages. This can be explained by the positive contribution of pozzolanic activity on compressive strength in later ages.

- When the strength values obtained after the 7, 28 and 90 days curing periods of the mixtures are compared, it is seen that the highest strength values are obtained from the FA(A10) mixture.

### 3.4. Flexural strength test

The flexural strength test on the hardened samples was carried out on the 7, 28 and 90 days following and the results are given in Table 4.

**Table 4.** 7, 28 and 90 days flexural strengths of samples.

Mix. ID	Flexural Strength (MPa)		
	7 day	28 day	90 day
FA(0)	6.86	8.42	10.43
FA(C10)	5.62	7.74	9.22
FA(C20)	4.57	7.54	10.27
FA(C30)	4.06	7.33	9.79
FA(C5+A5)	6.00	8.86	11.28
FA(C10+A10)	4.82	7.55	10.63
FA(C15+A15)	4.53	7.36	12.15
FA(A10)	5.58	8.47	10.93
FA(A20)	5.36	7.46	10.90
FA(A30)	5.04	6.77	10.68

In the simple substitution method, the maximum decrease in flexural strength compared to FA(0) was in FA(C10) samples (12%), while the minimum decrease was in FA(C20) samples (2%).

In the partial substitution method, the maximum increase in flexural strength compared to FA(0) was in the FA(C15+A15) samples (17%), while the minimum increase was in the FA(C10+A10) samples (2%).

Similarly, in addition method, the maximum increase rate compared to FA(0) was in FA(A10) samples (5%), and the minimum increase rate was in FA(A30) samples (2%).

The comparison graph of the 7, 28 and 90 days flexural strength values of the samples is given in Figure 6.

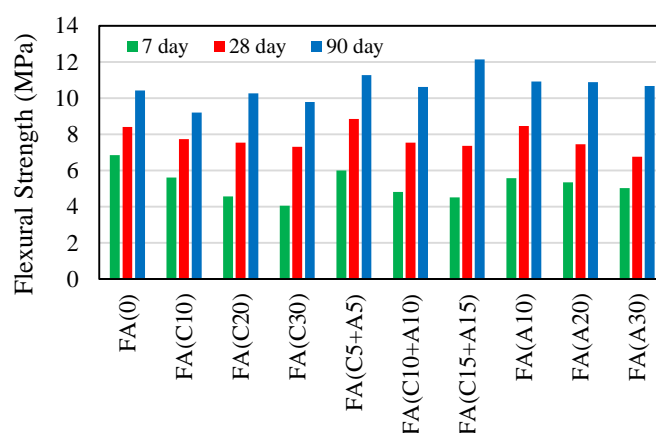


**Figure 6.** Comparison of flexural strengths of samples.

- The flexural strength of the samples prepared by the simple substitution method at increasing FA ratios was lower than the values obtained from the control samples at different ages. In the samples prepared with the partial replacement method and the addition method, only 7-day flexural strength values were lower than the control samples, and the 28 and 90-day strength values were generally higher than the control sample. According to this result, the replacement of FA with cement only

decreases the flexural strength values, partial replacement with cement and aggregate or only with aggregate causes an increase in flexural strengths in advancing ages.

- It has been observed that the increase in flexural strength of FA added samples in advancing ages is less than the increase in compressive strength. At the end of 90 days, the increase in flexural strength was at most 17%, and the increase in compressive strength was 33%.

### 3.5. Cylinder splitting strength test

The results obtained from the experiments are given in Table 5.

**Table 5.** 7, 28 and 90 days cylinder splitting strengths of samples.

Mix. ID	Cylinder Splitting Strength (MPa)		
	7 day	28 day	90 day
FA(0)	3.17	3.95	4.10
FA(C10)	2.87	3.45	3.87
FA(C20)	2.56	3.15	3.49
FA(C30)	1.65	2.85	3.28
FA(C5+A5)	3.13	3.53	4.06
FA(C10+A10)	2.76	3.22	3.66
FA(C15+A15)	2.18	3.00	4.21
FA(A10)	3.01	3.63	3.95
FA(A20)	2.68	3.35	3.59
FA(A30)	1.81	3.10	3.36

In the simple substitution method, the maximum decrease in split strength was found in the FA(C30) samples (20%) and the minimum decrease in the FA(C10) samples (5%) compared to the FA(0).

In the partial substitution method, the maximum increase in split strength was found in FA(C15+A15) samples (3%) and the maximum decrease in FA(C10+A10) samples (11%) compared to FA(0).

Similarly, in the addition method, the maximum decrease rate was found in FA(A30) samples (18%) and the minimum decrease rate was 4% in FA(A10) samples compared to FA(0).

The comparison graph of the 7, 28 and 90 days cylinder splitting strength values of the samples is given in Figure 7.

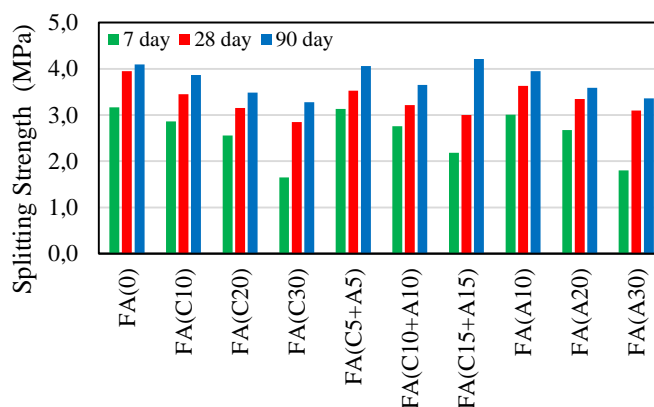


**Figure 7.** Comparison of cylinder splitting strength of samples.

According to the results of the splitting tensile strength test performed on the cylindrical samples, it was observed that the splitting strength values decreased as the FA content increased. The cylinder splitting strength of the FA added mixtures is lower than the control samples, only the 90-day values of the FA(C15+A15) mixture were found to be greater.



### 3.6. Freeze-Thaw test

The compressive and flexural strength results of the FA substituted and control samples with Freeze-Thaw (F-T) cycle and the comparison samples stored in the standard curing are given in Table 6.

**Table 6.** Strength drops under Freeze-Thaw effect.

Mixture ID	No Cycle		30 F-T Cycle		Strength Change	
	Compressive strength (MPa)	Flexural strength (MPa)	Compressive strength (MPa)	Flexural strength (MPa)	Compressive strength (%)	Flexural strength (%)
FA(0)	56.65	11.16	52.93	9.83	7	12
FA(C10)	49.27	11.01	46.20	9.95	6	10
FA(C20)	47.16	10.17	44.70	9.60	5	6
FA(C30)	42.38	9.72	40.59	9.44	4	3
FA(C5+A5)	60.54	11.50	57.20	10.58	6	8
FA(C10+A10)	55.55	10.50	53.17	9.86	4	6
FA(C15+A15)	51.17	9.98	49.80	9.68	3	3
FA(A10)	64.51	11.41	61.81	10.79	4	5
FA(A20)	61.76	10.73	60.26	10.25	2	4
FA(A30)	57.87	10.31	57.16	10.20	1	1

When Table 6 is examined, it is seen that the compressive and flexural strength values decrease as the amount of FA increases, similar to the mechanical strength tests. However, when the percentage changes in the strength losses of the samples are examined, it is seen that the decrease in the strength of the control samples without FA is greater than the decrease in the strength of the samples containing FA. The addition method showed less loss in compressive and flexural strengths.

### 3.7. Water absorption test

The water absorption test was performed on  $\varnothing 100 \times 50$  mm cylindrical samples on the 7th, 28th and 90th days and the percent water absorption values of the samples are given in Figure 8.

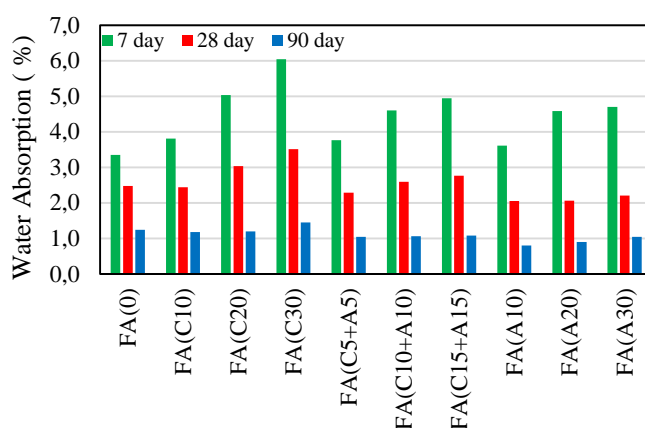
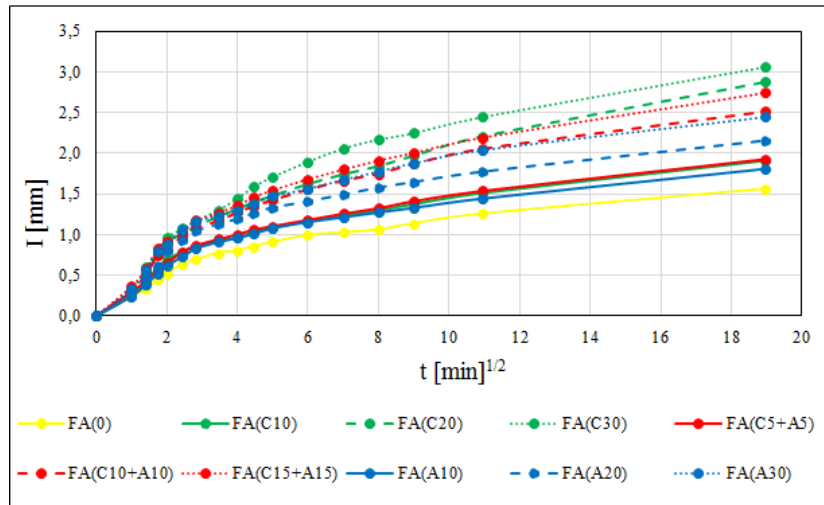


**Figure 8.** Comparison of the water absorption values of the samples.

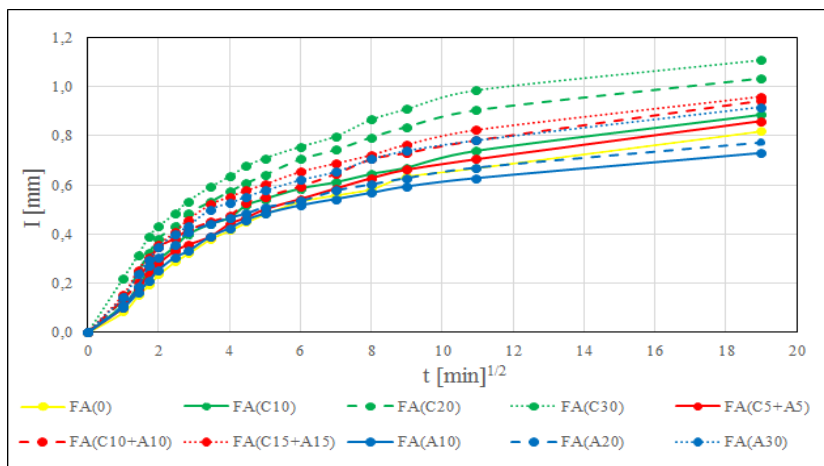
It is observed that as the amount of FA replacement increases, the amount of water absorption in the samples also increases. After 28 and 90 days of curing, it was observed that the water absorption values gradually decreased. This shows that the void structures of the samples decrease during curing. According to FA(0), the maximum decrease rate was 4% in the FA(C20) samples, and the maximum increase was 17% in the FA(C30) samples in the simple substitution method.

### 3.8. Capillary water absorption test

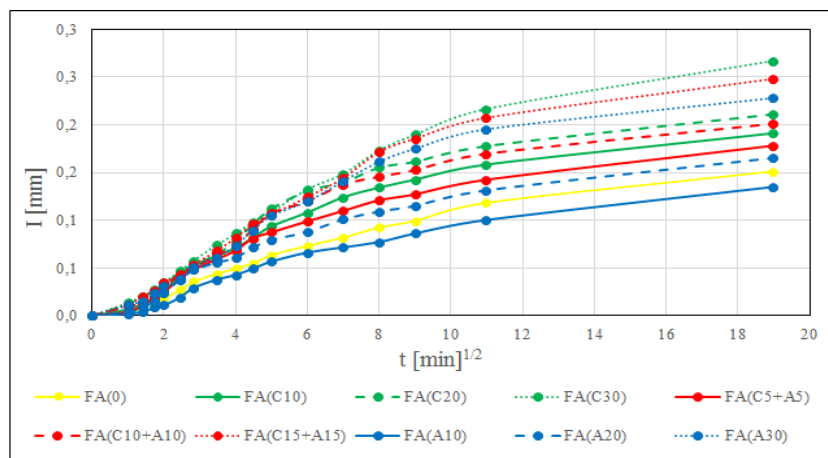
The change in the permeability properties of the samples as a result of the capillary water absorption test is given in Figure 9.



a) 7 days



b) 28 days



c) 90 days

**Figure 9.** Change in capillary absorption values of samples.

- Similar to the water absorption experiments, it was observed that the capillary water absorption results increased as the amount of FA increased, but this increase gradually decreased with advancing age, especially according to the 7-day test results. One of the most important factors affecting the void amount of the samples is the hydration of the cement. As the hydration progresses, the binder paste formed fills the capillary water absorption gaps and disconnects them. Similarly, additional C-S-H gels are formed as a result of the reaction of FA with  $\text{Ca}(\text{OH})_2$ , which is formed as a result of the hydration of the main components of the cement, and this reduces the amount of capillary space. It was observed that the capillary water absorption values gradually decreased after 28 and 90 days of curing due to the slower hydration reaction of the FA.
- In the experiments performed at different ages, it was observed that the lowest capillary water absorption value was obtained from the FA(A10) samples, and the highest values were obtained from the FA(C30) samples.

#### 4. Conclusions

In this study, FA was used in mixtures with three different mixing methods. Slump and unit weight tests were performed to determine the fresh properties of the mixtures, and mechanical, durability and permeability tests were performed to determine the hardened properties. The results obtained as a result of the experiments carried out are presented below.

- 1) Regardless of the rate of substitution for all mixes, the inclusion of FA improved the workability of concrete due to the fineness and spherical shape of its particles.
- 2) It has been observed that the use of large amounts of FA in concrete adversely affects the mechanical properties of the concrete. It is understood that the mechanical properties of mixtures containing 10% FA develop better. However, it was observed that the strength development accelerated in the samples prepared by the addition method or partial replacement method after the advancing curing periods and the FA additive had a positive effect on the behavior.
- 3) Decreases in flexural and compressive strength values of control samples after freeze-thaw cycles were higher than those of FA substituted samples. Accordingly, it can be said that as the FA content increases, the resistance of the samples to freeze-thaw increases. This can be explained by the fact that FA fills the voids in the sample better and increases the freeze-thaw resistance.
- 4) As a result of the permeability tests, the permeability properties of the samples prepared by the addition method were generally lower than the other mixing methods. According to this, it is understood that the replacement of FA with aggregate instead of cement has a positive effect in terms of reducing the amount of voids in the samples.

The use of FA as a binder material and reducing the amount of cement has positive results in many ways. By replacing FA with cement, it is possible to obtain more economical and environmentally friendly concrete. In addition, it is thought that the use of some FA instead of fine aggregate used in concrete will contribute to the efficient use of FA, which is a waste material, to the industry, and to reduce its effects on environmental pollution and storage costs.

**Peer-review:** Externally peer - reviewed.

**Author contributions:** Concept – A.A., M.A.; Data Collection &/or Processing – M.A.; Literature Search – A.A., M.A.; Writing - A.A.

**Conflict of Interest:** This work has been partly presented at the ICENTE'21 (International Conference on Engineering Technologies) held in Konya (Turkey), November 18-20, 2021. This

study was produced from the Master thesis entitled " Farklı Karışım Yöntemleri İle Kullanılan F Tipi Uçucu Külünün Beton Özelliklerine Etkilerinin İncelenmesi" by Marvan ALITHAWI, which was accepted in 2021.

**Financial Disclosure:** The authors declared that this study has received no financial support.

## References

- [1] A. K. Saha, "Effect of class F fly ash on the durability properties of concrete," Sustainable environment research, vol. 28, no. 1, pp. 25-31, 2018.
- [2] J. Rissanen, K. Ohenoja, P. Kinnunen, and M. Illikainen, "Partial replacement of portland-composite cement by fluidized bed combustion fly ash," Journal of Materials in Civil Engineering, vol. 29, no. 8, p. 04017061, 2017.
- [3] R. Siddique, "Performance characteristics of high-volume Class F fly ash concrete," Cement and Concrete Research, vol. 34, no. 3, pp. 487-493, 2004.
- [4] A. K. Saha and P. K. Sarker, "Sustainable use of ferronickel slag fine aggregate and fly ash in structural concrete: Mechanical properties and leaching study," Journal of Cleaner Production, vol. 162, pp. 438-448, 2017.
- [5] S. W. M. Supit and F. U. A. Shaikh, "Durability properties of high volume fly ash concrete containing nano-silica," Materials and structures, vol. 48, no. 8, pp. 2431-2445, 2015.
- [6] A. Mardani-Aghabaglou, Ö. Andiç-Çakir, and K. Ramyar, "Freeze–thaw resistance and transport properties of high-volume fly ash roller compacted concrete designed by maximum density method," Cement and Concrete Composites, vol. 37, pp. 259-266, 2013.
- [7] E. E. Berry and V. M. Malhotra, Fly ash in concrete. Energy, Mines and Resources Canada, CANMET, Ottawa, pp. 223-229., 1986.
- [8] V. Akyüncü, "F ve C tipi uçucu küllerin çimento ile ikame edilmesiyle üretilen betonların mekanik ve dayanıklılık özelliklerinin karşılaştırılarak incelenmesi," 2012.
- [9] A. C618, Standard specification for coal fly ash and raw or calcined natural pozzolan for use in concrete, in American society for testing and materials, 2003: ASTM international West Conshohocken, PA, USA.
- [10] ASTM C230, Standard specification for sample and testing fly ash or natural pozzolan for use as a mineral admixture in Portland cement," Annual Book of ASTM Standard, vol. 4, p. 172, 1997.
- [11] ASTM C39, Standard test method for compressive strength of cylindrical concrete specimens, American Society for Testing and Materials, West Conshohocken, Pa., 2012.
- [12] ASTM C293, Standard Test Method for Flexural Strength of Concrete (using simple beam with center-point loading), American Society for Testing and Materials, West Conshohocken, Pa, 1979.
- [13] TSE CEN/TR 15177, Testing the Freeze-Thaw Resistance of Concrete-Internal Structural Damage, Turkish Standards Institute, Ankara, Turkey, 2011.
- [14] ASTM C642-13, Standard test method for density, absorption, and voids in hardened concrete, American Society for Testing and Materials, West Conshohocken, Pa, 2013.
- [15] ASTM C1585-13, Standard Test Method for Measurement of Rate of Absorption of Water by Hydraulic-Cement Concretes, American Society for Testing and Materials, West Conshohocken, Pa, 2013.



# Modification of PVDF Membranes Using Dopamine/Zinc Oxide Powders for Lead Removal from Aqueous Media

<sup>1</sup> İrem Sevim Üçel , <sup>\*1</sup> Elif Demirel 

<sup>1</sup> Eskisehir Technical University, Department of Chemical Engineering, Eskisehir/Turkey.

\* Corresponding author, e-mail: elifyildiz@eskisehir.edu.tr, +90 222 3213550/6509

Submission Date: 15.01.2022

Acceptation Date: 21.03.2022

**Abstract** - Ultrafiltration (UF) has long been a leading separation technology with a strong historical track record for a wide range of applications such as the treatment of ground water, surface water and wastewater. The utilization of nanofillers in the fabrication of organic UF membranes has brought about breakthrough progress in membrane science and technology. The present study demonstrates modification of polyvinylidene fluoride (PVDF) membranes using zinc oxide (ZnO), polydopamine (PDA), and ZnO/PDA powders by blending and coating methods, respectively. ZnO/PDA nanoparticles were synthesized by the sol-gel method and were characterized using X-Ray Diffraction in comparison to ZnO and dopamine (DA) powders. Filtration performance of the fabricated membranes were determined in terms of water flux, sodium alginate (SA) rejection, and anti-fouling properties. Moreover, lead ( $Pb^{+2}$ ) ions were chelated with chitosan following rejection of the formed lead-chitosan complexes from the fabricated membranes. Although water flux and SA rejections of the pristine PVDF membrane in the presence of different powders could not be substantially improved, anti-fouling properties could be enhanced markedly. PVDF/ZnO/PDA membrane was found to exhibit the best separation performance with 92% flux recovery ratio and 97% SA rejection and had the highest lead-chitosan removal of 88.5% from aqueous solutions. The enhanced separation performance of the PVDF/ZnO/PDA membrane was revealed by SEM images, which demonstrated remarkable morphological changes such as more porous, longer and interconnected finger-like formations compared with the pristine PVDF membrane.

**Keywords:** Membrane, Nanoparticle, Zinc Oxide, Dopamine, Lead removal

## Sulu Ortamlardan Kurşun Giderimi için PVDF Membranların Çinko Oksit/Dopamin ile Modifiye Edilmesi

**Öz** - Ultrafiltrasyon (UF), uzun zamandır yeraltı suyu, yüzey suyu ve atık su arıtımı gibi çok çeşitli uygulamalarda kullanılan güçlü bir geçmişe sahip, lider bir ayırma teknolojisi olmuştur. Organik UF membranlarının üretiminde nano dolgu maddelerinin kullanılması, membran bilimi ve teknolojisinde çığır açan ilerlemeler sağlamıştır. Bu çalışmada, çinko oksit (ZnO), polidopamin (PDA) ve ZnO/PDA tozları sırasıyla harmanlama ve kaplama yöntemleri ile poliviniliden florür (PVDF) membranlarının modifikasyonu için kullanılmıştır. ZnO/PDA nanoparçacıkları sol-jel yöntemi ile sentezlendikten sonra, X-Işını Kırınım ile ZnO ve dopamin (DA) tozları ile karşılaştırılarak karakterize edilmiştir. Üretilen membranların filtrasyon performansı, su akısı, sodyum aljinat (SA) giderimi ve kirlenmeye karşı direnç özellikleri ile belirlenmiştir. Ayrıca, kurşun ( $Pb^{+2}$ ) iyonlarının kitosan ile kompleks haline getirilmesinden sonra oluşan kurşun-kitosan komplekslerinin membranlardan giderimi test edilmiştir. Saf PVDF membranın su akısı ve SA giderimi farklı tozlar varlığında kayda değer bir miktarda arttırılamasa da, kirlenmeye karşı direnç özellikleri önemli ölçüde iyileştirilmiştir. PVDF/ZnO/PDA membranının %92 su akısı geri kazanım oranı ve %97 SA giderimi ile en iyi ayırma performansı gösterdiği ve sulu çözeltilerden en yüksek kurşun-kitosan giderimini (%88,5) sağladığı belirlenmiştir. PVDF/ZnO/PDA membranının iyileştirilmiş ayırma performansı, saf PVDF membrana kıyasla daha gözenekli, uzun ve birbirine bağlı parmaklı oluşumların varlığını gösteren SEM görüntüleri ile ortaya konulmuştur.

**Anahtar kelimeler:** Membran, Nanotanecek, Çinko Oksit, Dopamin, Kurşun giderimi

<sup>1</sup> Corresponding author: Tel: +90 222 3213550/6509

E-mail: elifyildiz@eskisehir.edu.tr,

## 1. Introduction

In recent years, the limited availability of freshwater, which plays an important role in human life and the ecosystem, has led to a great interest in water and wastewater treatment technologies [1]. Surface and groundwater pollution, which has become a global environmental problem due to rapid population growth and global industries reveals the importance of wastewater treatment [1,2,3]. Besides, wastewater treatment is an important issue that needs to be addressed, as only 0.5% of the water in the world is fresh water [4,5]. The release of heavy metal ions, which are toxic even at low levels and cause damage to human health and the aquatic ecosystem, into water sources without adequate treatment is one of the main causes of surface and groundwater pollution [1,6,7,8]. In particular, heavy metals such as arsenic, cadmium, and lead must be removed from wastewater before they accumulate in living organisms. These non-biodegradable heavy metals have become an issue of great concern due to their hazardous effects. Especially lead is one of the most toxic metal pollutants and lead pollution has become an issue of great concern due to its large discharge and high mobility in an aqueous environment, and easy accumulation in the human body. Lead exposure is known to damage the nervous system, kidneys, and reproductive system, and excessive lead exposure can lead to headaches, stomach pain, cancer, and even death. Therefore, The World Health Organization (WHO) ascribes lead as one of the greatest public health issues [8,9,10,11]. According to WHO, the maximum contaminant level (MCL) of  $Pb^{+2}$  in drinking water should be less than 15  $\mu\text{g/L}$  [12].

Many technologies such as chemical precipitation, coagulation-flocculation, adsorption, membrane technology, ion exchange, and electrochemical purification are applied in the separation of lead from water [9]. In the last decades, membrane separation processes have become widespread owing to a number of advantages including high efficiency, easy integration with other separation techniques, feasible scale-up, and improvable fabrication techniques [13,14]. The most common membrane processes particularly applied for water treatment are microfiltration (MF), ultrafiltration (UF), nanofiltration (NF), reverse osmosis (RO), electrodialysis, and membrane distillation. NF and RO membranes are used in various water treatment processes and heavy metal removal due to their appropriate pore sizes, but they require higher pressure and energy consumption compared to UF and MF processes. However, the application of UF and MF processes for the removal of heavy metals is limited due to their large pore structure. Therefore, modification of UF/MF membranes is necessary to enable the removal of heavy metal ions from aqueous solutions [11]. Membrane fouling, which is the most limiting factor for wider applications of membrane processes, causes a serious reduction in permeability and considerable technical problems such as requirement for higher operating pressures and harsh cleaning conditions [6,11,15]. The incorporation of fillers into the membrane matrix by physical blending, chemical grafting, and surface modifications has been demonstrated to enhance the hydrophilicity, permeability, and contamination resistance of the membrane [16, 17]. Zinc oxide (ZnO) has been used as a membrane filler for its exceptional physical and chemical properties as well as its antibacterial activity [16,18]. Dopamine (DA), which is a very hydrophilic molecule and biocompatible with catechol and amino groups, has recently attracted considerable attention in the modification of membranes. DA is a highly suitable material for surface modification since it self-polymerizes to polydopamine (PDA) under alkaline conditions on almost any surface regardless of its morphology or chemical composition [19, 20, 21]. PDA coating has several advantages such as electrostatic attraction, chelation, and covalent bonds with the surface [21]. Some studies on the synthesis of ZnO/PDA powders and their incorporation into membrane matrix with an aim to enhance filtration performance have been reported in the literature. Tavakoli et al. synthesized a new composite material by decorating ZnO nanoparticles with PDA and reported that the oxygen atoms in the ZnO were bonded to hydrogen atoms in the amine and catechol functional groups of the PDA molecule through hydrogen intermolecular forces. They also reported that coating ZnO nanoparticles

with PDA did not result in a change in their morphology, but some spherical precipitations on the surface of the nanoparticles confirmed the presence of PDA coating [22]. Zhang et al. incorporated PDA-modified titanium dioxide ( $\text{TiO}_2$ ) fillers into the PVDF membrane matrix by blending method and also coated the membrane surface with PDA and reported that water flux of pristine PVDF membrane increased by 312% and 287% by coating the membrane using 2 g/L DA solution and with the addition of a PDA-modified  $\text{TiO}_2$  additive by blending method, respectively [20].

In addition to the membrane modification methods mentioned above such as incorporation of fillers into the membrane matrix by physical blending, chemical grafting, and surface modifications, the complexation–membrane filtration or polymer-assisted ultrafiltration (PEUF) is another noteworthy technique for heavy metal removal from water [23]. The overall idea of this method is based on binding the cationic heavy metals to a water-soluble polymer to increase the molecular weight of the heavy metal so as to retain even trace amounts of metal on the membrane surface [23, 24]. The use of polymers containing carboxylic or amine groups as complexing agents such as carboxyl methylcellulose (CMC) [25], polyvinylethylenimin (PEI) [26,27], polyvinyl alcohol (PVA) [27], poly(acrylic acid) (PAA) [28], and chitosan have been reported to be capable of removing several heavy metals from wastewater. Chitosan is a natural biodegradable polymer that can be used to bind metal ions by interacting with them through  $-\text{OH}$  and  $-\text{NH}_2$  functional groups. That is, the stoichiometry of chitosan-metal complex is based on the number of amine groups ( $\text{R}-\text{NH}_2$ ) bound to the metal ions [29]. The formation of probable metal-chitosan complex is given in Figure 1. Metal-complexing agent ratio and pH of the solution are significant parameters that affect the removal efficiency of the metal, while membrane characteristics and operating conditions of the process influence the reusability of the membrane. Polymer can easily be removed from the complex subsequent to filtration.

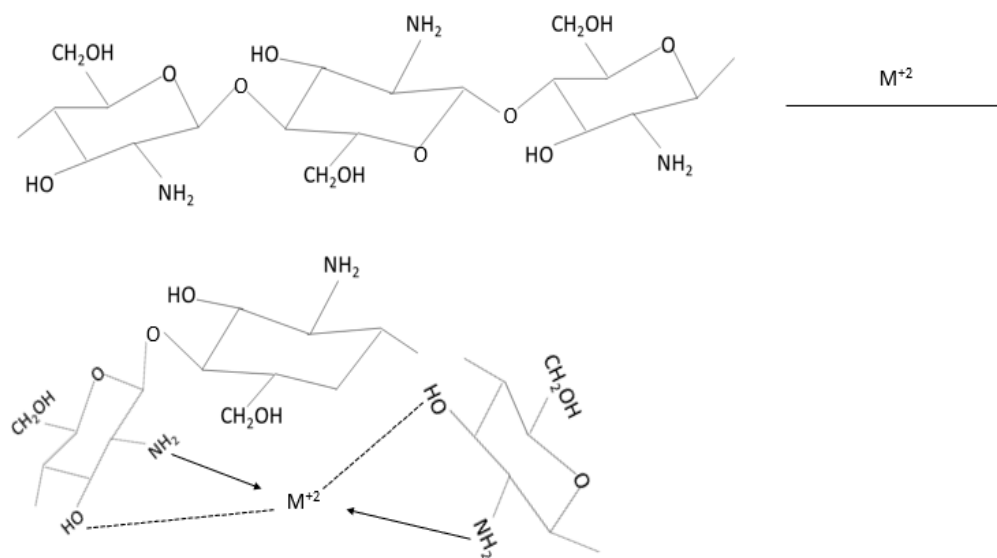


**Figure 1.** Probable molecular structure of the metal ( $\text{M}^{+2}$ )-chitosan complex.

Although several studies have attempted to incorporate different fillers including ZnO, DA, PDA along with their combined forms into polymer-based membrane matrices, utilizing them for heavy metal removal from aqueous media using polymer assisted ultrafiltration technique is still lacking in the literature. Present study aims at fabricating polyvinylidene fluoride (PVDF) based nanocomposite membranes modified with ZnO, PDA, and ZnO/PDA powders using the phase inversion technique for the investigation of their separation performance not only in terms of lead removal from aqueous solutions but also other filtration characteristics such as water flux and anti-fouling properties in

comparison to that of pristine PVDF membrane. In this context, ZnO and ZnO/PDA powders were incorporated into the membrane matrix in certain proportions by blending method, and PDA was added by coating method. Membrane characterization was carried out by exploring their morphology, porosity, mean pore size, bulk thermal stability, and mechanical strength using several equipments and analytical techniques. In addition, as a complexing agent, chitosan was employed in polymer-assisted ultrafiltration process to remove lead ions from aqueous solutions and the highest lead-chitosan removal performance was highlighted by investigating the main operating conditions such as lead: chitosan ratio and pH of the solution.

## 2. Materials and Methods

### 2.1. Chemicals

PVDF (Molecular Weight (MW) = 534,000 g.mol<sup>-1</sup>), polyethylene glycol (PEG, MW= 6,000 Da), 3,4-dihydroxyphenethylamine (dopamine hydrochloride), Tris(hydroxymethyl) aminomethane (Tris), ZnO (particle size <100 nm), chitosan (from shrimp shells, ≥75%) and sodium alginate (SA) were purchased from Sigma-Aldrich. 1-Methyl-2-pyrrolidone (NMP, >99%) and lead nitrate (PbNO<sub>3</sub>) were supplied by Alfa Aesar and Carlo Elba, respectively. All the other chemicals were used as received without further treatment. Deionized (DI) water was produced by a Milli-Q system (Millipore, US).

### 2.2. Synthesis of ZnO/PDA Powders

ZnO/PDA nanoparticles were prepared by the sol-gel method using ZnO and dopamine hydrochloride (DA) [20]. 0.5 g ZnO nanoparticle was added into 50 mL DI water and ultrasonically dispersed for 30 min. Besides, a Tris solution with a concentration of 1.0 g/L was prepared and its pH was adjusted to 8.5 using either NaOH or HNO<sub>3</sub> solutions. 0.5 g DA was ultrasonically dispersed in 200 mL Tris-HCl buffer. PDA solution was obtained by self-polymerization of dopamine in tris-HCl buffer solution since hydrophilic DA can self-polymerize under alkaline conditions. The ZnO suspension prepared in the first step and DA solution were mixed in a magnetic stirrer at room temperature for 24 h. The sediment obtained was centrifuged at 5000 rpm and then filtered under vacuum. Finally, the ZnO/PDA nanoparticles were washed with ethyl alcohol and DI water three times and then dried at 85 °C prior to characterization.

### 2.3. Fabrication of Membranes

Pristine PVDF, ZnO, and ZnO/PDA doped nanocomposite membranes were fabricated using blending and phase inversion with immersion precipitation technique [20]. For the preparation of membrane casting solutions, ZnO or ZnO/PDA nanoparticles (0.5wt. % of PVDF) were added into NMP and stirred in an ultrasonic bath for 3 and 1 hours, respectively. After the addition of PVDF and PEG, the resulting mixture was stirred at 70°C for 48 hours to get a homogenous solution. The casting solution was poured on a glass plate and cast into a film of 150 μm thickness using an adjustable casting blade and the thin film was immediately immersed into a coagulation bath of nonsolvent water. Membrane was transferred into a container of fresh water to get rid of the residual NMP. All the membranes were dried in an oven at 50°C under vacuum for 24 hours before the characterization tests [20]. The viscosity of each casting solution was measured at least twice using a Rotational Viscometer (Fungilab, Smart R, Spain) at room temperature with 50 rpm speed and 60% torque, and the average values are reported [30].

To investigate the effect of PDA coating, a pristine PVDF membrane was immersed into a 2 g/L DA solution for 24 hours. For this purpose, 0.4 g DA was added into 200 mL ethanol-Tris-HCl buffer solution (1:1, v/v) and the pH was adjusted to 8.5. The solution was stirred at 25°C for 24 hours, and the DA in the solution was self-polymerized into PDA [31]. Finally, nanocomposite membranes were washed with DI water and ethanol to remove the residual PDA particles [32].



The compositions of the membranes prepared by blending and coating methods are listed in Table 1.

**Table 1.** The compositions and viscosities of the casting solutions.

Membran ID	PVDF (g)	PEG (g)	NMP (g)	Additives (%wt.)	Viscosity (Pa.s)
PVDF	9	0.5	40.500	-	9.7
PVDF/ZnO	9	0.5	40.455	0.5 ZnO	10.8
PVDF/ZnO/PDA	9	0.5	40.455	0.5 ZnO/PDA	14.6
PVDF/PDA	9	0.5	40.455	PDA	-

## 2.4. Characterization

The morphology of the top surface and cross-section of the pristine and nanocomposite membranes were determined by Field Emission-Scanning Electron Microscopy (FE-SEM) (Hitachi Regulus 8230).

Membrane porosity was calculated by gravimetric method using the following equation [33].

$$\varepsilon = \frac{W_w - W_d}{\rho_w(\pi r^2 l)} \times 100\% \quad (1)$$

where  $W_w$  and  $W_d$  are the masses of the wet and dry membranes (g), respectively,  $\rho_w$  is the density of the water at room temperature ( $\text{g/cm}^3$ ),  $r$  is the radius (cm), and  $l$  is the thickness (cm) of the membrane.

The mean pore diameter of the membrane was calculated using the Guerout-Elford-Ferry equation given below [34, 35].

$$a = \sqrt{\frac{(2.9 - 1.75\varepsilon) * (8\mu l Q_w)}{\varepsilon A \Delta P}} \quad (2)$$

where  $a$  denotes the mean pore diameter (m),  $\varepsilon$  is the porosity,  $\mu$  is the viscosity of the filtrated water at room temperature (Pa.s),  $Q_w$  is the water flux ( $\text{m}^3/\text{s}$ ),  $l$  is the thickness (m),  $A$  is the filtration area of the membrane ( $\text{m}^2$ ), and  $\Delta P$  is the transmembrane pressure (Pa).

The crystallinity of ZnO, DA, ZnO/PDA powders, and the fabricated membranes nanocomposite membranes were characterized by X-ray diffraction (XRD) analysis (Rigaku Miniflex 600). The addition of ZnO and ZnO/PDA fillers and the effect of PDA coating on the thermal behavior of the pristine membrane were investigated by thermogravimetric analysis (TGA, Perkin Elmer (STA) 6000). The functional groups of pristine and nanocomposite membranes were characterized by Fourier-Transform Infrared Spectroscopy (FTIR) (ThermoFisher Science, Nicolet iS10). The mechanical stabilities of the membranes were determined using a single-column mechanical tensile tester (Instron 5944) and the results are reported in terms of Young modulus (MPa), tensile strength (MPa), and elongation at break (%).

## 2.5. Separation Performance of Membranes

Water flux values of the membranes were measured using a dead-end ultrafiltration system. A membrane sample with an effective surface area of  $28.7 \text{ cm}^2$  was placed in a stirred cell (Millipore, Amicon Stirred Cell) of 200 mL capacity. Each membrane was compacted at 0.21 MPa for 1 h before

the ultrafiltration experiments. Then the pressure was lowered to 0.07 MPa and all the ultrafiltration experiments were carried out at this transmembrane pressure (TMP). The solution in the cell was stirred at 400 rpm to minimize concentration polarization [33]. Permeate was weighed in one-minute time intervals using a balance, and the data was collected and stored using a software (Radwag, Poland). The water flux was calculated using the following equation.

$$J_{w,1} = \frac{\Delta V}{A * \Delta t} \quad (3)$$

where  $J_{w,1}$  is the pure water flux ( $L/m^2h$ ),  $\Delta V$  is the volume change of the permeate (L) in one-minute time interval,  $A$  is the membrane filtration area ( $m^2$ ), and  $\Delta t$  is the permeation time (h).

The water flux values of the membranes were determined at different TMP (0.07-0.27 MPa) to investigate the compaction behavior and stability of membranes.

Rejection tests of the fabricated membranes were carried out using SA solution with a concentration of 20 mg/L. Concentrations of the collected permeate and feed for each membrane were determined quantitatively using a TOC-L Analyzer (Shimadzu, Japan) and calculated by the following equation [33].

$$R(\%) = \left(1 - \frac{C_p}{C_f}\right) \times 100 \quad (4)$$

where  $C_p$  and  $C_f$  are the concentrations of the permeate and feed solutions, respectively.

To assess the anti-fouling properties, a membrane sample was subjected to SA solution for 4 hours, washed with DI water and the flux was measured again. The anti-fouling property was interpreted in terms of flux recovery ratio (FRR), which was calculated using the equation below [36].

$$FRR (\%) = \frac{J_{w,2}}{J_{w,1}} \times 100 \quad (5)$$

where  $J_{w,1}$  and  $J_{w,2}$  denote the pure water flux and water flux after the SA fouling test, respectively.

During SA filtration, foulant molecules are adsorbed on the surface and inside fingerlike pores of the membrane structure that in turn leads to a flux decline. To understand the fouling resistances of the membranes, the resistance-in-series model was used [17, 36].

$$R_t = R_m + R_r + R_{ir} = \frac{\Delta P}{\mu * J_{w,2}} \quad (6)$$

where  $R_t$  denote the total fouling resistance of the membrane ( $m^{-1}$ ), ( $R_m$ ) is the intrinsic membrane resistance ( $m^{-1}$ ),  $R_{ir}$  is the irreversible fouling resistance ( $m^{-1}$ ),  $R_r$  is the reversible fouling resistance ( $m^{-1}$ ),  $J_{w,2}$  is the water flux after the SA fouling test ( $m^3/m^2.s$ ),  $\Delta P$  is the corresponding transmembrane pressure in (Pa) and  $\mu$  is the dynamic viscosity of water at room temperature (Pa.s) [17]. Each resistance was computed using the following equations.

$$R_m = \frac{\Delta P}{\mu * J_{w,1}} \quad (7)$$

$$R_r = \frac{\Delta P}{\mu * J_{w,3}} - R_m \quad (8)$$

$$R_{ir} = R_t - R_m - R_r \quad (9)$$

where  $J_{w,3}$  denotes the pure water flux ( $\text{m}^3/\text{m}^2 \cdot \text{s}$ ) measured after backwashing of membranes for 30 min.

## 2.6. Lead Removal Efficiency

The performance of the fabricated membranes was tested for  $\text{Pb}^{+2}$  removal from aqueous solutions using polymer assisted ultrafiltration method. For this purpose,  $\text{Pb}^{+2}$  ions were bound to chitosan to form a lead-chitosan complex before the filtration experiments [29, 37]. For this purpose, 10 ppm  $\text{Pb}^{+2}$  solution was added to chitosan solutions of different concentrations (500 ppm and 1000 ppm) in 0.4 vol% acetic acid, and the resulting mixture is stirred for 24 hours to form a complex. pH was adjusted to the desired value using either 0.1 M NaOH or 0.1 M  $\text{HNO}_3$  solutions. The concentrations of the permeate and the feed were determined using UV-Vis Spectrophotometer (Shimadzu, UV 2600/2700) at a wavelength of 200 nm.

## 3. Results and Discussions

### 3.1. Characterization of Nanoparticles

The crystallinity of ZnO, DA, and ZnO/PDA powders was characterized by XRD analysis. As shown in Figure 2a, the peaks observed at  $31.82^\circ$ ,  $34.46^\circ$ ,  $36.3^\circ$  corresponded to the hexagonal wurtzite crystal structure of ZnO [22, 38, 39, 40]. The peaks observed at  $23.1^\circ$ ,  $25.9^\circ$ ,  $26.7^\circ$ ,  $27.7^\circ$ ,  $28.7^\circ$ , and  $31.3^\circ$  in Fig. 2b were attributed to the characteristic peaks of DA that confirmed its crystalline structure [41]. XRD pattern of ZnO/PDA (Fig. 2c) powder had diffraction peaks similar to those of ZnO nanoparticles indicating that PDA did not cause any destruction during its interaction with ZnO and the crystalline structure of DA was degraded due to its self-polymerization into PDA [22, 41].

### 3.2. Effects of Environmental Conditions on Adsorption Study

The surface and cross-section images of the pristine and nanocomposite membranes were determined by SEM analysis and the results are given in Figure 3 and Figure 4, respectively. As shown in Figure 3, the pristine PVDF membrane exhibited the largest surface porosity with some defects and nonuniform distribution of pores and the number of the surface pores decreased with the addition of nanoparticles into the membrane matrix. A significant amount of ZnO clusters (as highlighted with yellow circles in Fig. 3b) were observed on the surface of the PVDF/ZnO membrane, indicating that ZnO was not uniformly distributed in the matrix due to its poor interaction with PVDF [42]. However, the incorporation of functional ZnO/PDA powders to the membrane matrix enhanced the interaction of PDA chains with PVDF, which in turn led to a uniform distribution surface pores in the matrix. As also shown in Figure 3c, negligible amount of aggregates (shown with yellow circles in Fig. 3c) were detected on the membrane surface. PVDF/PDA membrane had the lowest porosity with a significant amount of PDA clusters on the coating surface (shown with yellow circles in Fig. 3d) [43].

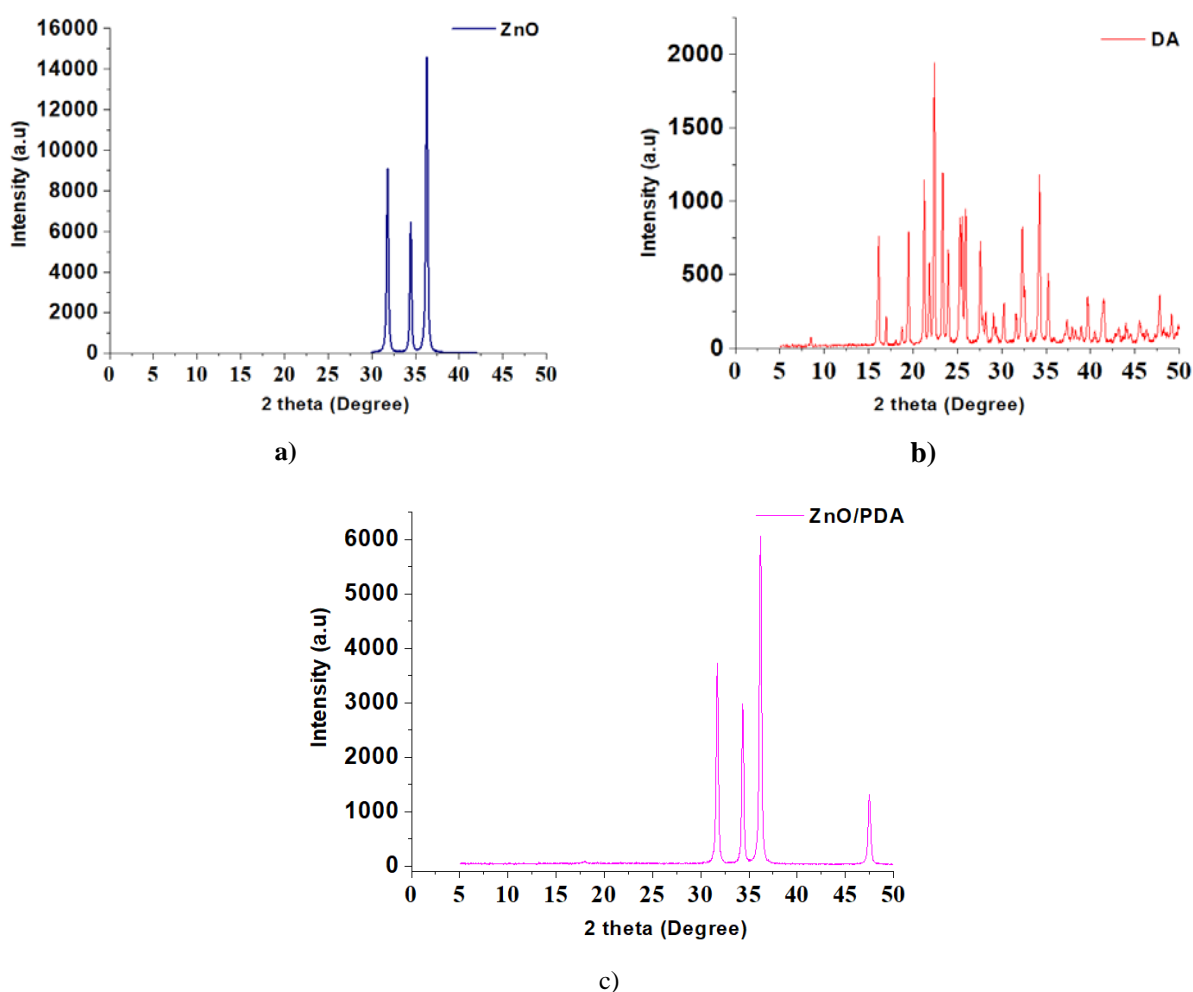


**Figure 2.** XRD patterns of nanoparticles a) ZnO b) DA c) ZnO/PDA.

As seen in Figure 4, all membranes consisted of an active upper layer with a low pore density and a support layer containing larger macropores, where the active upper layer separated by an orange line from the support layer [13,44]. The finger-like structures (yellow circles in Fig. 4) of the pristine PVDF membrane extended along the membrane cross-section. However, with the addition of ZnO to the matrix, as the size of the finger-like pore sizes were shortened, macroporous gaps (red circles in Fig.4b) occurred in the lower sections. However, PVDF/ZnO/PDA membrane showed finger-like formations, which extended along the cross-section, similar to that of the pristine PVDF membrane. Due to the non-uniform distribution of PDA powders on the coating surface, apparently the finger-like pores in the cross-section of the PVDF/PDA membrane was almost eliminated, and instead macroporous gaps (red circles in Fig.4d) were formed at the membrane base.

Some morphological properties of the fabricated membranes are given in Table 2. The porosity and mean pore diameter of the PVDF/ZnO nanocomposite membrane (84.6% and 14.1 nm, respectively) were similar to those of the pristine PVDF membrane (85.4% and 14.4 nm, respectively) since ZnO nanoparticles could not be distributed evenly over the membrane surface and finger-like pores (Table 2). The PVDF/ZnO/PDA membrane had the highest porosity (96.1%) with a comparatively smaller mean pore size indicating the existence of a large number of smaller pores in the matrix. The mean pore diameter (10.5 nm) of the PVDF/PDA membrane was the lowest since a long coating time may have caused the formation of a thick PDA layer on the surface or probably PDA aggregates clogged the membrane pores [45]. The morphological properties of membranes were in good agreement with the water permeability values.



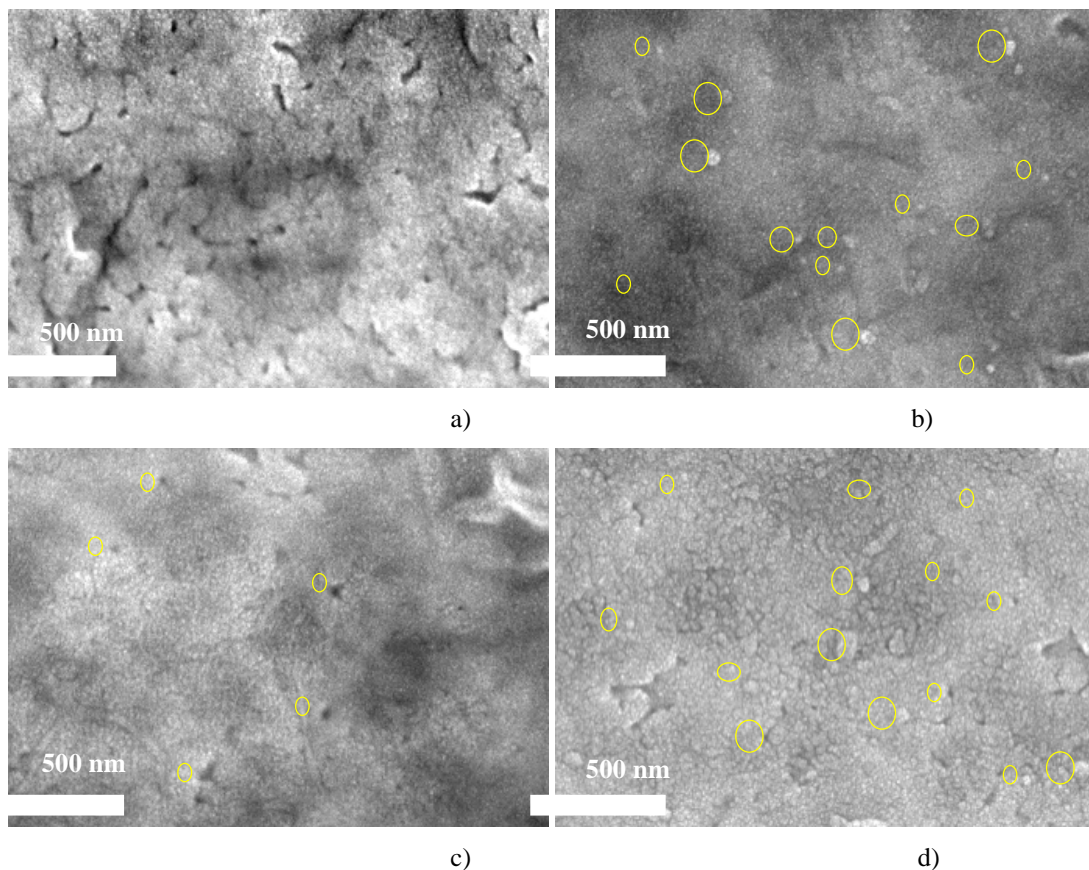


**Figure 3.** Surface SEM images of the membranes a) PVDF b) PVDF/ZnO c) PVDF/ZnO/PDA d) PVDF/PDA.

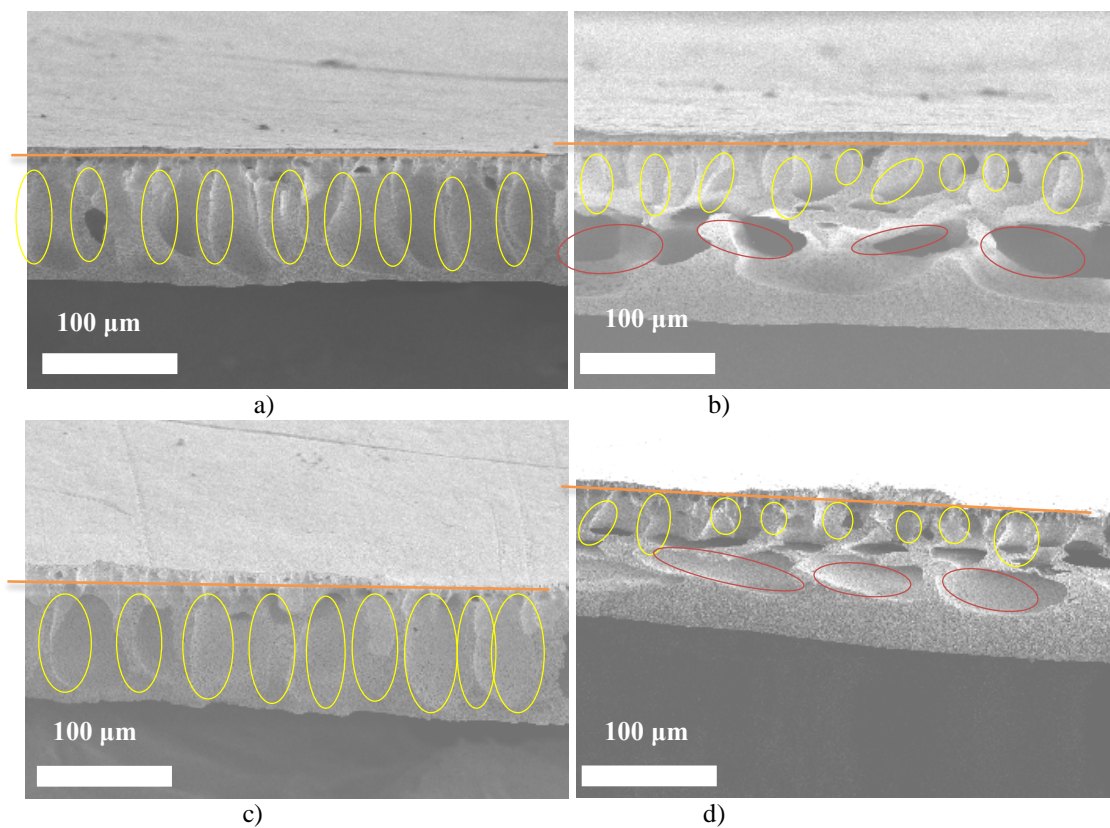


**Figure 4.** Cross-section SEM images of the membranes a) PVDF b) PVDF/ZnO c) PVDF/ZnO/PDA d) PVDF/PDA.



**Table 2.** Some morphological properties of membranes.

Membran ID	Porosity (%)	Mean pore diameter (nm)	Thickness ( $\mu\text{m}$ )
PVDF	85.4	14.4 $\pm$ 0.8	73 $\pm$ 2
PVDF/ZnO	84.6	14.1 $\pm$ 0.5	77 $\pm$ 2
PVDF/ZnO/PDA	96.1	12.8 $\pm$ 0.4	75 $\pm$ 2
PVDF/PDA	93.3	10.5 $\pm$ 0.5	74 $\pm$ 2

The crystallinity of the pristine PVDF membrane and nanocomposite membranes were characterized by XRD analysis. It can be seen from Figure 5 that, the characteristic diffraction peaks of the PVDF membrane observed at 18.8°, 21.1°, and 39° correspond to (020) (110) and (131) planes of the PVDF polymer. The fact that the peak intensity increased in Figure 5b could be attributed to the non-uniform distribution of ZnO nanoparticles in the membrane matrix [46]. The XRD patterns of PVDF/ZnO/PDA and PVDF/PDA membranes were similar to that of pristine PVDF membrane with no significant changes in the crystal structure [47, 48].

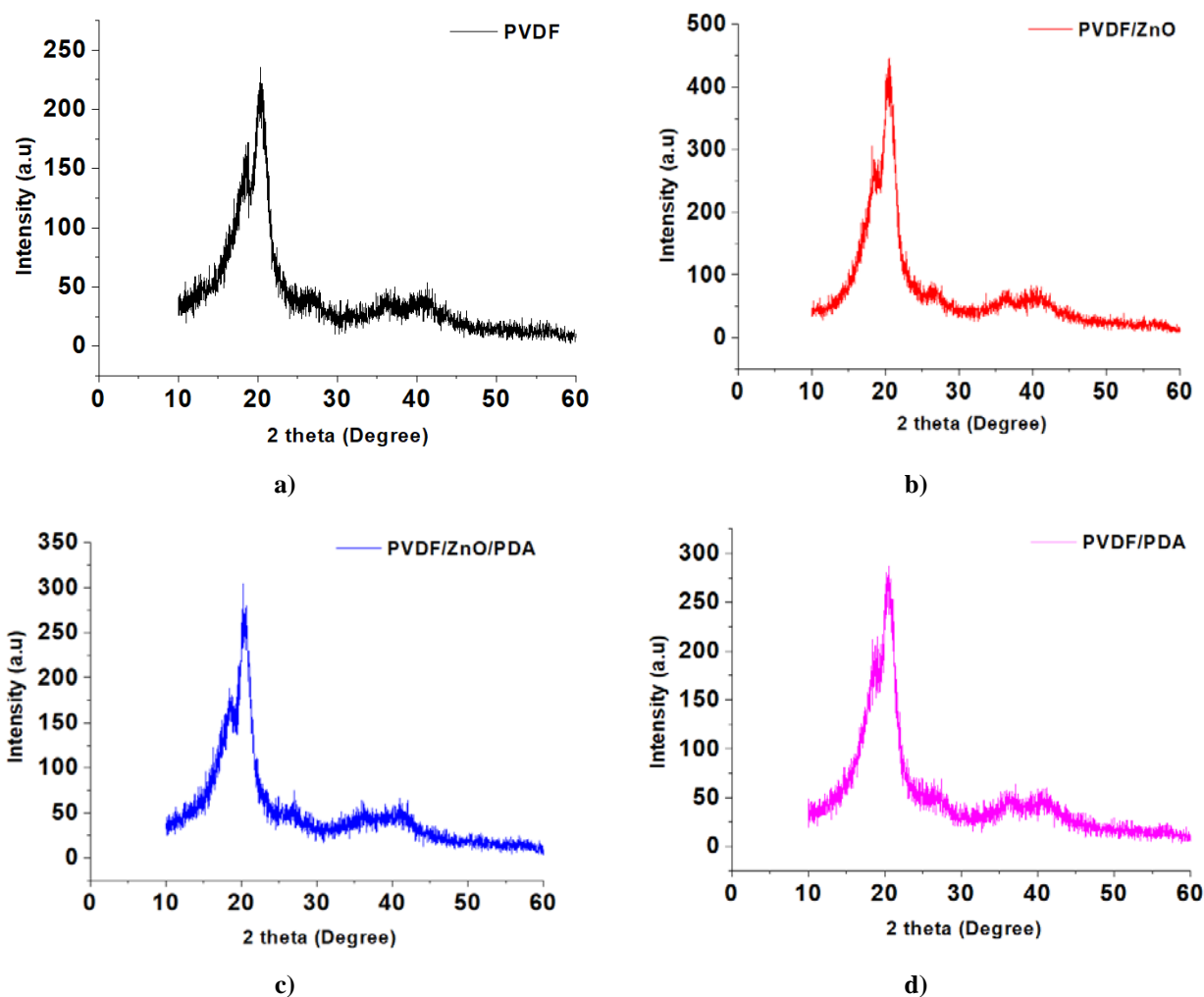


**Figure 5.** XRD patterns of membranes a) PVDF b) PVDF/ZnO c) PVDF/ZnO/PDA d) PVDF/PDA.

Functional groups of all membranes determined by FTIR analysis are given in Figure 6. The spectra of PVDF/ZnO and PVDF/ZnO/PDA nanocomposite membranes are quite similar. The wide peaks between 3500  $\text{cm}^{-1}$  and 2950  $\text{cm}^{-1}$  could correspond to the stretching vibrations of the N-H and hydroxyl groups resulting from catechol, which is the main functional group of PDA. The bands at 3500  $\text{cm}^{-1}$  were assigned to the O-H group of adsorbed water [38]. In addition, new clear peaks at 1500-1700  $\text{cm}^{-1}$  in the spectra of PVDF/PDA/ZnO and PVDF/PDA membranes were attributed to the

superposition of phenylic C-C stretching vibrations, N-H bending vibrations, and N-H shearing vibrations [49]. The FTIR spectra of the membranes show vibrational peaks at about 840 and 700  $\text{cm}^{-1}$ , which are typical vibrational characteristics of the  $\beta$ -crystal phase [50]. The bands at 1177, 977, 840, and 509  $\text{cm}^{-1}$  are able to be assigned to the vibration of the  $\beta$ -PVDF polymorphic phase [51]. It was observed that the intensity of the bands at 1177 and 840  $\text{cm}^{-1}$  increased after the addition of ZnO nanoparticles which indicated that ZnO nanoparticles enhanced the crystallization of the  $\beta$ -PVDF phase. In addition, the strong absorption band at 1177  $\text{cm}^{-1}$  is able to associate with the stretching vibration of  $-\text{CF}_2$  [51].

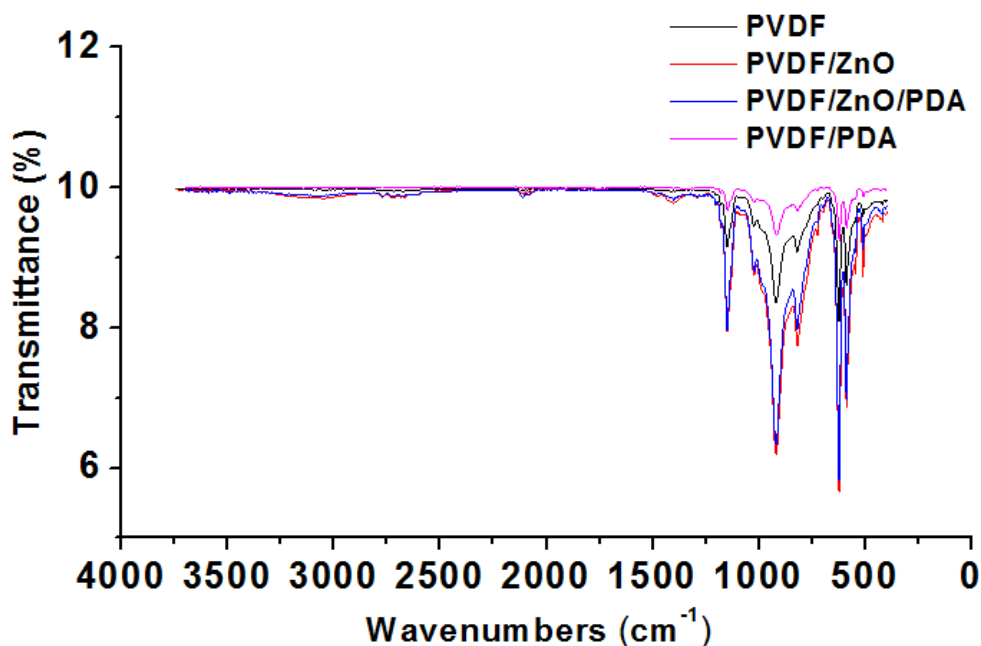
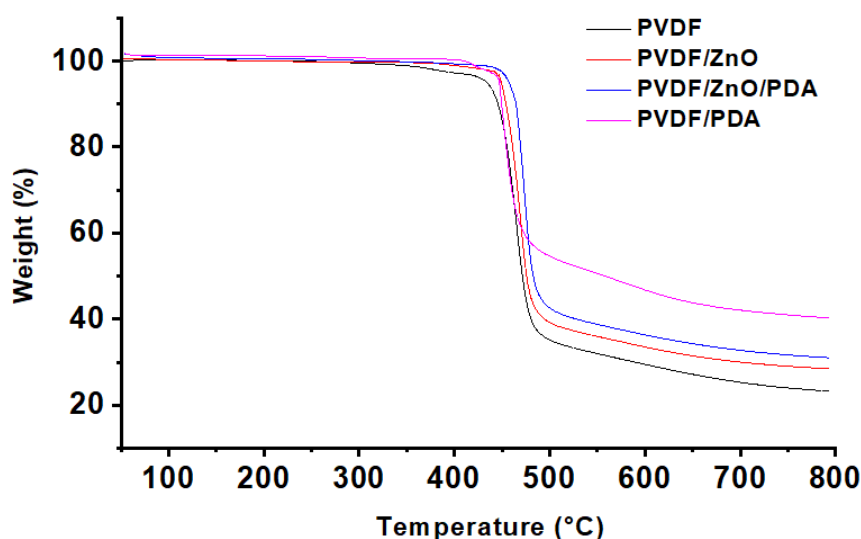


Figure 6. FTIR spectra of the pristine PVDF and modified nanocomposite membranes.

The thermal properties of the fabricated membranes investigated using TGA analysis are given in Figure 7. The degradation of the pristine membrane occurred between 430-500°C with a mass loss of 65%. Decomposition temperatures of ZnO-doped and the PDA-coated composite membranes were similar to that of the pristine PVDF membrane, which was probably due to the fact that neither the ZnO nanoparticles and nor the PDA layer could not be distributed homogeneously in the polymer matrix, as also supported by SEM analyses results. Decomposition of the PVDF/ZnO/PDA nanocomposite membrane was observed in the range of 470-510°C with a mass loss of 57%. This improvement in thermal stability of PVDF/ZnO/PDA membrane could be attributed to the strong interaction of ZnO/PDA powders with the polymer chains [21, 31].



**Figure 7.** TGA thermograms of the fabricated membranes.

Mechanical properties of the pristine PVDF and nanocomposite membranes were evaluated by Young's modulus (MPa), tensile strength (MPa), and elongation at break (%), and the results are presented in Table 3. The mechanical properties of porous membranes depend mainly on the characteristics of the polymer, fillers as well as porosity and pore size distribution of porous membranes. The Young's modulus, which is a measure of stiffness of a material, can be found from the slope of the stress-strain curve in the elastic region, which describes how much of the material tested deforms for different levels of applied stress. As shown in Table 3, the Young's modulus of the pristine PVDF membrane was 67.1 MPa and increased to 117.8 MPa and 98.9 MPa with the addition of ZnO and ZnO/PDA powders to the membrane matrix, respectively. A more rigid structure of both composite membranes could be attributed to the presence of nanofillers serving as a bridge between the polymer chains [52]. Tensile strength is the value of the maximum stress that a material can handle. The tensile strength of the PVDF/ZnO and PVDF/ZnO/PDA membranes had higher values in comparison to that of pristine PVDF membrane since more energy would be required to break the bonds between ZnO and PVDF and also between PDA/ZnO and PVDF due to the rigidity enhancement of polymer chains [18]. The elongation at the break is an indicator of the elasticity of a material. Elongation at break of the PVDF membrane increased from 14.5% to 19.0% with the addition of ZnO/PDA powders into the membrane matrix since PDA was able to absorb energy during the tensile test, thereby leading to a decrease in the fragility of the membranes [49, 53]. However, even though PVDF/ZnO membrane exhibited the highest Young's modulus and tensile strength values, significant amount of ZnO clusters observed on the PVDF/ZnO membrane surface (Figure 3b) led to weaker interactions of the nanoparticles with the polymer chains in some spots and resulted a decrease in the rupture elongation value of the membrane [54]. It is well known that nanoparticles can significantly resist the applied stress and improve the modulus on the condition that they are uniformly distributed along the matrix. Any defects resulted from aggregations can remarkably reduce the mechanical strength due to brittleness [55]. Although the mechanical properties are expected to be better for membranes with a smaller pore size, due to the non-uniform distribution of PDA fillers on the surface caused the formation of weak stress zones, which in turn resulted in the poor mechanical stability of the PVDF/PDA membrane [56]. However, when the PVDF/ZnO/PDA membrane is examined, it is seen that the mechanical properties of the membrane improve as an effect of the distribution of ZnO/PDA powders in the membrane matrix.

**Table 3.** Mechanical properties of the membranes.

Membrane ID	Young's modulus (MPa)	Tensile strength (MPa)	Elongation at break (%)
PVDF	67.1±1.85	1.89±0.35	14.5±2.88
PVDF/ZnO	117.8±4.02	2.23±0.49	10.4±0.57
PVDF/ZnO/PDA	98.9±3.05	2.15±0.43	19.0±2.00
PVDF/PDA	61.9±2.87	1.69±0.05	12.0±1.50

### 3.3. Separation Performance of Membranes

The separation performance of the fabricated membranes was determined in terms of water flux, rejection, and anti-fouling properties. At least three measurements were made to for each performance indicator and the average of these values were reported.

Water flux and SA rejections of the fabricated membranes are shown in Figure 8. According to Figure 8, water flux values of pristine PVDF, PVDF/ZnO, PVDF/ZnO/PDA, and PVDF/PDA membranes were determined as 45 L/m<sup>2</sup>h, 46 L/m<sup>2</sup>h, 49 L/m<sup>2</sup>h, and 32 L/m<sup>2</sup>h, respectively. This result showed that modification of PVDF matrix with nanoparticles resulted in no significant change

in water flux, whereas surface coating caused a reduction in the flux. This was supported by observing a significant amount of ZnO and PDA clusters on the surface of the PVDF/ZnO (Fig. 3b) and PVDF/PDA (Fig. 3d) membrane in the SEM analysis, respectively, and the porosity results.

The SA removal of pristine PVDF membrane increased from 93% to 95% and 97%, with the addition of ZnO and ZnO/PDA fillers to the membrane matrix, respectively, which was attributed to the improved hydrophilicity of the matrix. The increase in hydrophilicity with the addition of fillers reduced the interaction between SA and the membrane surface, preventing the penetration of contaminant molecules through modified membranes during SA filtration [57, 58].

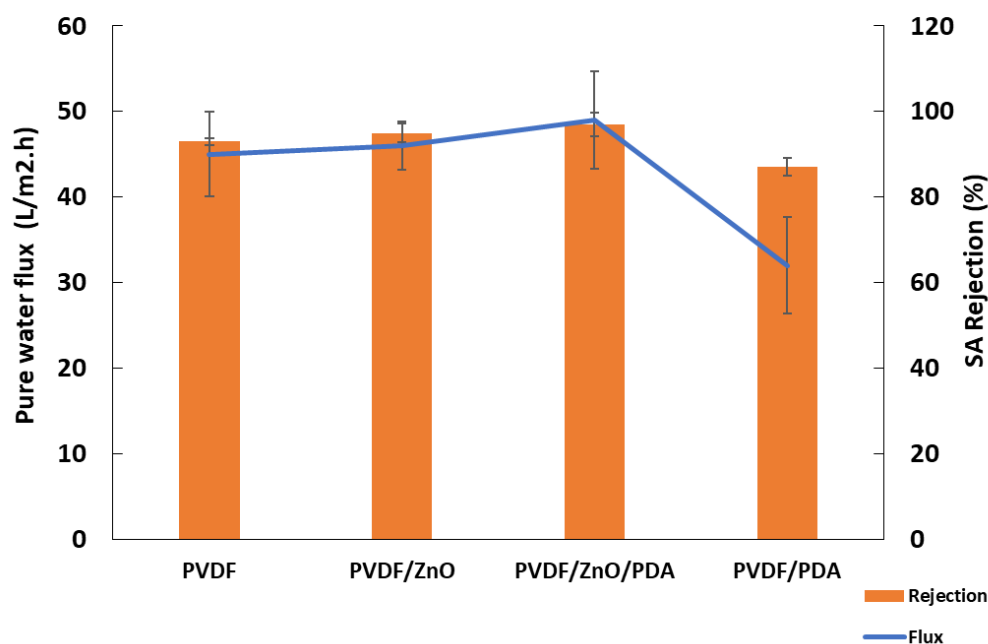


**Figure 8.** Water flux and SA rejections of the fabricated membranes.

The compaction behavior of the nanocomposite membranes in comparison to that of pristine PVDF membranes were investigated by measuring the water flux values at varying transmembrane pressures. As seen in Figure 9, water flux of all fabricated membranes increased with the applied transmembrane pressure. Even though the water flux of PVDF, PVDF/ZnO, and PVDF/ZnO/PDA membranes increased linearly with TMP until 0.15 MPa and 0.20 MPa, respectively, deviations from linearity were observed for all three membranes due to the pore deformation. However, the water flux values of the PVDF/ZnO/PDA membrane remained linear until the highest applied pressure, which revealed that with the addition of ZnO/PDA powders to the membrane matrix, the pore integrity was maintained even at high transmembrane pressures as a result of improvement in mechanical properties. The results agree well the mechanical properties given in Table 3.

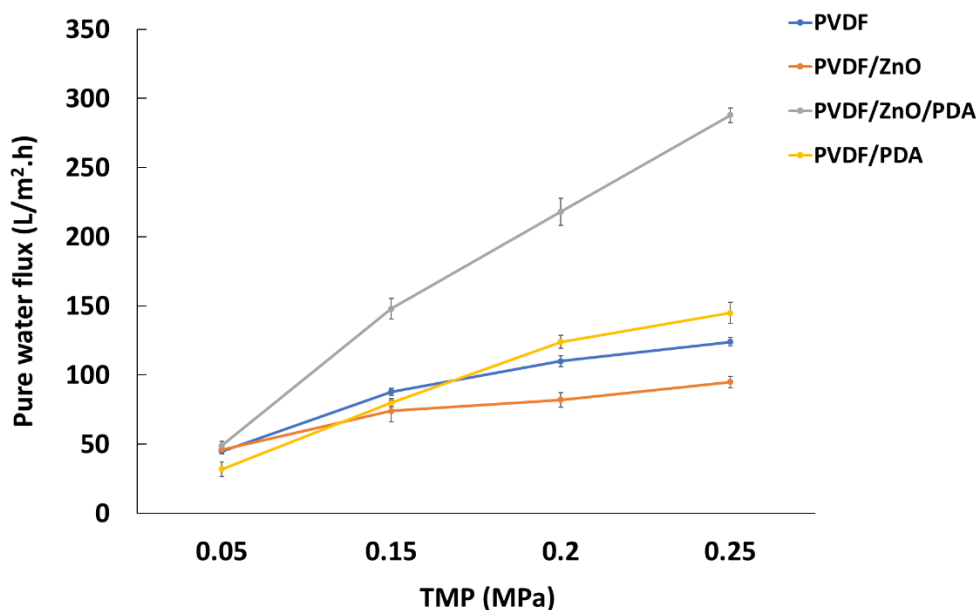


**Figure 9.** Variation of water flux with transmembrane pressure.

The anti-fouling properties of the fabricated membranes determined in terms of FRR and resistance values are shown in Figures 10 and 11, respectively. The FRR of the pristine PVDF membrane was as low as 51% due to the extremely hydrophobic nature of PVDF. Modification of membrane matrix with ZnO, PVDF/ZnO, and PDA provided an increase in FRR values to 57%, 92%, and 70%, respectively. The negatively charged groups (-OH) in ZnO/PDA nanoparticles repel the negative ions in the SA foulant solution mitigating the adsorption of the particles onto the membrane surface and internal pores, and therefore the anti-fouling properties were enhanced markedly [59]. In addition, the hydration layer induced on the membrane surface due to the presence of hydrophilic fillers would inhibit SA molecules from attaching to the membrane surface [60]. The FRR value of the PVDF/PDA membrane was not as high as PVDF/ZnO/PDA membrane due to the uneven distribution of PDA fillers in the matrix.

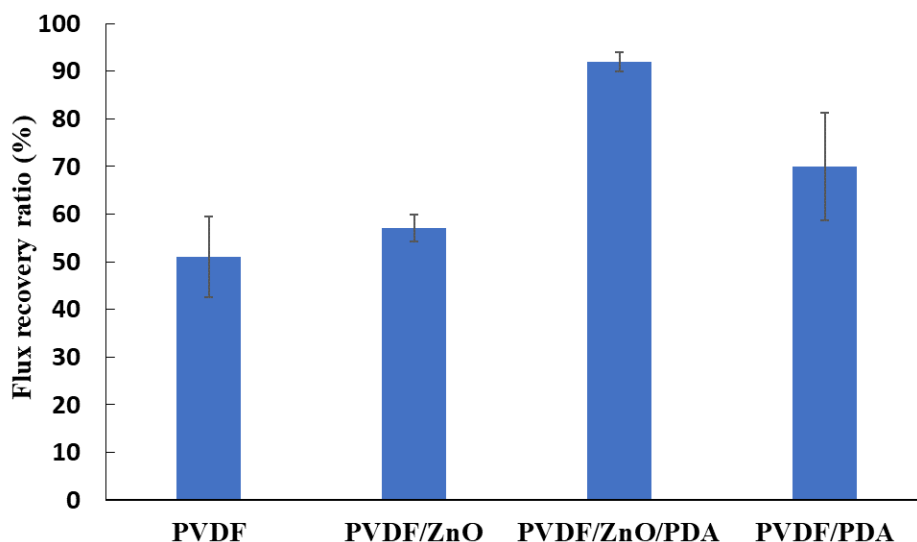


**Figure 10.** FRR values of the fabricated membranes after SA fouling.

According to Figure 11, the total fouling resistance of the ZnO/PDA membrane decreased compared to that of the pure PVDF membrane. The irreversible resistance of the pristine PVDF membrane ( $12.75 \times 10^8 \text{ m}^{-1}$ ) decreased to  $10.05 \times 10^8 \text{ m}^{-1}$  and  $0.70 \times 10^8 \text{ m}^{-1}$  with the addition of ZnO and ZnO/PDA fillers into the matrix, respectively. This result confirmed that the improvement of



membrane hydrophilicity with the addition of ZnO/PDA powders reduced the interaction between SA and membrane surface, which in turn avoided the permanent fouling [57, 58]. Non-uniform distribution of PDA coating layer on the surface led to a comparatively higher internal membrane resistance with regards to pristine PVDF membrane and yet no significant improvement was demonstrated in reversible and irreversible resistances.

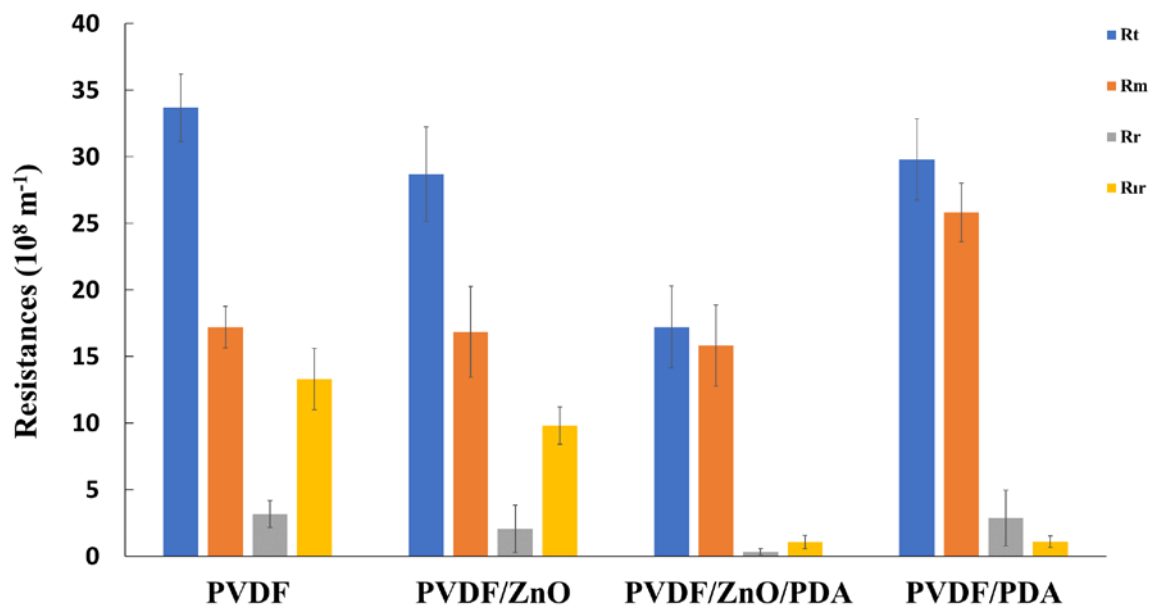


Figure 11. Filtration resistances of the fabricated membranes during SA fouling.

### 3.4. Lead Removal Efficiency

Since the pore sizes of the ultrafiltration membranes were not appropriate to separate Pb<sup>2+</sup> ions with high efficiency, chitosan as the chelating agent was used for binding the metal to form macromolecular complexes (Figure 1). The lead-chitosan removal efficiencies of the fabricated membranes were investigated for a constant Pb<sup>2+</sup> concentration of 10 ppm and pH value of 9.0 for different lead/chitosan ratios of 1:50 and 1:100 by mass. The results are given in Figure 12.

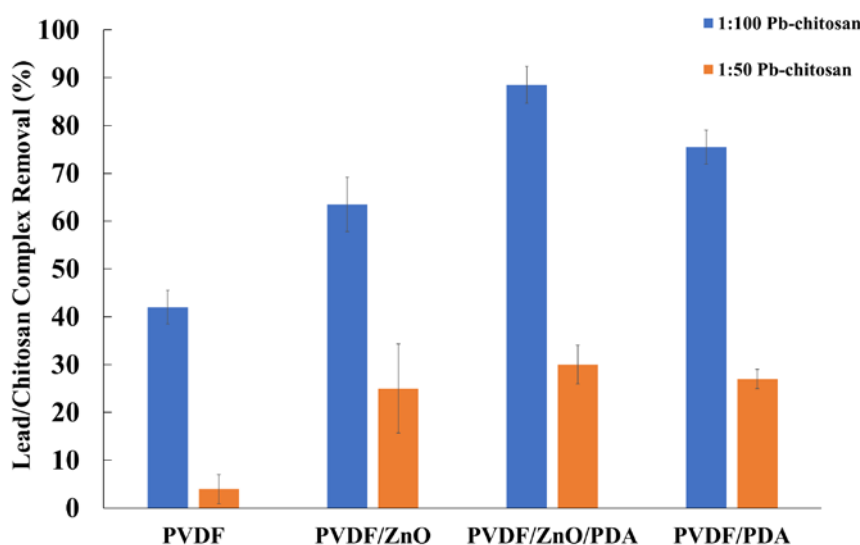


Figure 12. Lead-chitosan complex removal performance of membranes at different Pb/chitosan ratios (pH:9).

Chitosan, which is a cationic polyelectrolyte, is soluble in aqueous acidic media, and chelates metal ions. The formation of the metal-chitosan complex occurs primarily through the amino groups of chitosan, which act as ligands [61]. The interaction of metal ions with -OH and -NH<sub>2</sub> connects one or more chitosan chains. The complex structure formed has a larger diameter than the membrane pores allowing the Pb<sup>+2</sup> ions to be retained by the membrane [62, 63]. The main parameters affecting on complexation of target metal with polymer are metal and polymer type, loading (the ratio of metal to polymer), pH, and existence of other metal ions in the solution [63]. As seen in Figure 12, lead-chitosan complex removal efficiency of pristine PVDF membrane increased as a result of the addition of different fillers into the pristine membrane matrix. Moreover, doubling the concentration of chitosan led to a marked increase in the lead-chitosan removal efficiency from aqueous solutions in the case of all fabricated membranes. The lead-chitosan complex removal performances of pristine PVDF, PVDF/ZnO, PVDF/ZnO/PDA, and PVDF/PDA membranes were determined as 42%, 63.5%, 88.5%, and 75.5%, respectively for a lead-chitosan ratio of 1:100. Among the fabricated membranes, PVDF/ZnO/PDA membrane exhibited the highest lead-chitosan complex removal efficiency, which was probably due to the combined effects of uniform dispersion of ZnO/PDA nanoparticles in the membrane matrix, especially on the surface and relatively small pore size distribution of the PVDF/ZnO/PDA membrane.

#### 4. Conclusions

In the present study, PVDF-based nanocomposite flat-sheet membranes were developed by adding certain amounts of ZnO and ZnO/PDA powders to the membrane matrix and coating the membrane surface with PDA. The separation performance of the membranes were investigated in terms of water flux, sodium alginate (SA) rejection, and antifouling properties in comparison to pristine PVDF membrane. Moreover, lead removal efficiencies of the membranes from aqueous solutions with polymer-enhanced ultrafiltration method was investigated using chitosan as a chelating agent. The SEM images exhibited remarkable changes in pristine PVDF membrane morphology with higher connectivity among channels due to the presence of ZnO/PDA powders, indicating a uniform dispersion of the fillers as well as strong interaction with the polymer chains. As a result, bulk properties such as thermal stability and mechanical strength were enhanced substantially. Even though there was no significant improvement in water permeability of the pristine membrane, SA rejection increased from 93% to 97%, and a marked enhancement of 80% was obtained for FRR value with the addition of 0.5% ZnO/PDA fillers into the membrane matrix. Moreover, PVDF/ZnO/PDA membrane provided the highest lead-chitosan complex removal efficiency of 88.5% from aqueous solutions for a Pb-chitosan ratio of 1:100, which was probably due to the combined effects of uniform ZnO/PDA dispersion in the matrix, and comparatively smaller pore size distribution of the membrane structure.

**Peer-review:** Externally peer - reviewed.

**Conflict of Interest:** No conflict of interest was declared by the authors. This paper has been presented at the ICENTE'21 (International Conference on Engineering Technologies) held in Konya (Turkey), November 18-20, 2021.

**Financial Disclosure:** The authors declared that this study has received no financial support.

#### References

- [1] Hosseini, S. M., Alibakhshi, H., Jashni, E., Parvizian, F., Shen, J. N., Taheri, M., & Rafiei, N. (2020). A novel layer-by-layer heterogeneous cation Exchange membrane for heavy metal ions removal from water. *Journal of hazardous materials*, 381, 120884.

- [2] Naz, S., Rasheed, T., Naqvi, S. T. R., Hussain, D., Fatima, B., ul Haq, M. N., & Ibrahim, M. (2020). Polyvinylpyrrolidone decorated manganese ferrite-based cues for the efficient removal of heavy metals ions from wastewater. *Physica B: Condensed Matter*, 599, 412559.
- [3] Zhou, Q., Yang, N., Li, Y., Ren, B., Ding, X., Bian, H., & Yao, X. (2020). Total concentrations and sources of heavy metal pollution in the global river and lake water bodies from 1972 to 2017. *Global Ecology and Conservation*, 22, e00925.
- [4] Zhou, D., Zhu, L., Fu, Y., Zhu, M., & Xue, L. (2015). Development of lower-cost seawater desalination processes using nanofiltration technologies. *Desalination*, 376, 109- 116.
- [5] Fasaee, M. A. K., Berglund, E., Pieper, K. J., Ling, E., Benham, B., & Edwards, M. (2021). Developing a framework for classifying water lead levels at private drinking water systems: A Bayesian Belief Network approach. *Water Research*, 189, 116641.
- [6] Fang, X., Li, J., Li, X., Pan, S., Zhang, X., Sun, X., ... & Wang, L. (2017). Internal pore decoration with polydopamine nanoparticle on polymeric ultrafiltration membrane for enhanced heavy metal removal. *Chemical Engineering Journal*, 314, 38-49.
- [7] Hajdu, I., Bodnár, M., Csikós, Z., Wei, S., Daróczy, L., Kovács, B., ... & Borbély, J. (2012). Combined nano-membrane technology for removal of lead ions. *Journal of Membrane Science*, 409, 44-53.
- [8] Sheng, P. X., Ting, Y. P., Chen, J. P., & Hong, L. (2004). Sorption of lead, copper, cadmium, zinc, and nickel by marine algal biomass: characterization of biosorptive capacity and investigation of mechanisms. *Journal of colloid and interface science*, 275(1), 131-141.
- [9] He, J., Xiong, D., Zhou, P., Xiao, X., Ni, F., Deng, S., & Luo, L. (2020). A novel homogenous in-situ generated ferrihydrite nanoparticles/polyethersulfone composite membrane for removal of lead from water: Development, characterization, performance, and mechanism. *Chemical Engineering Journal*, 393, 124696.
- [10] Wang, K., Abdalla, A. A., Khaleel, M. A., Hilal, N. Khraisheh, M. K. (2017). Mechanical Properties of Water Desalination and Wastewater Treatment Membranes. *Desalination*. 401, 190-205.
- [11] Xu, W., Sun, X., Huang, M., Pan, X., Huang, X., & Zhuang, H. (2020). Novel covalent organic framework/PVDF ultrafiltration membranes with antifouling and lead removal performance. *Journal of Environmental Management*, 269, 110758.
- [12] Ali, H., & Khan, E. (2019). Bioaccumulation of Cr, Ni, Cd, and Pb in the economically important freshwater fish *Schizothorax plagiostomus* from three rivers of Malakand Division, Pakistan: risk assessment for human health. *Bulletin of environmental contamination and toxicology*, 102(1), 77-83.
- [13] Mulder, M., & Mulder, J. (1996). *Basic principles of membrane technology*. Springer Science & Business Media.
- [14] Aslan, M. (2016). Membran Teknolojileri. *T.C. Çevre ve Şehircilik Bakanlığı*. 57-218.
- [15] Gebru, K. A., & Das, C. (2018). Removal of chromium (VI) ions from aqueous solutions using amine impregnated TiO<sub>2</sub> nanoparticles modified cellulose acetate membranes. *Chemosphere*, 191, 673-684.
- [16] Ursino, C., Castro-Muñoz, R., Drioli, E., Gzara, L., Albeirutty, M. H., & Figoli, A. (2018). Progress of nanocomposite membranes for water treatment. *Membranes*, 8(2), 18.
- [17] Bai, H., Wang, X., Zhou, Y., & Zhang, L. (2012). Preparation and characterization of poly (vinylidene fluoride) composite membranes blended with nano-crystalline cellulose. *Progress in Natural Science: Materials International*, 22(3), 250-257.

- [18] Hong, J., & He, Y. (2012). Effects of nano-sized zinc oxide on the performance of PVDF microfiltration membranes. *Desalination*, 302, 71-79.
- [19] Shi, H., He, Y., Pan, Y., Di, H., Zeng, G., Zhang, L., & Zhang, C. (2016). A modified mussel-inspired method to fabricate TiO<sub>2</sub> decorated superhydrophobic PVDF membrane for oil/water separation. *Journal of Membrane Science*, 506, 60-70.
- [20] Zhang, Q., Cui, Z., & Li, W. (2020). High permeability poly (vinylidene fluoride) ultrafiltration membrane doped with polydopamine modified TiO<sub>2</sub> nanoparticles. *Chinese Journal of Chemical Engineering*, 28(12), 3152-3158.
- [21] Liebscher, J. (2019). Chemistry of polydopamine—scope, variation, and limitation. *European Journal of Organic Chemistry*, 2019(31-32), 4976-4994.
- [22] Tavakoli, S., Kharaziha, M., & Nemati, S. (2021). Polydopamine coated ZnO rod-shaped nanoparticles with noticeable biocompatibility, hemostatic and antibacterial activity. *Nanostructures & Nano-Objects*, 25, 100639.
- [23] Trivunac, K., & Stevanovic, S. (2006). Removal of heavy metal ions from water by complexation-assisted ultrafiltration. *Chemosphere*, 64(3), 486-491.
- [24] Juang, R. S., & Shiau, R. C. (2000). Metal removal from aqueous solutions using chitosan-enhanced membrane filtration. *Journal of membrane science*, 165(2), 159-167.
- [25] Petrov, S., & Nenov, V. (2004). Removal and recovery of copper from wastewater by a complexation-ultrafiltration process. *Desalination*, 162, 201-209.
- [26] Müslehiddinoğlu, J., Uludağ, Y., Özbelge, H. Ö., & Yilmaz, L. (1998). Effect of operating parameters on selective separation of heavy metals from binary mixtures via polymer enhanced ultrafiltration. *Journal of Membrane Science*, 140(2), 251-266.
- [27] Vieira, M., Tavares, C. R., Bergamasco, R., & Petrus, J. C. C. (2001). Application of ultrafiltration-complexation process for metal removal from pulp and paper industry wastewater. *Journal of Membrane Science*, 194(2), 273-276.
- [28] Zhang, Y. F., & Xu, Z. L. (2003). Study on the treatment of industrial wastewater containing Pb<sup>2+</sup> ion using a coupling process of polymer complexation-ultrafiltration. *Separation Science and Technology*, 38(7), 1585-1596.
- [29] Llorens, J., Pujola, M., & Sabaté, J. (2004). Separation of cadmium from aqueous streams by polymer enhanced ultrafiltration: a two-phase model for complexation binding. *Journal of Membrane Science*, 239(2), 173-181.
- [30] Freire, E., Bianchi, O., Monteiro, E. E., Nunes, R. C. R., & Forte, M. C. (2009). Processability of PVDF/PMMA blends studied by torque rheometry. *Materials Science and Engineering: C*, 29(2), 657-661.
- [31] Ma, F. F., Zhang, N., Wei, X., Yang, J. H., Wang, Y., & Zhou, Z. W. (2017). Blend-electrospun poly (vinylidene fluoride)/polydopamine membranes: self-polymerization of dopamine and the excellent adsorption/separation abilities. *Journal of Materials Chemistry A*, 5(27), 14430-14443.
- [32] Gu, X., Zhang, Y., Sun, H., Song, X., Fu, C., & Dong, P. (2015). Mussel-inspired polydopamine coated iron oxide nanoparticles for biomedical application. *Journal of Nanomaterials*, Article ID 154592.
- [33] Demirel, E., Zhang, B., Papakyriakou, M., Xia, S., & Chen, Y. (2017). Fe<sub>2</sub>O<sub>3</sub> nanocomposite PVC membrane with enhanced properties and separation performance. *Journal of membrane science*, 529, 170-184.

- [34] Wu, G., Gan, S., Cui, L., & Xu, Y. (2008). Preparation and characterization of PES/TiO<sub>2</sub> composite membranes. *Applied Surface Science*, 254(21), 7080-7086.
- [35] Vatanpour, V., Madaeni, S. S., Moradian, R., Zinadini, S., & Astinchap, B. (2012). Novel antifouling nanofiltration polyethersulfone membrane fabricated from embedding TiO<sub>2</sub> coated multiwalled carbon nanotubes. *Separation and purification technology*, 90, 69-82.
- [36] Mahmoudi, C., Demirel, E., & Chen, Y. (2020). Investigation of characteristics and performance of polyvinyl chloride ultrafiltration membranes modified with silica-oriented multi-walled carbon nanotubes. *Journal of Applied Polymer Science*, 137(45), 49397.
- [37] Juang, R. S., & Chiou, C. H. (2000). Ultrafiltration rejection of dissolved ions using various weakly basic water-soluble polymers. *Journal of Membrane Science*, 177(1-2), 207-214.
- [38] Zhang, X., Wang, Y., Liu, Y., Xu, J., Han, Y., & Xu, X. (2014). Preparation, performances of PVDF/ZnO hybrid membranes and their applications in the removal of copper ions. *Applied Surface Science*, 316, 333-340.
- [39] Fedorenko, V., Viter, R., Mrówczyński, R., Damberga, D., Coy, E., & Iatsunskyi, I. (2020). Synthesis and photoluminescence properties of hybrid 1D core-shell structured nanocomposites based on ZnO/polydopamine. *RSC Advances*, 10(50), 29751-29758.
- [40] Muhammad, W., Ullah, N., Haroon, M., & Abbasi, B. H. (2019). Optical, morphological, and biological analysis of zinc oxide nanoparticles (ZnO NPs) using *Papaver somniferum* L. *RSC Advances*, 9(51), 29541-29548.
- [41] Meng, R., Chen, Y., Zhang, X., Dong, X., Ma, H., & Wang, G. (2017). Synthesis of a hydrophilic  $\alpha$ -sulfur/PDA composite as a metal-free photocatalyst with enhanced photocatalytic performance under visible light. *Journal of Macromolecular Science-Pure and Applied Chemistry*, 54(5), 334-338.
- [42] Popa, A., Toloman, D., Stan, M., Stefan, M., Radu, T., Vlad, G., & Pana, O. (2021). Tailoring the RhB removal rate by modifying the PVDF membrane surface through ZnO particles deposition. *Journal of Inorganic and Organometallic Polymers and Materials*, 31(4), 1642-1652.
- [43] Syawaliah, S., Arahman, N., Riza, M., & Mulyati, S. (2018). The influences of polydopamine immersion time on characteristics and performance of polyvinylidene fluoride ultrafiltration membrane. In *MATEC Web of Conferences* (Vol. 197, p. 09007). EDP Sciences.
- [44] Guclu, S., Erkoc-Ilter, S., Koseoglu-Imer, D. Y., Unal, S., Menciloglu, Y. Z., Ozturk, I., & Koyuncu, I. (2019). Interfacially polymerized thin-film composite membranes: Impact of support layer pore size on active layer polymerization and seawater desalination performance. *Separation and Purification Technology*, 212, 438-448.
- [45] Muchtar, S., Wahab, M. Y., Fang, L. F., Jeon, S., Rajabzadeh, S., Takagi, R., & Matsuyama, H. (2019). Polydopamine-coated poly(vinylidene fluoride) membranes with high ultraviolet resistance and antifouling properties for a photocatalytic membrane reactor. *Journal of Applied Polymer Science*, 136(14), 47312.
- [46] Li, N., Tian, Y., Zhang, J., Sun, Z., Zhao, J., Zhang, J., & Zuo, W. (2017). Precisely controlled modification of PVDF membranes with 3D TiO<sub>2</sub>/ZnO nanolayer: enhanced anti-fouling performance by changing hydrophilicity and photocatalysis under visible light irradiation. *Journal of Membrane Science*, 528, 359-368.
- [47] Meng, R., Chen, Y., Zhang, X., Dong, X., Ma, H., & Wang, G. (2017). Synthesis of a hydrophilic  $\alpha$ -sulfur/PDA composite as a metal-free photocatalyst with enhanced



- photocatalytic performance under visible light. *Journal of Macromolecular Science, Part A*, 54(5), 334-338.
- [48] Moazeni, N., Sadrjahani, M., Merati, A. A., Latifi, M., & Rouhani, S. (2019). Effect of stimuli-responsive polydiacetylene on the crystallization and mechanical properties of PVDF nanofibers. *Polymer Bulletin*, 77(17) 1-16.
- [49] Li, J. H., Ni, X. X., Zhang, D. B., Zheng, H., Wang, J. B., & Zhang, Q. Q. (2018). Engineering self-driven PVDF/PDA hybrid membranes based on membrane micro-reactor effect to achieve super-hydrophilicity, excellent antifouling properties, and hemocompatibility. *Applied Surface Science*, 444, 672-690.
- [50] Sorayani Bafqi, M. S., Bagherzadeh, R., & Latifi, M. (2015). Fabrication of composite PVDF-ZnO nanofiber mats by electrospinning for energy scavenging application with enhanced efficiency. *Journal of polymer research*, 22(7), 1-9.
- [51] Radwan, A. B., Mohamed, A. M., Abdullah, A. M., & Al-Maadeed, M. A. (2016). Corrosion protection of electrospun PVDF-ZnO superhydrophobic coating. *Surface and Coatings Technology*, 289, 136-143.
- [52] Spasova, M., Manolova, N., Markova, N., & Rashkov, I. (2017). Tuning the properties of PVDF or PVDF-HFP fibrous materials decorated with ZnO nanoparticles by applying electrospinning alone or in conjunction with electrospraying. *Fibers and Polymers*, 18(4), 649-657.
- [53] Jiang, J. H., Zhu, L. P., Zhang, H. T., Zhu, B. K., & Xu, Y. Y. (2014). Improved hydrodynamic permeability and antifouling properties of poly (vinylidene fluoride) membranes using polydopamine nanoparticles as additives. *Journal of Membrane Science*, 457, 73-81.
- [54] Yan, L., Li, Y. S., Xiang, C. B., & Xianda, S. (2006). Effect of nano-sized Al<sub>2</sub>O<sub>3</sub>-particle addition on PVDF ultrafiltration membrane performance. *Journal of Membrane Science*, 276(1-2), 162-167.
- [55] Wan, Y., Wu, Q., Wang, S., Zhang, S., & Hu, Z. (2007). Mechanical properties of porous polylactide/chitosan blend membranes. *Macromolecular Materials and Engineering*, 292, 598-607.
- [56] Manawi, Y. M., Wang, K., Kochkodan, V., Johnson, D. J., Atieh, M. A., & Khraisheh, M. K. (2018). Engineering the surface and mechanical properties of water desalination membranes using ultralong carbon nanotubes. *Membranes*, 8(4), 106.
- [57] Breite, D., Went, M., Prager, A., & Schulze, A. (2015). Tailoring membrane surface charges: A novel study on electrostatic interactions during membrane fouling. *Polymers*, 7(10), 2017-2030.
- [58] Rana, D., & Matsuura, T. (2010). Surface modifications for antifouling membranes. *Chemical Reviews*, 110(4), 2448-2471.
- [59] Lalia, B. S., Kochkodan, V., Hashaikeh, R., & Hilal, N. (2013). A review on membrane fabrication: Structure, properties, and performance relationship. *Desalination*, 326, 77-95.
- [60] Kumar, R., & Ismail, A. F. (2015). Fouling control on microfiltration/ultrafiltration membranes: Effects of morphology, hydrophilicity, and charge. *Journal of Applied Polymer Science*, 132(21), 42042.
- [61] Krajewska, B. (2001). Diffusion of metal ions through gel chitosan membranes. *Reactive and Functional Polymers*, 47(1), 37-47.

- [62] Wang, X., Du, Y., Fan, L., Liu, H., & Hu, Y. (2005). Chitosan-metal complexes as antimicrobial agent: synthesis, characterization, and structure-activity study. *Polymer Bulletin*, 55(1), 105-113.
- [63] Garba, M. D., Usman, M., Mazumder, M. A. J., & Al-Ahmed, A. (2019). Complexing agents for metal removal using ultrafiltration membranes: *Environmental Chemistry Letters*, 1-14.

# Synthesis and Photophysical Properties of Pyrene-BODIPY Functionalized Subphthalocyanine Dyad

\*<sup>1</sup> Seda Çetindere 

<sup>1</sup> Gebze Technical University Department of Chemistry, Turkey.

\* Corresponding author, e-mail: sdemirer@gtu.edu.tr

Submission Date: 04.01.2022

Acceptation Date: 21.03.2022

**Abstract** - The treatment of boron (III) subphthalocyanine chloride (SubPcCl) with borondipyrromethene (BODIPY) derivative consisting of one pyrene group in toluene gave the corresponding axially substituted boron (III) subphthalocyanine dyad (SubPcBodiPy). Novel compound has been fully characterized by FTIR, mass, NMR (<sup>1</sup>H and <sup>13</sup>C) spectroscopy and elemental analysis. Photophysical properties of SubPcBodiPy was investigated and compared with its precursors by fluorescence and absorption spectroscopy in tetrahydrofuran (THF). Accordingly, fluorescence lifetimes were measured directly by single exponential calculation.

**Keywords:** Subphthalocyanine, BODIPY, pyrene, photophysical properties

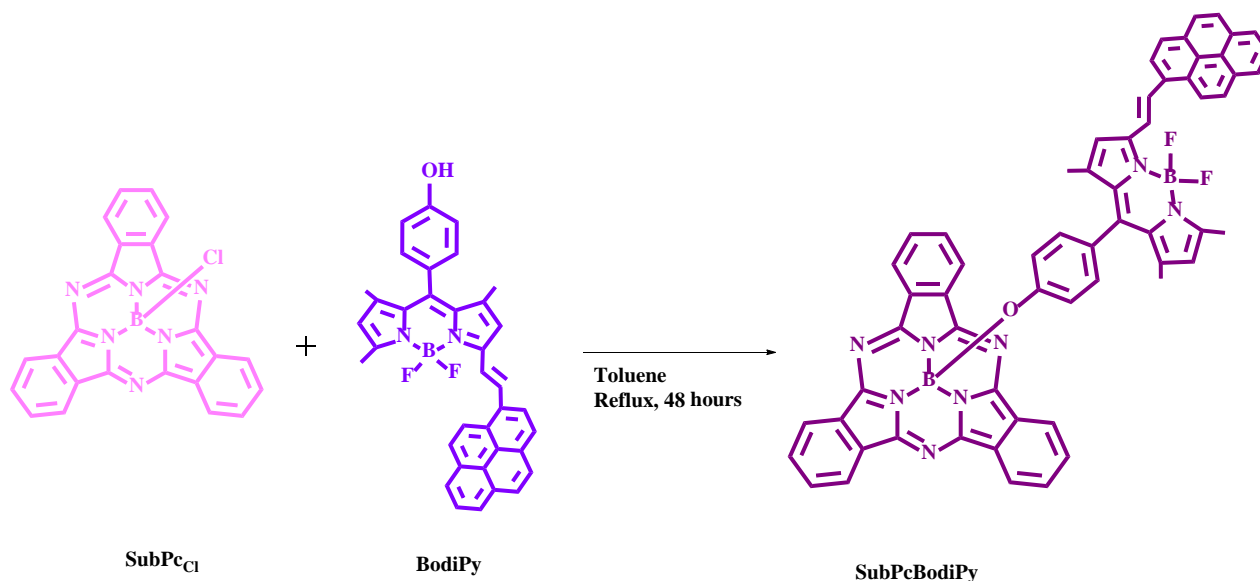
## 1. Introduction

Supramolecular systems with two or more chromophores are scientifically important for highly important applications ranging between optoelectronic devices, light harvesting and sensors. [1-2]. It is important to examine the photophysical properties of these compounds in detail. This indicates their dependence on functional dye systems [3]. BODIPY dyes are a very important material unit fluorophore family that has been widely studied due to its important specifications such as long excited state lifetimes, high fluorescent quantum yields, high absorption coefficients and generally good solubility in organic solvents. [4]. In addition, boron (III) subphthalocyanine (SubPc) derivatives are of great interest to the scientific world due to their specific and dish-like structures and physicochemical features like strong fluorescence and nonlinear optical features resulting from the aromatic conjugation system with delocalized  $14\pi$  electrons. [5]. SubPc derivatives are used as functional materials in different applications such as chemical sensors, organic thin-film transistors (OTFTs), organic photovoltaics (OPVs), organic light-emitting diodes (OLEDs), and supramolecular building blocks for molecular can be used [6-9]. The integration of BODIPY and SubPc on one molecule is expected to produce new photoactive materials. There are a few study on combination of SubPc-BODIPY derivatives reported in the literature. To the best of our knowledge, the first reported SubPc BODIPY derivatives exhibited highly efficient energy transfer [10] and then two axially substituted SubPc-BODIPY derivatives which have potentials to use in photodynamic therapy (PDT) applications have reported from our research group [11]. In recent years a series of SubPc-BODIPY compounds containing carbazole moieties which have energy transfer potential in efficient light-harvesting systems were reported by Ecik et al. [12]. In another study SubPc-BODIPY conjugates based photodevices have reported as photodiodes in solar tracking systems [13] and a series of BODIPY-SubPc dyads as photosensitizers for PDT [14].

In this study, synthesis and characterization of SubPcBodiPy were reported (Scheme 1). The photophysical properties of this novel compound were examined by UV-visible absorption and fluorescence spectral studies in THF. This novel compound retain the unique photophysical properties of its precursor BODIPY that showing its promise as photosensitizer.

---

<sup>1</sup> Corresponding author: E-mail: sdemirer@gtu.edu.tr



**Scheme 1:** Synthesis pathway of SubPcBodiPy

## 2. Materials and Methods

### 2.1. Materials

All chemical reactions were performed under inert argon atmosphere. Silica gel plates (Kieselgel 60, 0.25mm thickness) with F254 indicator were purchased from Merck for performed to thin layer chromatography (TLC). For purification of compounds, silica gel (Merck, Kieselgel 60, 230–400 mesh) was used for stationary phase on column chromatography with the appropriate eluents. 4-hydroxybenzaldehyde, boron trifluoride diethyl ether complex ( $\text{BF}_3\text{OEt}_2$ ), piperidine, dichloromethane, tetrahydrofuran, chloroform-d ( $\text{CDCl}_3$ ), ethylacetate (EtOAc), n-hexane, triethylamine (TEA) and toluene were obtained from Merck. Trifluoroacetic acid (TFA), para-toluenesulfonic acid (p-TsOH), 2,3-dichloro-5,6-dicyano-p-benzoquinone (DDQ) and 2,4-dimethyl-1H-pyrrole were purchased from Sigma-Aldrich. 1,8,9-antracenetriol which was used for mass analyses was obtained from Fluka. Boron (III) subphthalocyanine chloride and pyrene-1-carboxaldehyde were obtained from Alfa-Aesar.

### 2.2. Equipment

Elemental analyses were performed using a Thermo Finnigan Flash 1112 Instrument. Infrared spectra were measured on a Perkin Elmer Spectrum 100 FT-IR spectrophotometer. Mass spectra were measured using a MALDI-MS (Bruker microflex LT MALDI-TOF MS). A Shimadzu 2001 UV spectrophotometer and a Varian Eclipse spectrofluorometer were used for UV-Vis and fluorescence experiments. Fluorescence emission spectra were taken at room temperature by a using 1 cm pathlength cuvettes. NMR spectra ( $^1\text{H}$ ,  $^{13}\text{C}$ ) were obtained in  $\text{CDCl}_3$  by a Varian 500 MHz spectrometer. Fluoro Hub-B Single Photon Counting Controller equipped Horiba-Jobin-Yvon-SPEX Fluorolog 3-2iHR was used for fluorescence lifetime measurements.

### 2.3. Synthesis

The starting BODIPY(BodiPy) compound was synthesized and purified according to literature procedures [11].

Phenol containing Bodipy compound (200 mg; 0.6 mmol, 1 eq) [10], pyrene-1-carboxaldehyde (135 mg, 0.6 mmol, 1 eq), p-TsOH (168 mg; 0.8 mmol, 1.3 eq) and piperidine (0.1 mL) were heated at boiling point of toluene (50 mL). The formed water throughout the reaction was moved away

azeotropically by heating all night long in a Dean-Stark apparatus. The reaction mixture was concentrated by using vacuum and then chromatographed on silica gel using EtOAc: n-hexane (1:2) solvent system as eluent. BodiPy was collected as purple solid in (183 mg, 54% yield) [10]. The Analysis of Elemental: Found: C 77.25, H 4.90, N 4.02%,  $C_{36}H_{27}BF_2N_2O$  (553.3) needs C 78.27, H 4.93, N 5.07%. FTIR (ATR,  $cm^{-1}$ ): 3309 (-OH), 3039 (Ar-CH), 2959–2890 (-CH), 1637 (-C=N-), 1367 (B-N str), 1322 (B-F). MALDI MS:  $m/z$  calc. 553.3; found: 553.0  $[M]^+$  and 553.0  $[M-F]^+$   $^1H$  NMR (in DMSO- $d_6$ ,  $\delta$ , ppm) 10.02 (s, 1H, -OH), 8.94–7.98 (m, 9H, pyrene-H), 7.10 (d, 1H,  $J=16.2$ , H-C=C-H), 6.90 (d, 1H,  $J=16.2$ , H-C=C-H), 6.32 (d, 2H,  $J=7.2$ , Ar-H), 6.10 (d, 2H,  $J=7.2$ , Ar-H), 5.22 (s, 2H, pyrrole-H), 1.67 (s, 3H, CH<sub>3</sub>), 1.57 (s, 3H, CH<sub>3</sub>), 1.48 (s, 3H, CH<sub>3</sub>).  $^{13}C$  NMR (125 MHz, CDCl<sub>3</sub>,  $\delta$ , ppm) 166.3, 153.2, 131.8, 131.7, 130.3, 128.6, 127.2, 123.3, 126.0, 125.9, 125.4, 125.3, 125.0, 124.9, 124.2, 124.1, 121.2, 120.5, 109.2, 94.5, 68.9, 17.0, 15.6, 15.4.

Argon gas was first applied to the 20 mL reaction flask and then toluene (15 mL) was added to the flask. SubPcCl (78 mg, 0.18 mmol, 2 eq) was placed in the flask and then BodiPy (50 mg, 0.09 mmol, 1 eq) was added. The reaction mixture was stirred under reflux for 48 hours. By checking the reaction mixture by thin layer chromatography (TLC), the reaction was complete when BodiPy was finished. The mixture was then cooled to room temperature and filtered. Toluene was returned to evaporate. The residue was chromatographed on a column of silica gel using n-hexane as the eluent until the pink band containing unreacted compound appeared. Then the solvent system was changed to n-hexane-ethyl acetate (2:1) to take the pink-purple band which is refer to the new compound. It was collected and evaporated in vacuo to remove the solvent. The Analysis of Elemental: Found: C 75.20, H 3.95, N 12.08%,  $C_{60}H_{38}B_2F_2N_8O$  (946.64) needs C 76.13, H 4.05, N 11.84%. FTIR (ATR,  $cm^{-1}$ ): 2924.5, 2850.6 (Al-CH), 1730.5 (-N=C-), 1650.4 (-C=C-), 1592.5, 1536.3 (Ar-CH), 1508.7 (B-N), 1383.4 (B-F), 1303.5 (-N-CH<sub>3</sub>), 1242.2 (-N-C-), 1115.5 (-C-O-), 1067.9 (-C-C-), 1017.8 (B-O) (Figure 1). MALDI MS:  $m/z$  calc. 946.64; found: 946.77  $[M]^+$  and 926.43  $[M-F]^+$  (Figure 2).  $^1H$  NMR (500 MHz, CDCl<sub>3</sub>)  $\delta$ : 9.08-8.96 (m, 6H, SubPc-H $\alpha$ ), 8.33-7.99 (m, 9H, Py-H), 8.08 (d,  $J=16.2$  Hz, 1H, -HC=CH-), 7.39-7.18 (m, 2H, ArH), 7.09-6.86 (m, 6H, SubPc-H $\beta$ ), 7.09-6.84 (m, 2H, ArH), 6.83 (d,  $J=16.2$  Hz, 1H, -HC=CH-), 6.49 (s, 1H, pyrrole-H), 5.97 (s, 1H, pyrrole-H), 2.39 (s, 3H, CH<sub>3</sub>), 2.33 (s, 3H, CH<sub>3</sub>), 2.18 (s, 3H, CH<sub>3</sub>) (Figure 3).  $^{13}C$  NMR (125 MHz, CDCl<sub>3</sub>,  $\delta$ , ppm) 169.8, 165.2, 162.9, 161.3, 158.8, 151.3, 144.4, 143.3, 141.0, 139.3, 138.2, 136.0, 135.7, 133.8, 132.2, 130.0, 129.3, 128.4, 126.9, 125.8, 122.9, 121.8, 120.4, 119.3, 118.8, 115.8, 114.3, 112.7, 110.3, 104.4, 40.1, 21.2, 17.0, 15.1 (Figure 4).

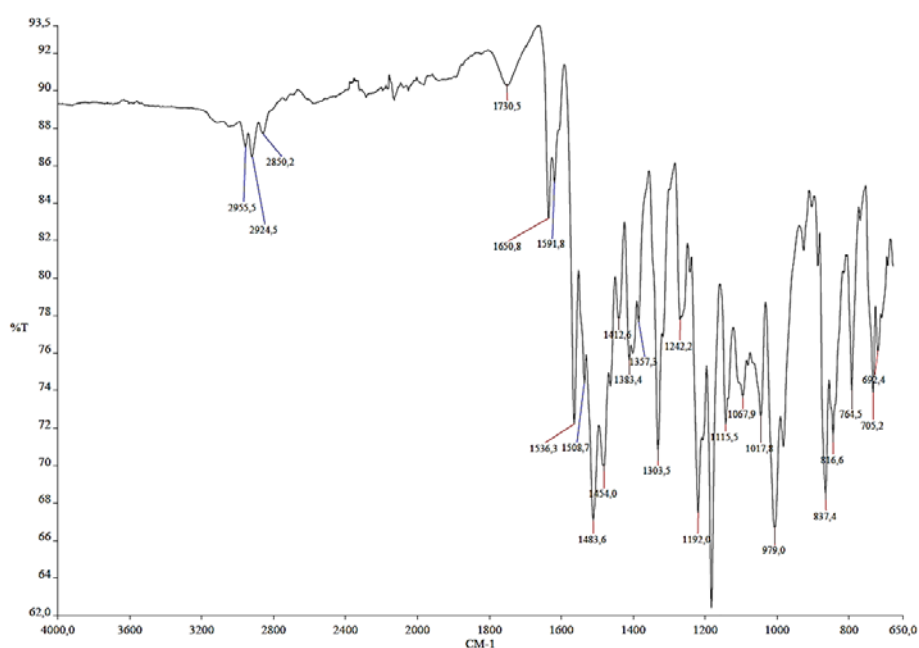
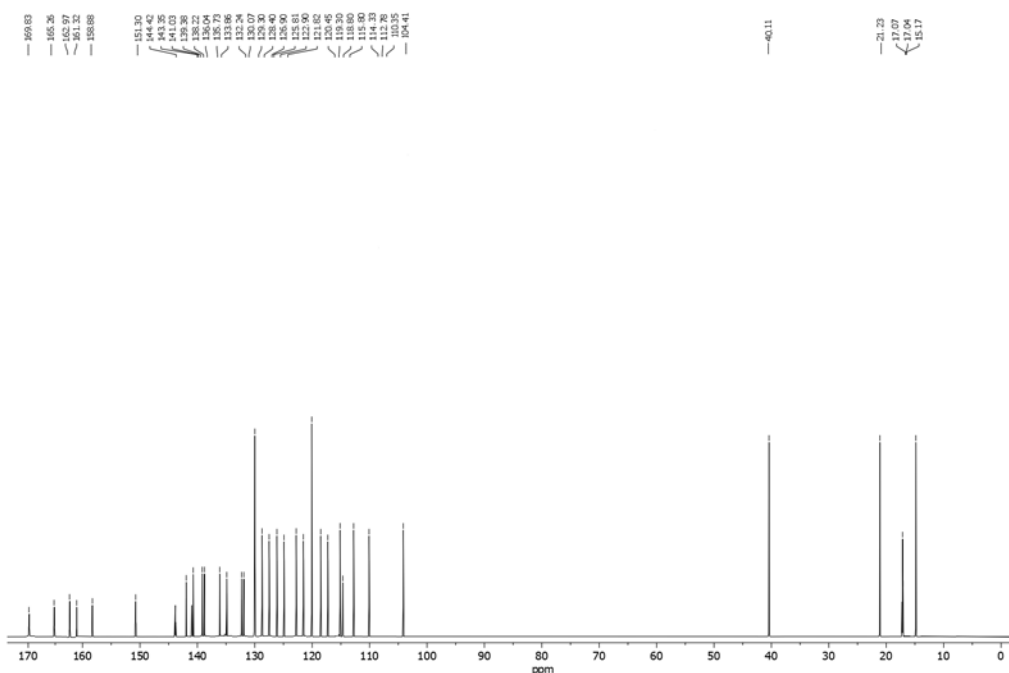


Figure 1. FTIR spectra of SubPcBodiPy







**Figure 4.**  $^{13}\text{C}$  NMR spectra of SubPcBodiPy

### 3. Results and Discussions

All these spectroscopy experiments were performed using a micropipette in a quartz spectroscopic cuvette at 25 °C. The photophysical properties of SubPcBodiPy were investigated in THF solutions using fluorescent spectroscopy and UV-visible absorption techniques and compared with its precursors (BodiPy and SubPcCl) (Figure 5). According to Figure 5a, the absorption maximum of SubPcBodiPy was observed at 594 nm like its precursor BodiPy, and according to Figure 5b, the emission maximum of SubPcBodiPy was found at 609 nm. The fluorescence lifetimes of the compounds (Figure 6) were measured directly with a single exponential calculation and lifetime measurements were made for each compound separately:  $3.0 \pm 0.006$  (SubPc),  $2.9 \pm 0.004$  (BodiPy),  $2.9 \pm 0.005$  (SubPcBodiPy).

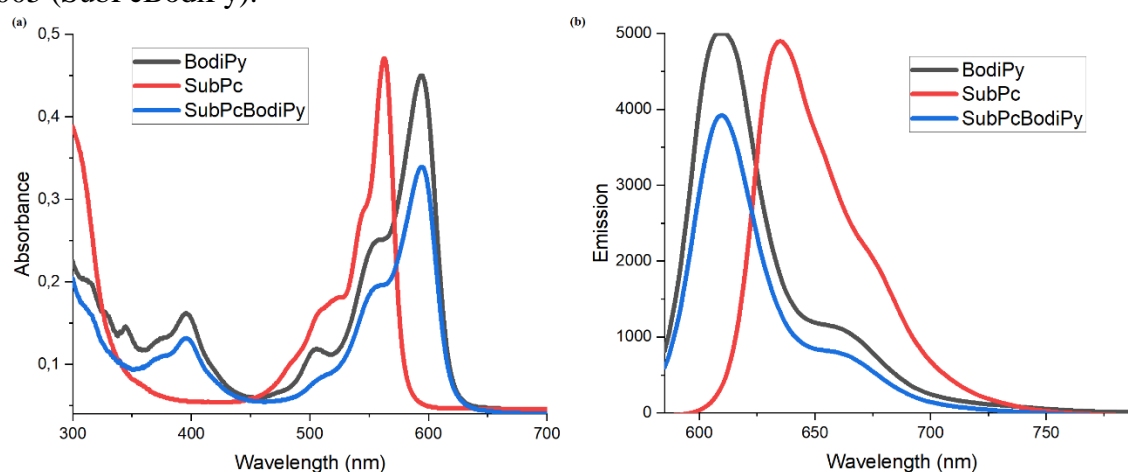


**Figure 5.** (a) Normalized absorption and (b) normalized emission spectra of compounds (Excitation wavelength: 510 nm)

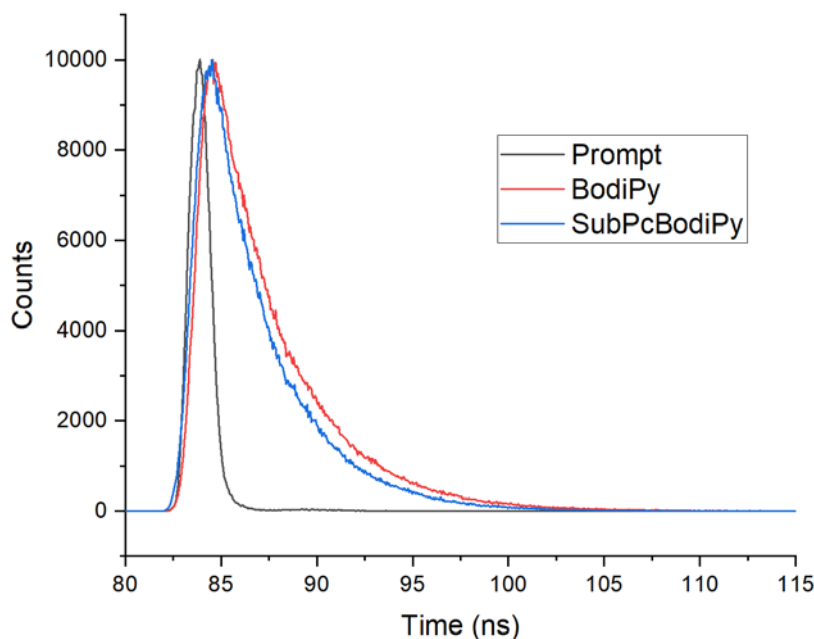


**Figure 6.** Fluorescence lifetime decay of BodiPy and SubPcBodiPy

Novel SubPcBodiPy derivative was prepared according to Scheme 1. The phenol containing Bodipy compound was first prepared by treating 2,4-dimethylpyrrole with 4-hydroxybenzaldehyde via sequential condensation, oxidation, and complexation reactions according to the literature [10]. In the following step this compound underwent Knoevenagel condensation reaction with pyrene-1-carboxaldehyde in the presence of piperidine to give the mono-styryl compound BodiPy. BodiPy was then treated with the commercially available boron (III) subphthalocyanine chloride in toluene to afford SubPcBodiPy compound. This novel compound was characterized by elemental analysis and FTIR, mass,  $^1\text{H}$  and  $^{13}\text{C}$  NMR spectrometry. All the results were consistent with the predicted structures as shown in the experimental section.

#### 4. Conclusion and Future Work

In this study, a novel BODIPY-subphthalocyanine dyad (SubPcBodiPy) was synthesized and fully characterized by mass, FTIR, mass, NMR ( $^1\text{H}$  and  $^{13}\text{C}$ ) spectroscopy and elemental analysis. The photophysical characteristics of all compounds were examined by using UV-visible absorption and fluorescence spectroscopy in THF, and according to the obtained data, SubPcBodiPy retained the unique photophysical properties of its precursor BodiPy and a photosensitizer was obtained. Future studies will help determine the possibility of this compound for the photodynamic therapy of cancer and its ability to produce singlet oxygen will help.

**Peer-review:** Externally peer - reviewed.

**Conflict of Interest:** No conflict of interest was declared by the authors.

**Financial Disclosure:** The authors declared that this study has received no financial support.

**Acknowledgment:** This study has been presented at the IMSEC 2021 (6th International Mediterranean Science and Engineering Congress) held in Antalya (Turkey), October 25-27, 2021.

## References

- [1] Ward M. D., (1997) "Photo-induced electron and energy transfer in non-covalently bonded supramolecular assemblies", *Chemical Society Reviews*, vol.26, pp.365-375.
- [2] Balzani V., Bergamini G., Ceroni P., (2008) "From the photochemistry of coordination compounds to light-powered nanoscale devices and machines", *Coordination Chemistry Reviews*, vol. 252, pp.2456-2469.
- [3] Holten D., Bocian D. F., Lindsey J. S., (2002) "Probing electronic communication in covalently linked multiporphyrin arrays. A guide to the rational design of molecular photonic devices" *Accounts of Chemical Research*, vol.35, pp.57-69.
- [4] Loudet A., Burgess K., (2007) "BODIPY dyes and their derivatives: syntheses and spectroscopic properties" *Chemical Reviews*, vol.107, pp.4891-4932.
- [5] Claessens C. G., González-Rodríguez D., Torres T., (2002) "Subphthalocyanines: singular nonplanar aromatic compounds synthesis, reactivity, and physical properties" *Chemical Reviews*, vol.102, pp.835-854.
- [6] Mutolo K.L., Mayo E.I., Rand B.P., Forrest S.R., Thompson M.E., (2006) "Enhanced open-circuit voltage in subphthalocyanine/C60 organic photovoltaic cells" *Journal of American Chemical Society*, vol.128, pp.8108-8109.
- [7] Xu S., Chen K., Tian H., (2005) "A colorimetric and fluorescent chemodosimeter: fluoride ion sensing by an axial-substituted subphthalocyanine" *Journal of Materials Chemistry A*, vol.15, pp.2676-2680.
- [8] Morse G. E., Helander M. G., Maka J. F., Lu Z. H., Bender T. P., (2010) "Fluorinated phenoxy boron subphthalocyanines in organic light-emitting diodes" *ACS Applied Materials & Interfaces*, vol.2(7), pp.1934-1944.
- [9] Renshaw K. C., Xu X., Forrest S. R., (2010) "A monolithically integrated organic photodetector and thin film transistor" *Organic Electronics*, vol.11, pp.175-178.
- [10] Liu J.Y., Yeung H.S., Xu W., Li X., Ng D.K.P., (2008) "Highly Efficient Energy Transfer in Subphthalocyanine-BODIPY Conjugates" *Organic Letters*, vol.10, pp.5421-5424.
- [11] Cetindere S., Cosut B., Yesilot S., Durmus M., Kilic A., (2014) "Synthesis and properties of axially BODIPY conjugated subphthalocyanine dyads" *Dyes and Pigments*, vol.101, pp.234-239.
- [12] Tanrıverdi-Eçik E., Ozcan E., Kandemir H., Sengul I. F., Çosut B., (2017) "Light harvesting systems composed of carbazole based subphthalocyanine-BODIPY enhanced with intramolecular fluorescence resonance energy transfer (FRET)" *Dyes and Pigments*, vol.136, pp.441-449.
- [13] Ozcan E., Kesan G., Topaloglu B., Tanrıverdi-Eçik E., Dere A., Yakuphanoglu F., Çosut B., (2018) "Synthesis, photophysical, DFT and photodiode properties of subphthalocyanine-BODIPY dyads" *New Journal of Chemistry*, vol.42, pp. 4972-4980.
- [14] Kazan H. H., Ozcan E., Çosut B., Yenilmez-Çiftçi G., Tanrıverdi-Eçik E., (2020) "Novel BODIPY-subphthalocyanine dyads with reasonable photodynamic therapy behaviours" *New Journal of Chemistry*, vol.44, pp.13738-13744.

# Fractal Adsorption Characteristics and Statistical Analysis Approach of Complex Dye Molecule on Metal Oxide Particles—A Case Study of Reactive Black 5(RB 5) Adsorption onto NiO Nanoparticles

\*<sup>1</sup> Ferda Gönen , <sup>1</sup> Gizem Biçer 

<sup>1</sup> Mersin University, Department of Chemical Engineering, 33343, Çiftlikköy/Mersin.

\* Corresponding author, e-mail: gonenf74@gmail.com

Submission Date: 31.01.2022

Acceptation Date: 01.04.2022

**Abstract** - In this study, environmental conditions for high efficient dye adsorption; initial pH, initial dye concentration, temperature, adsorbent concentration were determined as 6.0, 40°C, 100 mgL<sup>-1</sup> and 1 g L<sup>-1</sup>, respectively. Obtained results from SEM, FT-IR and XRD analyzes were evaluated and compared with founding in literature. It was found that the equilibrium data can be best represented with Langmuir isotherm model, and it was concluded that RB 5-NiO adsorption system behavior was explained the pseudo-second order kinetic model successfully. It was concluded that dye-nano-adsorbent system was exothermic ( $\Delta H < 0$ ) and voluntary ( $\Delta G < 0$ ). In thermodynamic analysis, RB 5 to NiO system adsorption proved that system has no structural change ( $S < 0$ ) at the adsorbent-solution interface. RSM (Response Surface Method) was used to express the interaction between process variables and responses and to examine the adsorption data. Removal percentages were determined theoretically using Design Expert 9.0.6 software program, and quadratic regression model was developed. It was seen that the adsorption parameters for the highest color removal obtained by the classical method were compared with the parameters found from RSM approach obtained under the same experimental conditions support each other.

**Keywords:** Adsorption, NiO, nanoparticle, RSM, Reactive Black 5 dye.

## 1. Introduction

Water has a great importance for living creatures to survive and has also played an important role in the development of civilizations. On a global scale, water limited in terms of availability is a renewable source [1-4]. The numerical expression of the total water in the world is 1.4 billion km<sup>3</sup>. The ratios of 97.5% and 2.5% worldwide water are known as salt water in oceans and seas and fresh water in rivers and lakes, respectively. Most water sources are contaminated by liquid organic pollutants caused by the textile, paper, food and cosmetics industries. These liquid pollutants not only cause environmental pollution but also they have toxic and carcinogenic effects. Besides, they can be easily noticed even at very low concentrations. Because of these damaging characteristics, waterborne diseases kill about 12 million people every year, according to the World Health Organization (WHO) report [3]. The pollution of water resources and the attention of environmental problems have resulted in the restructuring of national legislation in the world and in our country.

The main industrial wastewater suppliers produce color pollution are textiles, leather, printing, laundry, tannery, rubber, plastic, paint and etc. The wastewater generated in textile industries vary considerably in terms of quantity and composition. Because of these changes is the composition of wastewater as a result of the renewed business processes and the differences in the process technologies applied. Turkey's textile industry effluents are the largest colored wastewater among the other industries. Paper, leather, rubber and paint are among the sectors that produce colored wastewater after the textile sector.

---

<sup>1</sup> Corresponding author: Tel: +90 324 3610001

E-mail: ferda@mersin.edu.tr, gonenf74@gmail.com



In scientific investigations carried out, it was determined that color removal efficiencies at high rates were obtained by choosing the treatment processes based on different principles together. Applications of biological treatment and other treatment technologies are frequently encountered for better quality wastewater discharge to the receiving environment [6]. The main methods used in the treatment of wastewaters containing different types and numbers of pollutants in the world and in Turkey are membrane filtration, ion exchange, oxidation, coagulation-flocculation, adsorption, aerobic and anaerobic biological treatment technologies. Many highly colored wastewater producers having low initial investment cost in Turkey have preferred biological treatment for own wastewater. Biological treatment processes are known as an economical and ecofriendly technologies. While a more efficient dye removal can be achieved by this technology for most pollution removal, it may be insufficient in color removal by self. The reason for this sufficiency is more than one pollutant at high concentrations and the resistance of raw materials such as melanoidin, lignin and their derivatives etc. in wastewater. In this case, more than one treatment technologies can be used together for high pollutant removal efficiency. Therefore, the desired level of color removal can be obtained with one more than combined treatment process.

Adsorption method is often preferred in color removal from wastewater due to the reasons such as simplicity, fast and economical process conditions, high efficiency and harmless end-product from removal process. In this method, zeolite, clay, chitosan, nanoparticles are preferred as an adsorbent. In this experimental study, the adsorption of anionic RB 5 dye with synthesized materials of Ni-based nanomaterials, the interaction between the adsorbent and the solution using classical methods with the help of equilibrium, kinetic and thermodynamic models were investigated and finally the comparison of experimental equilibrium removal percent values with theoretical ones from RSM were evaluated in a batch system.

The primary function of grinding media is to crush and grind ore particles inside rotating mills, such as ball, rod, and semi-autogenous mills, and sometimes in stirred mills such as Vertimill, SVM mills, Sala Agitated Mill, HIGMill, Tower Mill, and ISAMill [2]. In recent years, grinding charges with unconventional shapes have appeared on the market. One example is the cylindrically shaped media called Cylpebs. Cylpebs have greater surface area and higher bulk density than balls of similar mass and size, due to their shape. Cylpebs of the same diameter and length have 50% greater surface area, and 45% greater weight, than balls of the same material. In addition, they have 9% higher bulk density than steel balls, and 12% higher than cast balls. The objective of this paper is to compare Cylpebs and ball grinding media in terms of grinding efficiency for fabrication of nano sized calcite [3-4]. Calcite ( $\text{CaCO}_3$ ) was chosen as test material for this study. It is a salt, widely used in the ground nano-form, in paints, food or pharmaceuticals industries and as filler in the paper making process (Garsia et al., 2002).

## 2. Materials and Methods

### 2.1. Reagents

$\text{NiSO}_4$  and  $\text{Ni}(\text{OH})_2$  used in nanomaterial synthesis were purchased from Sigma–Aldrich. Also, RB 5 dye was purchased from Sigma–Aldrich. Its Molecular Weight[MW]: 991.82; Molecular Formula [MF]:  $\text{C}_{26}\text{H}_{21}\text{N}_5\text{Na}_4\text{O}_{19}\text{S}_6$ ;  $\lambda_{\text{max}}$ : 597 nm. The corresponding chemical structure of RB 5 dye is shown in Figure 1.

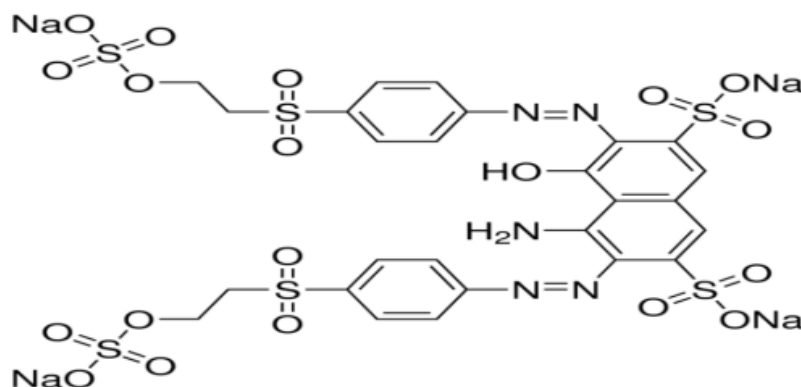


**Figure 1.** The chemical structure of RB 5.

## 2.2. Synthesis of nanoparticles

In this method, firstly, 0.5 M NiSO<sub>4</sub> solution and 1 M NaOH solution were prepared. Then solutions were mixed and 2.0 grams of agar was added into 25 mL of solution containing this mixture. It was mixed on a shaker for 1 hour at a stirring speed of 200 rpm at room conditions. The solid-liquid mixture formed was separated by filtration and the solid part was taken. Then it was subjected to calcination process at 250°C for 4.5 hours [7- 13].

## 2.3. Characterization experiments

FTIR (Perkin Elmer, Fourier Transform Infrared Spectrometer), SEM (ZeissSupra 55 Area Emission, Scanned Electron Microscope), and XRD (Philips, X'Pert brand X-Ray Diffractometer) were used for identification of morphological properties and identification of phases and crystal structures of synthesized particles at Advanced Materials Research Center (MEITAM).

## 2.4. Color removal experiments

Color removal experiments were carried out at 120 rpm constant agitation rate in a batch system. Desired amount of NiO based nanoparticles were weighed and then mixed with 150 mL RB 5 dye solutions adjusted to the desired pH values with NaOH and HCl solutions. Samples were taken and centrifuged at specific time intervals (0,5, 15, 30, 60, 120, 180, 240, 300, 360, 420, 1440, 1500, 1600, 1800, 2000) in the shaking water bath. Centrifuged samples were diluted and analyzed by UV-Vis spectrophotometer at 663 nm wavelength. Dye removal % was determined by the following formula;

$$\text{Dye Removal \%} = ((C_o - C_e) / C_o) \times 100 \quad [1]$$

where, C<sub>o</sub> and C<sub>e</sub> are;

the initial and equilibrium dye concentration in mg L<sup>-1</sup>, respectively. The amount of dye adsorbed per unit of the adsorbent at equilibrium was calculated in terms of q<sub>e</sub> (mg g<sup>-1</sup>) using equation given below,

The equilibrium amount of dye removal per unit of the nanoparticle was determined in terms of q<sub>e</sub> (mg g<sup>-1</sup>) using equation given below.

$$\text{Removal capacity (q}_e\text{)} = (C_o - C_e)V/m \quad [2]$$

Where V is the volume of dye solution (L) and m is the mass of the adsorbent(g).

## 3. Results and Discussions

### 3.1. Characterization studies for NiO based nanoparticles

SEM analyzes were carried out to investigate the surface properties of the nanoadsorbent used in RB 5-NiO system before and after adsorption. SEM images for NiO based nanoparticles before and

after adsorption are presented in Figure 2. It can be seen from the SEM images that the nanoparticles, which have a porous surface before adsorption, are filled with dye molecules after adsorption.

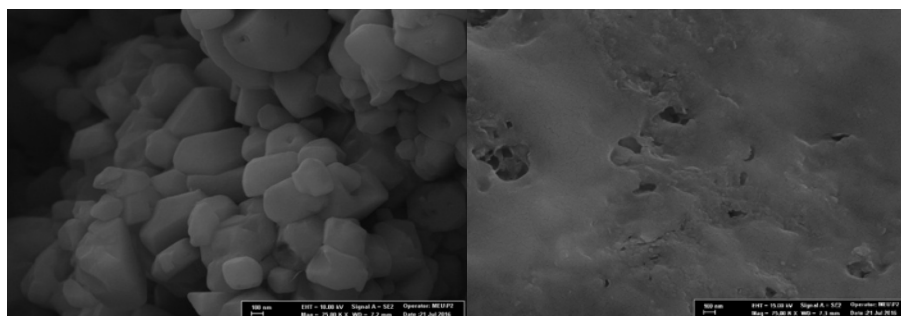


**Figure 2.** SEM images of RB 5 dye before and after adsorption on NiO-based nanomaterial adsorption.

In order to explain RB 5-NiO adsorption mechanism, FT-IR analyzes of the adsorbent were used before and after the adsorption and presented in Figure 3. In the spectrum of NiO based material; Peaks around 3644 and 3272.34  $\text{cm}^{-1}$  correspond to  $\text{OH}$  group, vibration 1038.43 $\text{cm}^{-1}$  corresponds to-Si-O-Si- group, adsorption peaks at 867.91 $\text{cm}^{-1}$  correspond to simple hetero-oxy compound frequencies of aromatic phosphates (P-O-C stress) [7, 8, 9]. Tension band at 474.38  $\text{cm}^{-1}$  indicates the Ni – O bond [10, 11].

The graph of XRD spectra (X-Ray Diffractometry) analysis for adsorbent phases and crystal properties used in the adsorption of RB 5 dye is given in Figure 4. In XRD analysis, all data were obtained between  $10^\circ$  -  $80^\circ$  of  $2\theta$  value.

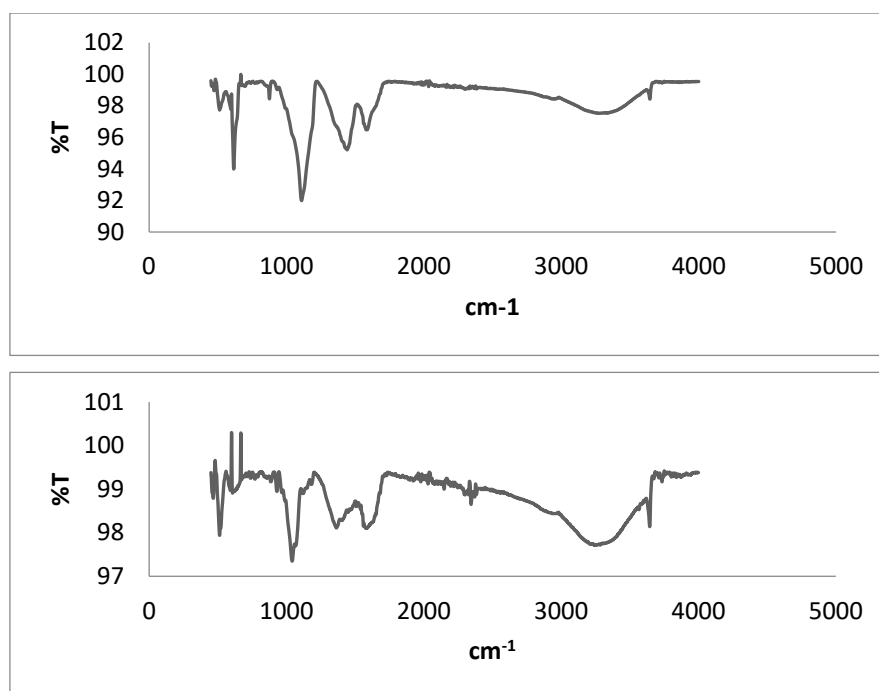


**Figure 3.** FT-IR spectra of RB 5 dye before and after adsorption.

Figure 4 and 5 show the spectra of XRD (X-ray Diffractometer) analysis spectra to determine the adsorbent phases and crystal properties used in the adsorption of RB 5. The highest characteristic peaks were obtained as  $18.6^\circ$  -  $19.0^\circ$  -  $31.6^\circ$  -  $37.9^\circ$  -  $38.8^\circ$  at  $2\theta$  value for the NiO particle, respectively. In XRD analysis, the presence of large-scale peaks in the structure of the NiO-based nanomaterial shows that the crystals are small or structurally irregular, or both are valid, as well as regions of amorphous structure on the material other than the crystal structure.

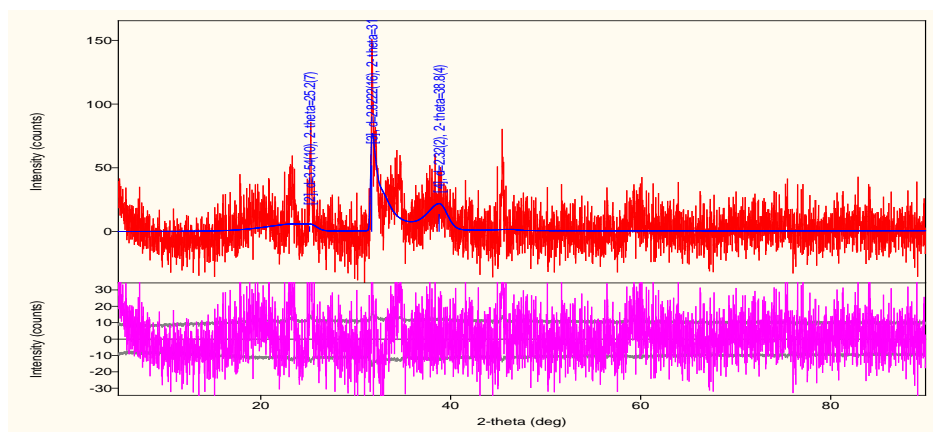


Figure 4. XRD analysis of RB 5 dye before adsorption on NiO based nanomaterials.

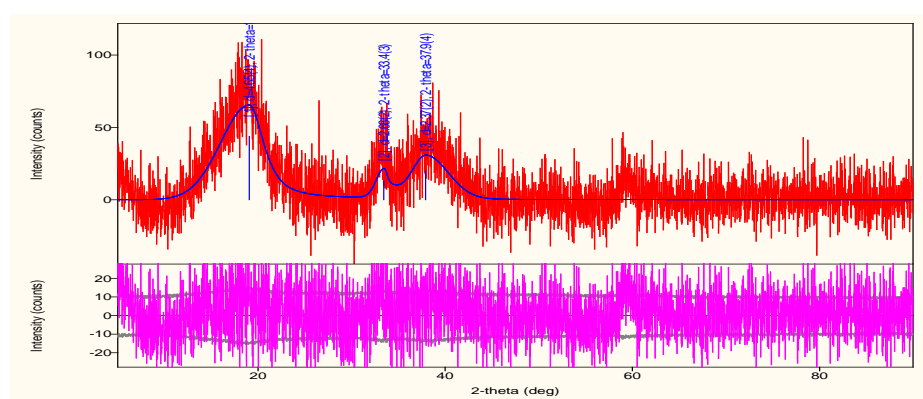


Figure 5. XRD analysis of RB 5 dye after adsorption on NiO based nanomaterials.

### 3.2. Effects of Environmental Conditions on Adsorption Study

While the effects of parameters such as pH, temperature, initial dye and adsorbent concentration on adsorption were examined by classical method. In this method, the environmental condition parameter value was changed within a determined certain experimental range to investigate its effect, while the other environmental adsorption parameters values were kept constant. pH, temperature, concentration, adsorbent concentration were examined in the range of pH: 2-10, temperature 30°C-60°C, initial concentration 50 mg L<sup>-1</sup>-500 mg L<sup>-1</sup>, adsorbent concentration 0.5 g L<sup>-1</sup>-3 g L<sup>-1</sup> respectively.

Initial pH is the most important parameter for color removal from wastewater. In this part, pH value was changed between 2.0 and 10. The initial dye solution pH was increased from 2 to 6 the adsorbed dye amount per unit adsorbent mass increased from 21.83 mg g<sup>-1</sup> to 60.85 mg g<sup>-1</sup>, respectively. On the other hand, the removal dye percent increased from 22.73 % to 62.19%, respectively. From experimental data, the favorable pH value for the highest removal efficiency is determined as 6.0.

In temperature effect part for adsorption of RB 5 on NiO nanoparticles, when the temperature was increased from 30 °C to 60 °C, it was observed that the amount of material adsorbed per unit adsorbent mass decreased from 79.14 to 34.83 at equilibrium. Also the removal dye percent increased from 22.73 % to 62.19%, respectively. In this study, the preferable temperature value for high yield

removal was determined as 40 °C ( $q_d=82.48 \text{ mgg}^{-1}$ , 80.19%) and all thermodynamic parameters were evaluated at this temperature value.

In the range of 25–2000 $\text{mg}\cdot\text{L}^{-1}$  dye concentration. When the initial RB 5 concentration was increased from 25  $\text{mg L}^{-1}$  to 2000  $\text{mgL}^{-1}$  in RB 5 dye adsorption, the adsorbed dye amount per unit adsorbent mass increased from 25  $\text{mgg}^{-1}$  to 1489.79  $\text{mgg}^{-1}$ , while dye removal percentage decreased from 95.15 to 76.93 respectively.

In the third part of the adsorption effect parameter investigation, the contact time for 50  $\text{mgL}^{-1}$  initial dye concentration for equilibrium was found approximately 20 minutes, while this equilibrium time was found to be approximately 100 minutes for higher concentration values. It is due to the presence of empty active areas on the adsorbent surface at low dye concentrations. However, as the initial dye concentration was increased, the driving force was increased too, and the active areas became saturated with dye molecules [12].

In the range of, 0.2 to 3.0 $\text{g L}^{-1}$  adsorbent dosage range, adsorbent amount was decreased with the increasing adsorbent dose. This was caused that the interaction of the adsorbent particles and agglomeration when the adsorbent was increased. From the same table, it is seen that the increase of adsorbent dosage increases the adsorption yield, and it is observed that the color removal is detected as 98.53% when the amount of adsorbent is 3g in 1L. The adsorbed dye removal percentage value increased from 76.77 % to 91.50%, while dye amount per unit adsorbent mass removal percentage decreased from 95.15 to 76.93 respectively.

In RB 5-NiO adsorption system, the initial pH, the initial dye concentration, temperature and adsorbent concentration 6, 100  $\text{mg L}^{-1}$ , 40°C and 0.5  $\text{g L}^{-1}$  were determined as desirable removal conditions. Under highest removal conditions for adsorption, the amount of RB 5 adsorbed per unit mass of adsorbent at equilibrium was 75.89  $\text{mg g}^{-1}$  and the removal percentage was 74.38%.

### 3.3. Adsorption Equilibrium

In this part, Langmuir, Freundlich, and Temkin isotherm models [2, 7, 12-18, 20-22, 24-26] have been examined in order to determine the correlation that best represents the experimental equilibrium data obtained at different temperatures in the adsorption of RB 5 dye to NiO-based nanomaterials results are presented below.

**Table 1.** Isotherm model constants for RB 5 dye on NiO adsorption.

Langmuir Model Constant				
	30°C	40 °C	50 °C	60 °C
$Q^{\circ} (\text{m g}^{-1})$	126.528	140.845	116.279	136.986
$b (\text{L mg}^{-1})$	0.078	0.039	0.012	0.005
$R^2$	0.930	0.994	0.997	0.981
$R_L$	0.113	0.204	0.454	0.666
Freundlich Model Constant				
	30°C	40 °C	50 °C	60 °C
$1/n$	0.172	0.131	0.260	0.400
$n$	5.803	7.621	3.840	2.495
$K_f$ [( $\text{mg/g}$ )/( $\text{L/mg}$ ) $^{1/n}$ ]	45.979	61.775	20.701	8.786
$R^2$	0.964	0.983	0.991	0.941
Temkin Model Constant				
	30°C	40 °C	50 °C	60 °C
$A_t (\text{L g}^{-1})$	4.187	12.146	0.213	0.055
$B (\text{J mol}^{-1})$	17.224	15.914	22.027	30.843
$R^2$	94.07	0.987	0.996	0.961

According to Table 1,  $R^2$  values in the Langmuir isotherm model are high and the dimensionless separation factor  $R_L$  is between zero and one. It is seen that the obtained data fit better Langmuir



isotherm model. It can be concluded that NiO-based nanomaterials are suitable adsorbent for the adsorption of RB 5 dye and it is concluded that adsorption is a viable process for RB 5-NiO system.

In literature, Lingamdinne et al. (2017) applied three different isotherm models to describe the adsorption of Pb(II) and Cr(III) by using graphene oxide based inverse spinel nickel ferrite composite. The Langmuir adsorption isotherm data fit well with the experimental adsorption data and Langmuir isotherm regression coefficients was higher than the Freundlich and Temkin isotherm coefficients compared to the other two models. Thus, it was concluded that the Langmuir isotherm is suitable for RB 5-NiO adsorption system [13].

### 3.4. Adsorption Kinetics

In order to model the adsorption kinetics of RB 5 dye solution onto NiO based nanomaterials, pseudo-first and pseudo-second order kinetic models [9, 10, 12-18, 20-24-26] were applied to the adsorption data obtained at different initial dye concentrations; experimental findings are presented in Table 2 and Table 3.

**Table 2.** Pseudo-first order rate constant and regression coefficient values of RB 5 dye adsorption onto NiO-based nanomaterial.

$C_0$ (mg L <sup>-1</sup> )	$q_{d,experimental}$	$q_{d,theoretical}$	$k_1$ (dk <sup>-1</sup> )	$R^2$
50	42.60	28.95	0.035	0.921
100	82.48	97.99	0.052	0.960
200	110.97	99.72	0.039	0.992
300	122.76	88.88	0.028	0.942
400	129.26	103.06	0.033	0.990
500	132.52	104.81	0.028	0.987

**Table 3.** Pseudo- second order rate constant and regression coefficient values of RB 5 dye adsorption to NiO-based nanomaterial.

$C_0$ (mg L <sup>-1</sup> )	$q_{d,experimental}$	$q_{d,theoretical}$	$k_2$ (g mg <sup>-1</sup> .min <sup>-1</sup> )	$R^2$
50	42.60	44.44	0.003	0.999
100	82.48	87.71	0.001	0.999
200	110.97	116.27	0.001	0.999
300	122.76	128.20	0.001	0.999
400	129.26	135.13	0.001	0.999
500	132.52	138.88	0.001	0.999

In the adsorption kinetic model studies, it was seen that the regression coefficients of the pseudo-first-order kinetic model were quite low. At the same time, the difference between the calculated  $q_d$  values and the experimental  $q_d$  values indicates that the process does not fit the pseudo-first order kinetic model. RB5-NiO desorption system was determined as more compatible with second-order kinetics in the studies, due to the high  $R^2$  values of the pseudo-second-order kinetic model and the theoretical  $q_a$  values calculated from model equation.

### 3.5. Adsorption Thermodynamics

Thermodynamic parameters such as Gibbs free energy change ( $\Delta G$ ), enthalpy change ( $\Delta H$ ) and entropy change (S) in the adsorption of RB 5 dye onto NiO-based nanoparticle were determined according to Van't Hoff equation [10, 12-18, 20-22, 24-26] Gibbs free energy (G), enthalpy ( $\Delta H$ ) and entropy ( $\Delta S$ ) values calculated from thermodynamic study data are presented in Table 4, respectively.

**Table 4.** Pseudo- second order rate constant and regression coefficient values of RB 5 dye adsorption to NiO-based nanomaterial.

T(K)	$\Delta G$ (J mol <sup>-1</sup> )	$\Delta H$ (J mol <sup>-1</sup> )	$\Delta S$ (J mol <sup>-1</sup> K <sup>-1</sup> )	T $\Delta S$ (J mol <sup>-1</sup> )
298	-2640.95			-42789.8
303	-3359.66			-43507.7
313	-3639.81	-46558.4	-143.59	-44943.6
323	559.15			-46379.5

333	1734.38			-47815.4
-----	---------	--	--	----------

According to the adsorption experimental results, all thermodynamic parameters were found to be negative for RB 5-NiO adsorption system. In other words, the adsorption process was determined to be exothermic ( $\Delta H < 0$ ), voluntary ( $\Delta G < 0$ ) and stable ( $\Delta S < 0$ ) systems that run without structural changes at the solid/liquid interface.

#### 4. Adsorption Thermodynamics

Box-Behnken Design Expert 9.0.6 software with four variables was used to optimize parameters such as pH, initial dye concentration, temperature and adsorbent amount in the adsorption of RB 5 dye onto NiO based nanomaterial. The quadratic model was chosen for model calculations [21, 28, 29]. The factors of pH, temperature, initial dye concentration and adsorbent concentration are represented by the letters A, B, C and D, respectively. The % dye removal, which is the response value, is represented by the symbol  $R_1$ .

For the adsorption of RB 5 dye to NiO-based nanomaterial, the statistical significance of the model suggested by the program and the results were evaluated and presented with the ANOVA test shown in Table 5.

In this approximation, model equation (suggested by Design Expert 9.0.6 software) as a function of the parameters of pH, temperature, initial dye concentration and adsorbent amount is given in Equation 3 in terms of real values. In these equations A, B, C, D represent pH, temperature, dye concentration and adsorbent amount, respectively.

$$\% \text{ Removal} = -188.91152 + 35.17223 * pH + 5.95074 * T + 0.67653 * C + 23.53433 * X_o - 0.087542 * pH * T - 0.0061625 * pH * C - 0.31750 * pH * X_o - 0.014550 * T * C + 0.008 * T * X_o - 0.0192 * C * X_o - 2.21442 * pH^2 - 0.058392 * T^2 - 0.0002343 * C^2 - 8.963 * X_o^2 \quad (3)$$

**Table 5.** Box-Behnken ANOVA results for optimization in adsorption of RB 5 dye to NiO-based nanomaterial.

Source	Sum of Squares	Df	Mean Square	F Value	p-value Prob > F
Model	14151.79	14	1010.84	13.98	< 0.0001
A-pH	3328.67	1	3328.67	46.03	< 0.0001
B-T	1296.26	1	1296.26	17.93	0.0008
C-C	2.17	1	2.17	0.030	0.8650
D- $X_o$	13.27	1	13.27	0.18	0.6749
AB	110.36	1	110.36	1.53	0.2370
AC	6.08	1	6.08	0.084	0.7762
AD	1.61	1	1.61	0.022	0.8834
BC	476.33	1	476.33	6.59	0.0224
BD	0.014	1	0.014	1.991E-004	0.9889
CD	0.92	1	0.92	0.013	0.9117
A <sup>2</sup>	8142.73	1	8142.73	112.61	< 0.0001
B <sup>2</sup>	1119.66	1	1119.66	15.48	0.0015
C <sup>2</sup>	2.23	1	2.23	0.031	0.8632
D <sup>2</sup>	32.57	1	32.57	0.45	0.5131
Residual	1012.31	14	72.31		
Lack of Fit	1010.13	10	101.01	184.57	< 0.0001
Pure Error	2.19	4	0.55		
Cor Total	15164.10	28			

It was seen that the model coefficients in the equation suggested by the program were positively signed. While this situation shows the synergistic effect, the negative sign shows the antagonistic effect. According to the program results, all variables in all three equations create a positive effect.

Error percentage was found at very low levels in the study performed and were found to be 6.01%. With the help of perturbation area, the effects of all factors at a particular point in the design area have been tried to be compared. Accordingly, with the results given by the program, the results obtained under laboratory conditions are pH 6 for NiO-RB5, initial dye concentration 100 mg L<sup>-1</sup>; temperature 40°C; adsorbent concentration 0.5 g L<sup>-1</sup> support each other. By examining the ANOVA tests and the sum of squares values, it was seen that significant results were obtained for the adsorption system.

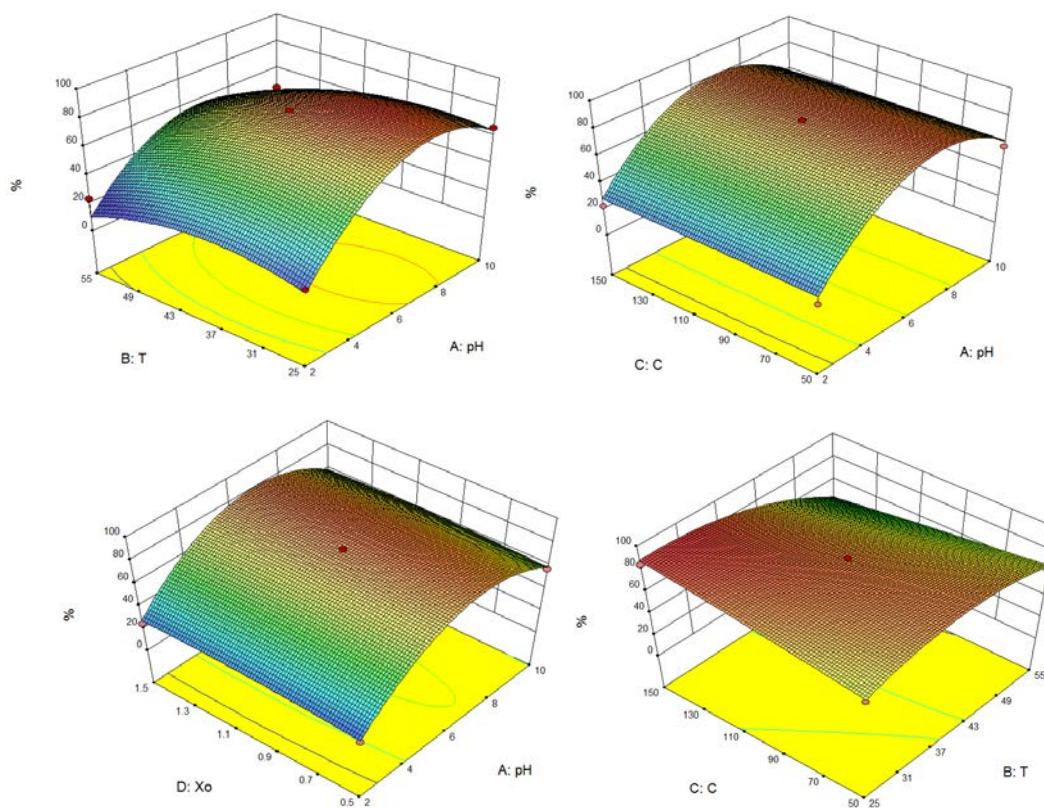


**Figure 6.** Three-dimensional graphs in the adsorption of RB 5 to NiO.

Perturbation analysis for the system, response surface designs show how the response changes as each factor moves from the selected reference point and other constant factors at the reference value. By using Perturbation chart, the effects of all factors in the design area in optimum operating conditions are compared. The perturbation area helps to compare the effect of all factors at a given point in the design field [21, 28, 29].

According to Figure 6, optimum conditions were found as pH 6, temperature 40 °C, dye concentration 100 mg L<sup>-1</sup> and adsorbent amount 1g L<sup>-1</sup>. When the program results are evaluated, the results of the program and the results obtained in laboratory conditions support each other.

#### 7. Investigation of the Validity of the Model Obtained in the Answer Surface Method Outside the Selected Investigation Range

Optimization of parameters such as pH, initial dye concentration, temperature and adsorbent concentration, which affect the adsorption of RB 5 dye to NiO based nanomaterials, were examined within specified ranges and the results obtained were presented in classical optimization results.

In this section, the probability of the using model equation has been investigated with the proses variables outside the selected experimental range by applying model equation. From RB 5-NiO adsorption data evaluation, it is seen that adsorption system is very sensitive to pH and temperature

changes. If adsorption data outside the selected range is used in model equation, some deviations can be occurred in system estimation. The main reason for this deviation is a large number of variables (adsorption parameters effecting sorption yield) in the system. As a result, for highly accurate estimation, number of adsorption variables and experimental range for model equation should be selected carefully. Model equations with a wide range of values can offer the researcher quite a lot of estimation possibilities.

## 5. Conclusions

In the adsorption of RB 5 dye to NiO based nanoparticles, the initial pH, the initial dye concentration, temperature and adsorbent concentration were determined as 6, 100 mg L<sup>-1</sup>, 40°C, 0.5 mg L<sup>-1</sup> for the highest removal yield. At these conditions, the amount of RB 5 adsorbed per unit mass of adsorbent at equilibrium was 75.89 mg g<sup>-1</sup> and the removal percentage was 74.38%. For equilibrium model description, Langmuir, Freundlich and Temkin isotherm models were applied to the adsorption equilibrium data obtained at different temperatures during the adsorption of RB 5 dye onto NiO-derived nanoparticles; It was observed that equilibrium data fit better with Langmuir isotherm model.

For adsorption kinetic model investigation, the adsorption data results indicated that the conformity of theoretical values with the experimental ones prove that adsorption process cannot be represented by the pseudo-first-order kinetic model. It was concluded that adsorption system was best represented with second-order kinetic model due to the high R<sup>2</sup> values from the model equation and the conformity of theoretical values with the experimental ones.

Thermodynamic parameters such as enthalpy change ( $\Delta H$ ), entropy change ( $\Delta S$ ), free Gibbs energy change ( $G$ ) were determined with the help of the data obtained at different temperatures in the adsorption of RB 5 dyes to NiO. All thermodynamic parameters were found to be negative in the adsorption of RB 5 to NiO. In other words, the adsorption process was determined to be exothermic ( $\Delta H < 0$ ), voluntary ( $\Delta G < 0$ ) and stable ( $\Delta S < 0$ ) systems that without structural changes at the solid/liquid interface.

In characterization studies; FT-IR was used for the determination of functional groups in the characterization of NiO nanomaterials. It was observed that there were slight shifts from the peaks formed in the FT-IR spectra after the peaks formed in the FT-IR spectra before the adsorbent adsorption. At the second step, in order to determine crystal structure and phase analysis XRD was used. Finally, SEM analyzes were made for surface morphology and it was observed that the pores were filled with dye molecules after dye adsorption.

Finally, parameters affecting RB 5-NiO adsorption system were optimized by using the Response Surface Method (RSM) program. It was observed that the coefficients in the model equations offered by the program were positively signed representing synergistic effect

Accordingly, to the RSM program results, the experimental results carried out in laboratory conditions (conditions for the highest adsorption yield: pH 6, 100 mg L<sup>-1</sup> initial dye concentration; 40°C temperature; 0.5 mg L<sup>-1</sup> adsorbent concentration) confirm classical approach results with great accuracy.

In future studies, it may be aimed to reduce the particle size to even smaller sizes. In this case, a more efficient dye removal can be achieved by increasing the surface area. As a result of the increase in particle size, high dye removal percentages and equilibrium time reduction can be achieved. Also, high technologic processes can be developed for desorption of nanoparticle, to use the sustainable adsorbent repeatedly.

As the future subject related with this investigation under laboratory conditions, batch system results can be adapted to the continuous system and proposed for large-scale applications in order to



treat high volume wastewater containing single or/and more than one pollutant with different flow reactors.

**Peer-review:** Externally peer - reviewed.

**Author contributions:** Concept – F.G.; Data Collection &/or Processing – F.G., G.B.; Literature Search - F.G., G.B.; Writing – F.G., G.B.

**Acknowledgment:** We would like to thank Mersin University Chemical Engineering Laboratories and Advanced Technology Education, Research and Application Center, which was used in determination of particle surface properties in experimental studies.

**Conflict of Interest:** No conflict of interest was declared by the authors.

**Financial Disclosure:** The authors declared that this study has received no financial support.

## References

- [1] Akram, M.W., Abdul Motin, S. M., Hoque, M.A., and Mustafi N.N., (2019). Design, construction and performance test of a solar still for water desalination in Bangladesh perspective. Conference Paper in AIP Conference Proceedings, 2121, 130001, <https://doi.org/10.1063/1.5115947>
- [2] Rahman, M.H., Mamtaz, R., and Ferdausi, S.A., (1997). Pilot solar desalination plants in Bangladesh. WEDC CONFERENCE. 23(1997), 178–181.
- [3] Saleh, A.S., (2015). Solar Desalination in Bangladesh: Progress, Prospect, and Challenges, Proceedings of the International Conference on Mechanical Engineering and Renewable Energy. (ICMERE2015) 26 – 29 November, Chittagong, Bangladesh.
- [4] Hallaji, K., Yazıcıgil, H., (1996). Optimal management of a coastal aquifer in Southern Turkey. Journal of Water Resources Planning and Management. Volume 12.2, Issue 4, 233-244.
- [5] Bhattacharyya A., (2013). Solar stills for desalination of water in rural households. Int. J. Environ. Sustain., 2, no. 1, 21-30.
- [6] Kulkarni, S.J., Kherde, P.M., (2013). Research on Advanced Biological Effluent Treatment: A Review. International Journal of Research & Review ([www.gkpublication.in](http://www.gkpublication.in)). 2, 508-512.
- [7] Sheshdeh, R.K., Nikou, M.R. K., Badii, K., Limaee, N.Y., Golkarnarenji, G., (2014). Equilibrium and kinetics studies for the adsorption of Basic Red 46 on nickel oxide nanoparticles-modified diatomite in aqueous solutions. Journal of the Taiwan Institute of Chemical Engineers. 45, 1792–1802.
- [8] Slosarczyk, A., Paszkiewicz, Z., Paluszkiewicz, C., (2005). FTIR and XRD evaluation of carbonated hydroxyapatite powders synthesized by wet methods. Journal of Molecular Structure. 657–661.
- [9] Tharaneedhar, V., Kumar, P.S., (2017). Saravanan, A. Ravikumar, C. Jaikumar, V. Prediction and interpretation of adsorption parameters for the sequestration of methylene blue dye from aqueous solution using microwave assisted corncob activated carbon. Sustainable Materials and Technologies. 11, 1–11.
- [10] Chowdhury, A.N., Rahim, A., Ferdosi, Y. J., Azam, M. S., Hossain, M. M., (2010). Cobalt–nickel mixed oxide surface: A promising adsorbent for the removal of PR dye from water. Applied Surface Science. 256, 3718–3724.



- [11] Gabrovska M. Krstić, J., Edreva-Kardjieva, R., Stanković, M., Jovanović, D., (2006). The influence of the support on the properties of nickel catalysts for edible oil hydrogenation. *Appl. Catal. A-Gen.*, 299, 73.
- [12] Al - Amri L. S. A. A., Subhi, M., and Namdeti, R., (2014). Comparison Studies for the removal of Methylene Blue from aqueous solution using Tea and Coffee powder. *International Journal of Chemical Technology Research*. 6, 619 – 627.
- [13] Lingamdinne, L.P., Choi, Y.L., SoonKim, I.M., Kim, Yang, J.K., Koduru, J.R., YoungChang, Y., (2017). Preparation and characterization of porous reduced graphene oxide based inverse spinel nickel ferrite nanocomposite for adsorption removal of radionuclides. *Journal of Hazardous Materials*. 326, 145–156.
- [14] Gupta, V. K., Jain, R., Siddiqui, M. N., Saleh, T. A., Agarwal, S., Malati, S., Pathak, D., (2010). Equilibrium and Thermodynamic Studies on the Adsorption of the Dye Rhodamine-B onto Mustard Cake and Activated Carbon. *J. Chem. Eng. Data*. 55, 5225–5229
- [15] Saeeda, A., Sharif, M., Iqbal, M., (2010). Application potential of grapefruit peel as dye sorbent: Kinetics, equilibrium and mechanism of crystal violet adsorption. *J. Hazard. Mater.* 179, 564–572.
- [16] Chollom, M.N., Rathilal, S., Swalaha, F.M., Bakare B.F., (2020). Adsorptive removal of veterinary antibiotics from water using an integrated photocatalyst (IPCA) *Int. J. Environ. Stud.*, 77 (2), 236-254
- [17] Gupta, V. K., Jain, R., Shrivastava, M., Navak, A., (2010). Equilibrium and thermodynamic studies on the adsorption of the dye tartrazine onto waste coconut husks carbon and activated Carbon. *J. Chem. Eng. Data*. 55, 5083–5090.
- [18] Aqdam, S.R., Otzen, D.E., Morshedi, D., (2021). Adsorption of azo dyes by a novel bio-nanocomposite based on whey protein nanofibrils and nano-clay: Equilibrium isotherm and kinetic modeling *Journal of Colloid and Interface Science*. 602, 490-503.
- [19] Dotto, G. L., Pinto, L. A. A., (2011). Adsorption of food dyes onto chitosan: Optimization process and kinetic. *Carbohydr. Polym.* 84, 231–238.
- [20] Kumar, P.S., Ramalingam S., Senthamarai, C., Niranjana M., Vijayalakshmi P., Sivanesan, S., (2010). Adsorption of Dye from Aqueous Solution by Cashew Nut Shell: Studies on Equilibrium Isotherm, Desalination, Volume 261, Issue 1-2, Pages 52 – 60.
- [21] Deniz, F., Karaman, S., Saygideger, S.D., (2011). Biosorption of a model basic dye onto *Pinus brutia* Ten: evaluating of equilibrium, kinetic and thermodynamic data, *Desalination*, 270, 199-205.
- [22] Hameed, B.H., (2008). Equilibrium and kinetic studies of methyl violet sorption by agricultural waste. *J. Hazard Mater.*, 154, 204-212.
- [23] Ho, Y., McKay, G., (1999). Pseudo-second order model for sorption processes, *Process Biochem.*, 34, 451-465.
- [24] Shah, J., Jan, M., Zeeshan, R., Imran, M.M., (2017). Kinetic, equilibrium and thermodynamic studies for sorption of 2,4-dichlorophenol onto surfactant modified fuller's earth. *Appl. Clay Sci.*, 143, 227-233.
- [25] Iram, M., Guo, C., Guan, Y., Ishfaq, A., Liu, H., (2010). Adsorption and magnetic removal of neutral red dye from aqueous solution using Fe<sub>3</sub>O<sub>4</sub> hollow nanospheres. *J. Hazard. Mater.*, 181, 1039–1050.

[26] Shabani, S., Dinari, M., (2021). Cu-Ca-Al-layered double hydroxide modified by itaconic acid as an adsorbent for anionic dye removal: Kinetic and isotherm study, *Inorganic Chemistry Communications*, 133, 108914.

[27] Mishra, S., Sahoo, S.S., Debnath, A.K., Muthe, K.P., Das, N., Parhi, P., (2020). Cobalt ferrite nanoparticles prepared by microwave hydrothermal synthesis and adsorption efficiency for organic dyes: Isotherms, thermodynamics and kinetic studies, *Advanced Powder Technology*. 133, 4552-4562.

[28] Design-Expert 9 User's Guide Multifactor RSM Tutorial: Stat-Ease Incorporated, (2013), 1–56.

[29] Dashamiri, S., Ghaedi, M., Asfaram, A., Zare, F., Wang, S., (2017). Multi-response optimization of ultrasound assisted competitive adsorption of dyes onto Cu(OH)<sub>2</sub>-nanoparticle loaded activated carbon: Central composite design, *Ultrasonics Sonochemistry*, 34, 343–353.

[30] Bajpai, S., Gupta, S.K., Dey, A., Jha M.K., Bajpai, V., Joshi, S., Gupta, A., (2012). Application of Central Composite Design approach for removal of chromium (VI) from aqueous solution using weakly anionic resin: Modeling, optimization, and study of interactive variables, *Journal of Hazardous Materials*. 227– 228: 436– 444.

# Investigation of the Effects of Unidirectional Compression on the Hardness of High-Density Polyethylene Materials

\*<sup>1</sup> Erkin Akdoğan 

<sup>1</sup> Karamanoğlu Mehmetbey University, Department of Mechanical Engineering, Karaman, Turkey.  
\* Corresponding author, e-mail: eakdogan@kmu.edu.tr

Submission Date: 29.04.2022

Acceptation Date: 27.05.2022

**Abstract** - In this study, hardness measurements were carried out by applying one-way compression to the high-density polyethylene (HDPE) material at different rates. The amount of deformation was made at room conditions approximately at 23 °C and 50% humidity with 10%, 20%, 30%, 40%, 50%, 60%, 70% and 80% strain ratios. Compression processes were made on 3 mm thick plate samples. The pressing direction was carried out in the direction of thickness. The hardness and stress values of the samples were determined which were subjected to compression processes. In addition, plastic deformation rates for each compression ratio were calculated. The highest hardness value was determined at a 10% compression ratio, and it was observed that the hardness values decreased with increasing compression ratios. In plastic deformation rates, the permanent deformation of 10% and 20% is very slight, and apart from these, a remarkable increase has been observed with increasing deformation rates.

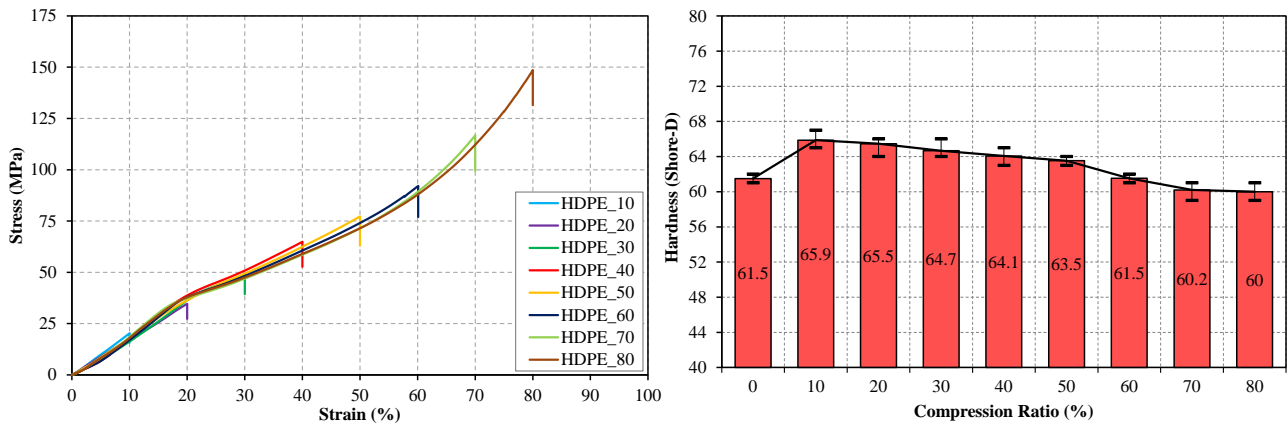
**Keywords:** High-density polyethylene, Compression, Deformation, Hardness, Stress

## Tek Yönlü Basma İşleminin Yüksek Yoğunluklu Polietilen Malzemelerin Sertliğine Etkisinin Araştırılması

**Öz** - Bu çalışmada yüksek yoğunluklu polietilen (HDPE) malzemeye farklı oranlarda tek yönlü basma işlemi uygulanarak sertlik ölçümleri gerçekleştirilmiştir. Şekil değişim miktarları %10, %20, %30, %40, %50, %60, %70 ve %80 oranlarında oda şartlarında yaklaşık 23 °C and %50 nemde gerçekleştirilmiştir. Basma işlemleri plaka şeklinde 3 mm kalınlığında numunelere yapılmıştır. Basma yönü kalınlık doğrultusunda gerçekleştirilmiştir. Basma işlemleri yapılan numunelerin sertlik değerleri ve gerilme değerleri tespit edilmiştir. Ayrıca her bir sıkıştırma oranı için plastik deformasyon oranları hesaplanmıştır. %10 basma oranında en yüksek sertlik değeri tespit edilmiş olup artan basma oranlarında sertlik değerlerinin düştüğü gözlemlenmiştir. Plastik deformasyon oranlarında ise %10 ve %20 oranlarında kalıcı şekil değişimi çok düşük değerlerde olup artan deformasyon oranlarında dikkate değer bir artış görülmüştür.

**Anahtar kelimeler:** Yüksek yoğunluklu polietilen, Basma, Deformasyon, Sertlik, Gerilme

### GRAPHICAL ABSTRACT (If possible)



## 1. Introduction

HDPE materials are widely used due to their lightweight, good insulation, easy moldability and cheapness [1]. HDPE materials are one of the semi-crystalline polymers in the polyolefin family. The name of polyethylene comes from the structures that form it, from ethylene monomers. HDPE polymers are more crystalline than the other types of polyethylene like low-density polyethylene (LDPE), linear low-density polyethylene (LLDPE) and cross-linked polyethylene (XLPE). This situation makes HDPE more ductile than the other polyethylenes. These materials can be exposed to mechanical, thermal, ultraviolet rays and chemical factors during use. Some properties may change after the specified factors. The determination of these features is also an important issue.

It has been observed that after the tensile test the tensile strength values of the samples with increasing deformation rates, increase the tensile strength and modulus of elasticity values in contrast to the elongation at break values decrease in the results of the studies in the literature [2]. In another study, it was observed that the thermal aging process of HDPE material increased its mechanical properties, as well as increased hardness values [3]. Harekrushna et al. (2019) mixed HDPE material and polypropylene (PP) material in different ratios by mass in their study. They determined that the speed of testing and surface roughness of the polymer mixtures affect the mechanical properties of materials. Lamri et al. (2020) found out that increasing the strain rate in tension will decrease the molecular mobility of the HDPE chains by making the chains stiffer.

Koriem et al. (2021) pointed out that several researchers have studied the effect of weathering on the chemical and physical properties of polymers. And those researchers found out that degradation affects the physicochemical properties of polymers. In addition, they concluded that additives are very effective for the stability and durability of the polymer matrix.

In this study, different from the studies in the literature, the compression process was applied to HDPE materials and hardness measurements were carried out. Such a process has not been performed before and it is planned to contribute to the literature in this way. Compression process was carried out at 10%, 20%, 30%, 40%, 50%, 60%, 70% and 80% deformation rates in the direction of the thickness of HDPE materials. Stress values were calculated for applied compression ratios. The plastic deformations occurring at these rates were calculated by measuring their thickness. The hardness of the samples was measured at the specified compression ratios.

## 2. Materials and Methods

Petkim I668 was used as HDPE material which is a commercial product in granule form with a melt flow rate of 5.5 g/10 min (190 °C / 2.16 kg). HDPE granule raw material is shown in Figure 1 [7]. HDPE granules were dried in an oven at 60 °C for 4 hours before the injection molding machine. Then, the samples were produced by melting at 170-180-190-200 °C from the feeding zone to the nozzle zone in a plastic injection machine with a screw diameter of 35 mm, L/D ratio of 30 and mold closing power of 70 tons.



Figure 1. HDPE granule raw material

All the samples were kept in the Nüve brand TK252 model conditioning unit at 23 °C and 50% relative humidity for 40 hours according to the ASTM D618 standard [8] before the tests. The oven, plastic injection machine, conditioning unit and oven are shown in Figure 2 [7].



Figure 2. Devices used in production a) oven, b) conditioning unit and (c) plastic injection machine

Compression processes were carried out in Shimadzu brand AGS-X 100 kN model 100 kN load cell static tensile-compression test device at 1.3 mm/min speed of testing according to ASTM D695 standard [9]. The universal testing machine and compression plates are given in Figure 3 [7].





Figure 3. Shimadzu AGS-X 100 kN universal tensile-compression tester and compression plates

The required sample dimensions for the compression process are  $3\pm 0.2$  mm x  $13\pm 0.5$  mm x  $25\pm 0.5$  mm. Compression samples were obtained by cutting from ASTM D790 samples [10]. Sample dimensions are given in Figure 4.

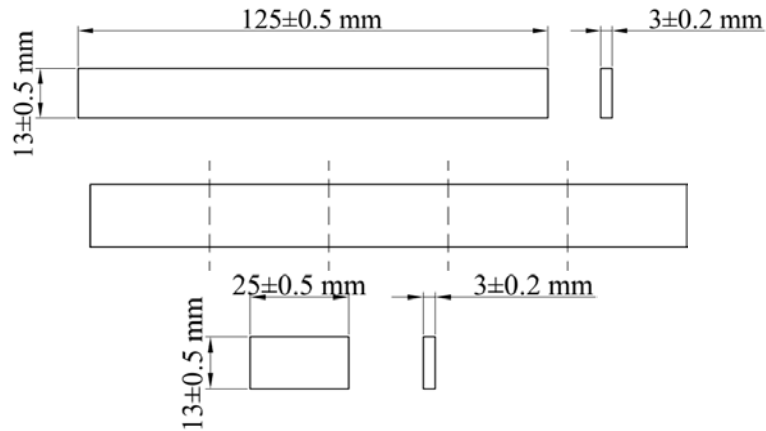


Figure 4. Dimensions of the compression sample

Compression operations were carried out in the direction of the thickness of the samples as shown in Figure 5. Compression ratio were made at the ratios of 10%, 20%, 30%, 40%, 50%, 60%, 70% and 80% according to the thickness. Six samples were subjected to the compression process at each compression ratio. Sample codes are given in Table 1.

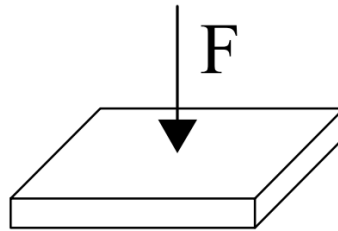


Figure 5. Direction of compression

Table 1. Compression rates and sample codes

Compression ratio (%)	Sample Code
0	HDPE
10	HDPE_10
20	HDPE_20
30	HDPE_30
40	HDPE_40
50	HDPE_50
60	HDPE_60
70	HDPE_70
80	HDPE_80

The stress values in the compression ratios of the compressed samples were determined. In addition, the hardness of the samples at these compression ratios was measured. Hardness measurements were carried out on 6 different samples each compression process using the X.F Shore-D hardness tester [3] (Figure 6) according to the ASTM D2240 standard [11].



Figure. 6 X.F Shore-D hardness tester

### 3. Results and Discussions

After compression, plastic deformation rates were measured with a digital caliper and micrometer and calculated as percent change. Compressed and uncompressed HDPE samples are shown in Figure 7. The average, highest, lowest and standard deviation values of the calculated plastic deformation rates are given in Table 2.

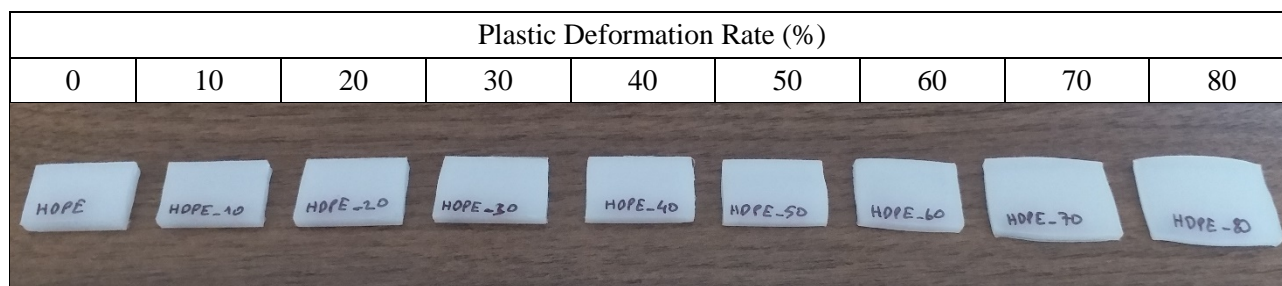


Figure 7. Compressed and uncompressed HDPE samples

Table 2. The calculated plastic deformation rates

Sample Code	Plastic Deformation Rate (%)			
	Average	Max	Min	Standard Deviation
HDPE_10	1.3	1.6	1	0.3
HDPE_20	1.3	1.7	1	0.3
HDPE_30	6.8	8.2	5.7	1.3
HDPE_40	12.7	15.2	11	2.2
HDPE_50	16.2	17.9	13.7	2.2
HDPE_60	28	31	25.7	2.7
HDPE_70	41.8	43.1	40	1.6
HDPE_80	50.5	51.6	49.2	1.2

It has been observed that the plastic deformation is at the same values at 10% and 20% compression rates. It has been determined that the material has not yet reached the yield limit at these rates, in other words, it has not reached permanent deformation. Also, it has been observed that the permanent deformation rates increase with increasing compression ratios above 20%. However, it has been found that these values are not as high as compression ratios. The reason for this is the recovery of the elastic deformation after compression. The calculated plastic deformation rates are shown in Figure 8 comparatively.

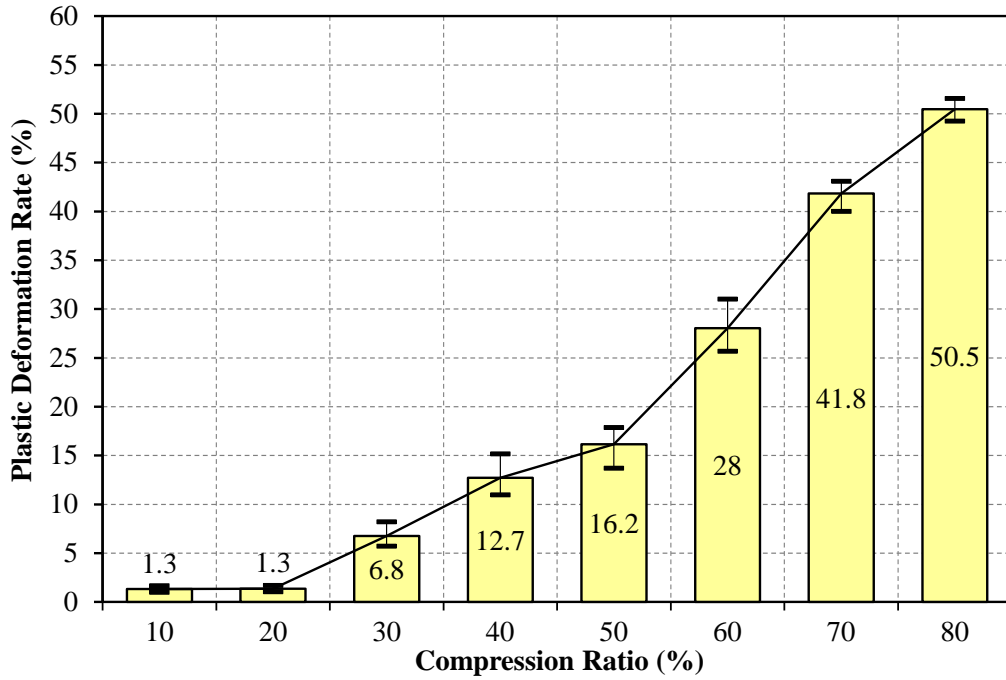


Figure 8. The calculated plastic deformation rates of HDPE materials

The compression curves are shown in Figure 9. It has been observed that the characteristics of the compression curves are in a harmony with each other. The HDPE material could not reach the yield limit up to 20% compression ratio but at increasing strain rates, yield limit values exceeded. The stress values at the determined compression ratios are given in Table 3. The average, highest, lowest and standard deviation values were calculated.

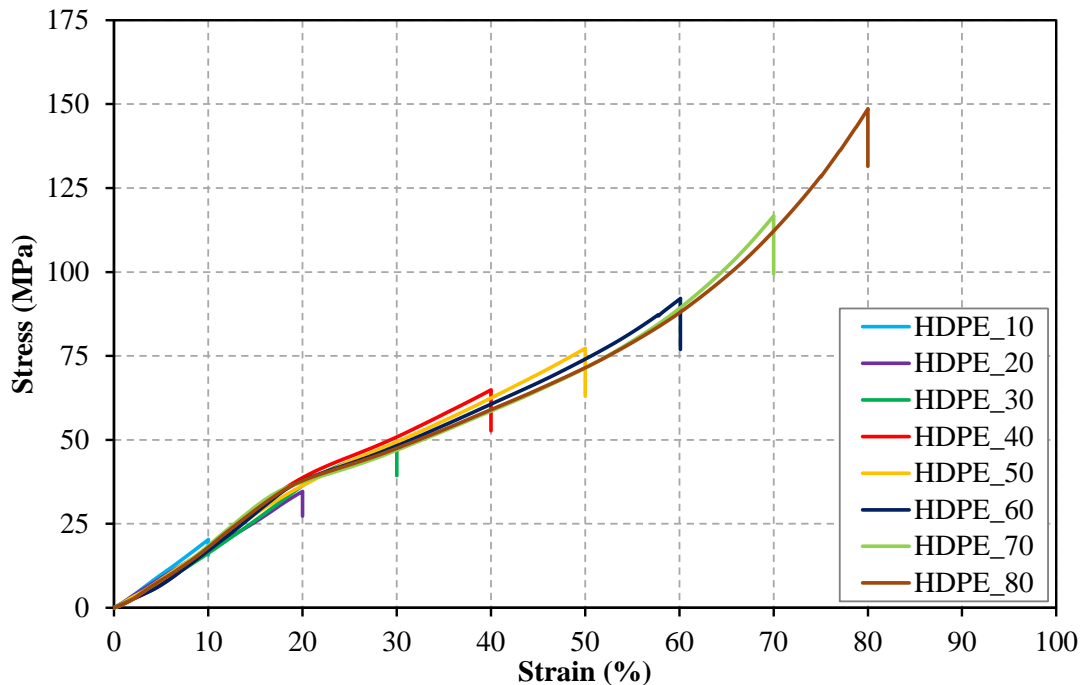


Figure 9. The compression curves of HDPE Materials

Table 3. The stress values of compressed HDPE materials

Sample Code	Stress (MPa)			
	Average	Max	Min	Standard Deviation
HDPE_10	19.8	21.5	18	1.3
HDPE_20	36.7	38.2	35.9	0.9
HDPE_30	52.1	53	51.4	0.6
HDPE_40	65.4	67.2	63	1.5
HDPE_50	77.2	78.5	75.5	1.1
HDPE_60	92.5	93.6	91.2	1.1
HDPE_70	115.8	117.9	114	1.5
HDPE_80	152.2	155.9	149.1	2.5

The stress values at the specified compression ratios are shown in Figure 10 comparatively. It is clearly seen that while a nearly linear increase is observed in the stress values up to 60% compression ratio, the amount of increase is significantly at 70% and above compression ratios.

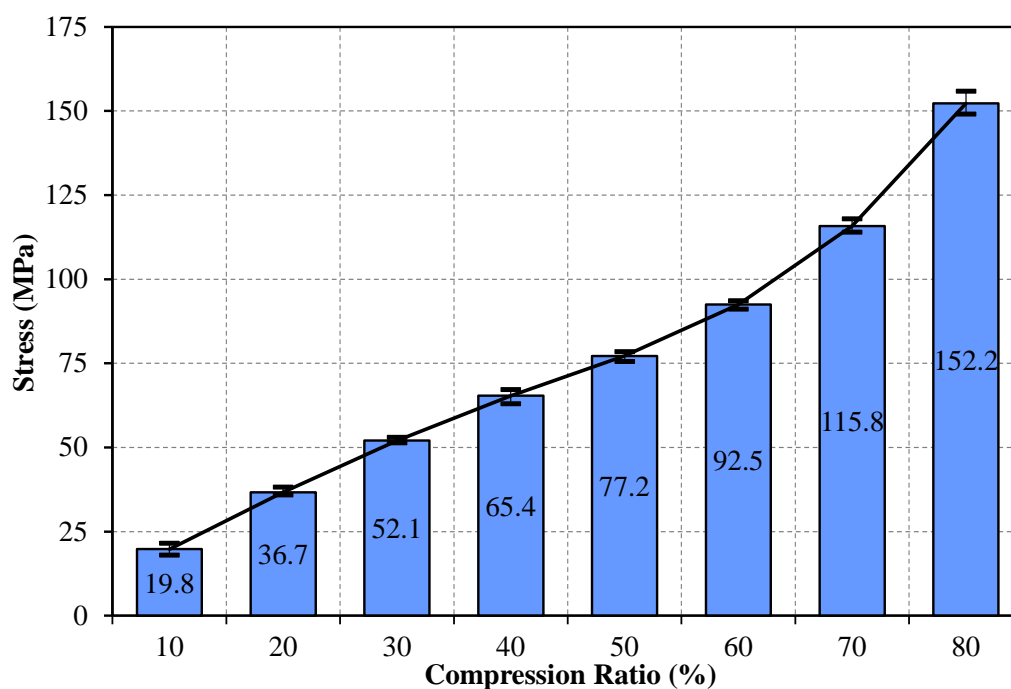


Figure 10. The stress values at specified compression ratios of HDPE Materials

After the hardness tests, mean, highest, lowest and standard deviation values were calculated. These values were given in Table 4. The hardness values were given in Fig. 11 comparatively. The highest hardness value was reached at 10% compression, and it was observed that the hardness values decreased with increasing compression ratios. This is due to the breaking of bonds between HDPE molecules at increasing deformation rates. However, it has been observed that the hardness values are higher than the uncompressed HDPE material at compression ratios between 10% and 50%.

It has been observed that it gives the same hardness values when compared to HDPE material with 60% compression ratio. On the other hand, it was determined that the hardness values at 70% and 80% compression ratios were lower than the hardness values of the materials that were not subjected to the compression process. This situation has shown that increasing deformation rates reduce the hardness values of the HDPE materials.

Table 4. The hardness values of compressed HDPE materials

Sample Code	Hardness (Shore-D)			
	Average	Max	Min	Standard Deviation
HDPE	61.5	62	61	0.5
HDPE_10	65.9	67	65	0.8
HDPE_20	65.5	66	64	0.6
HDPE_30	64.7	66	64	0.8
HDPE_40	64.1	65	63	0.8
HDPE_50	63.5	64	63	0.5
HDPE_60	61.6	62	61	0.5
HDPE_70	60.2	61	59	0.7
HDPE_80	60	61	59	0.7

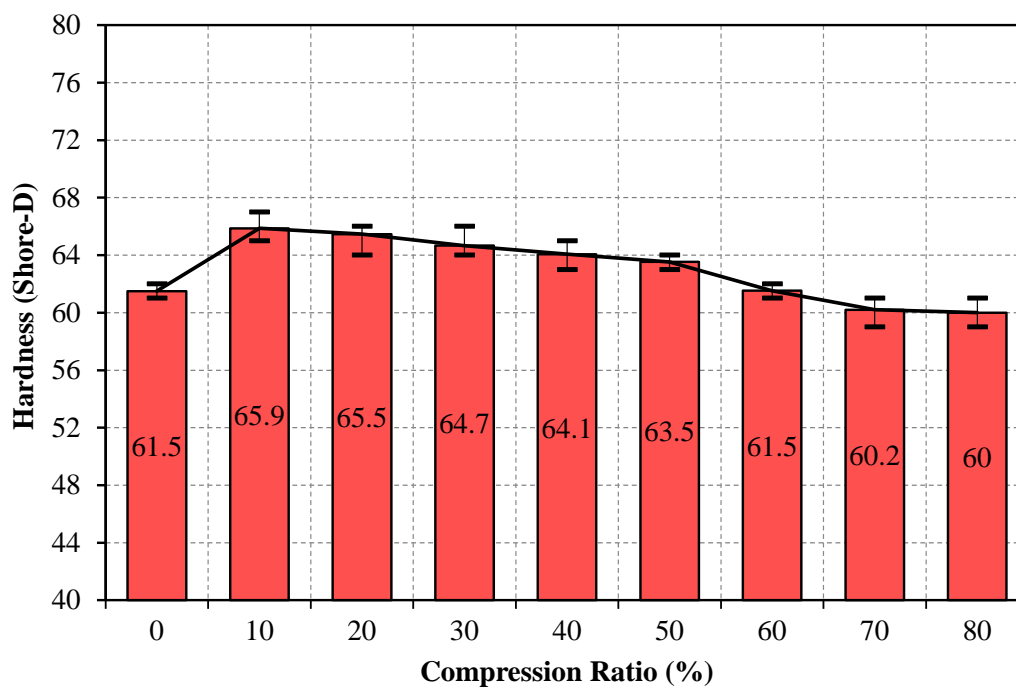


Figure 11. The hardness values at specified compression ratios of HDPE materials

#### 4. Conclusions

In this study 10%, 20%, 30%, 40%, 50%, 60%, 70% and 80% compression process were carried out on HDPE materials according to their thickness. Permanent plastic deformation rates and stress values at specified compression rates are given comparatively. Also, hardness measurements of the compressed samples were made and the results were given comparatively.

The following conclusions have been drawn as a result of this study.

- There was no plastic deformation difference observed between 10% and 20% whereas a remarkable change was observed between 30% and 80%.
- It was observed that while the hardness values increased at compression ratios between 10% and 50% but the hardness values decreased at 70% and 80% compression ratios.
- The highest increase in hardness test was observed at 10% compression ratio.



## Acknowledgment

The author would like to thank both institutions for using Pamukkale University Mechanical Engineering Laboratories and Karamanoğlu Mehmetbey University Mechanical Engineering Laboratories in the study.

In addition, the author would like to thank Research Assistant Dr. Mehmet ŞAHBAZ for his assistance in performing the mechanical experiments who works at Karamanoğlu Mehmetbey University, Department of Mechanical Engineering.

**Peer-review:** Externally peer - reviewed.

**Author contributions:** Concept - E.A.; Data Collection &/or Processing - EA.; Literature Search - E.A.; Experimental Part - E.A.

**Conflict of Interest:** No conflict of interest was declared by the author.

**Financial Disclosure:** The author declared that this study has received no financial support.

## References

- [1] Akdoğan, E. and Bektaş, N.B. 2018. The Effects of Nanoclay on Mechanical Properties of High Density Polyethylene and Polypropylene Materials, *Acta Physica Polonica A*, Vol.134, no.1. p.297-299.
- [2] Bartczak, Z., Morawiec, J. and Galeski, A. 2002. Deformation of High-Density Polyethylene Produced by Rolling with Side Constraints. II. Mechanical Properties of Oriented Bars, *Journal of Applied Polymer Science*, Vol.86, no.6. p.1405-1412.
- [3] Akdoğan, E. 2020. The Effects of High Density Polyethylene Addition to Low Density Polyethylene Polymer on Mechanical, Impact and Physical Properties, *European Journal of Technique*, Vol.10, no.1. p.25-37.
- [4] Harekrushna, S., Himanshu, M., Chiranjit, D., Rabiranjana, M. and Sangram, P. 2019. Strain Rate Effects on Tensile Properties of HDPE-PP Composite Prepared by Extrusion and Injection Moulding Method, *Materials Sciences and Applications*, Vol.10, p.205-215.
- [5] Lamri, A., Shirinbayan, M., Pereira, M., Truffault, L., Fitoussi, J., Lamouri, S., Bakir, F. and Tcharkhtchi, A. 2020. Effects of Strain Rate and Temperature on the Mechanical Behavior of High-Density Polyethylene, *Journal of Applied Polymer Science*, Vol.137, no.23. pp.48778.
- [6] Koriem, A., Ollick, A.M. and Elhadary, M. 2021. The Effect of Artificial Weathering and Hardening on Mechanical Properties of HDPE with and without UV Stabilizers, *Alexandria Engineering Journal*, Vol.60, p.4167-4175.
- [7] Şahbaz, M. and Akdoğan, E. 2022. Yüksek Yoğunluklu Polietilen Malzemelerde Termal Yaşlandırmanın Mekanik Özelliklerine Etkisinin İncelenmesi, *European Journal of Science and Technology*, Vol.34, p.757-762.
- [8] Standard Practice for Conditioning Plastics for Testing, ASTM Std. D618, 2013.
- [9] Standard Test Method for Compressive Properties of Rigid Plastics, ASTM Std. D695, 2015.
- [10] Standard Test Methods for Flexural Properties of Unreinforced and Reinforced Plastics and

Electrical Insulating Materials, ASTM Std. D790, 2017.

[11] Standard Test Method for Rubber Property-Durometer Hardness, ASTM Std. D2240, 2015.